UNIVERSITÀ DI PARMA

UNIVERSITÀ DEGLI STUDI DI PARMA

DOTTORATO DI RICERCA IN
"INGEGNERIA CIVILE E ARCHITETTURA"

CICLO XXXIV

Programmable response and controlled morphing of polymer-based elements

Coordinatore:
Chiar.mo Prof. SANDRO LONGO

Tutore:
Chiar.mo Prof. ROBERTO BRIGHENTI

Dottorando: MATTIA PANCRAZIO COSMA

Anni Accademici 2018/2019 - 2020/2021

UNIVERSITÀ DI PARMA

UNIVERSITÀ DEGLI STUDI DI PARMA

RESEARCH DOCTORATE IN
"CIVIL ENGINEERING AND ARCHITECTURE"

XXXIV CYCLE

Programmable response and controlled morphing of polymer-based elements

Coordinator:
Chiar.mo Prof. SANDRO LONGO

Tutor:
Chiar.mo Prof. ROBERTO BRIGHENTI

PhD Candidate: MATTIA PANCRAZIO COSMA

Academic Years 2018/2019 - 2020/2021

SOMMARIO

Le strutture naturali possono rispondere a stimoli esterni in modo da innescare particolari funzionalità, al fine di compiere diverse attività (svolgimento di processi biologici, attivazione di meccanismi di auto-protezione, movimento ecc.). Questo comportamento funzionale è stato codificato in modo naturale all'interno di tali strutture tramite processi biologici che hanno portato alla loro genesi, pertanto esse sono naturalmente programmate per comportarsi in uno specifico modo. L'aumento della domanda di materiali e/o dispositivi intelligenti da utilizzare in svariate applicazioni avanzate o d'uso quotidiano, ha favorito l'interesse di ricercatori ed ingegneri nello sviluppare materiali funzionali sintetici che, in maniera simile alle strutture naturali, possono opportunamente rispondere a stimoli esterni così da garantire il raggiungimento dei requisiti richiesti da una specifica applicazione in un'ottica funzionale. In questo studio, una tale definita relazione processo-microstruttura-risposta, è sfruttata per controllare e programmare la risposta meccanica di materiali funzionali sintetici innovativi a matrice polimerica; infatti, grazie a processi di sintesi e produzione innovativi (come la stampa 3D), la microstruttura di un materiale funzionale sintetico può essere programmata e fabbricata in modo tale da "codificare" la risposta meccanica del materiale in maniera specifica e personalizzabile. La microstruttura del materiale (dipendente dal processo di sintesi) offre un ampio spazio di design per lo sviluppo di nuovi polimeri funzionali. A questo scopo, in questo lavoro sono proposti modelli di tipo *physics-based*, in grado di mettere in relazione la microstruttura di un materiale funzionale con la sua risposta meccanica (e con il suo processo di sintesi), per supportarne il design attraverso un approccio ingegneristico. In particolare, questo lavoro si concentra sulla modellazione teorica e computazionale della risposta meccanica (*process-dependent*) di elastomeri in presenza di cristalli liquidi (LCE) sottoposti a stimoli di natura termica e di materiali ottenuti tramite fotopolimerizzazione. Viene mostrato come sia possibile controllare e programmare i cambiamenti di forma di LCEs sottoposti a variazioni termiche o la risposta meccanica di materiali ottenuti tramite fotopolimerizzazione, pilotando in maniera opportuna particolari caratteristiche della microstruttura del materiale, oggi possibile grazie a processi innovativi di sintesi e fabbricazione.

ABSTRACT

Natural structures can respond to external stimuli to trigger particular functionality, in order to perform some tasks (for basic biological functions to occur, to protect themselves, to perform locomotion, etc.). This functional behavior has been naturally encoded within these structures from basic biological processes, and so they are naturally-programmed to behave in a certain way. The increasing demand for smart and responsive devices to be used in many advanced and daily-life applications, has promoted the interest of researchers and engineers in developing synthetic functional materials (smart materials) which, similarly to natural structures, can respond to external stimuli in a functional way in order to meet the specific requirements of the application in turn. In this thesis, the so-called process-microstructure-responsiveness relationship concept is exploited to control and program the mechanical response of innovative synthetic polymer-based functional materials; in fact, thanks to innovative synthesis process (3D printing), the microstructure of a synthetic functional material can be programmed and fabricated in order to encode a specific tailored mechanical responsiveness to the material. The process-dependent material's microstructure offers a wide design space for the development of new functional polymers. To this aim, physics-based models capable to relate the microstructure of a functional material to its responsiveness (as well as to its synthesis process), to support its design through an engineering approach, are proposed. In particular, the theoretical and computational modeling of the process-dependent mechanical response of thermally-responsive Liquid Crystal Elastomer (LCE) materials and of materials obtained through photopolymerization, is considered. It is shown how microscale features of the material, today controllable by means of innovative synthesis and manufacturing processes, can be tuned in order to control and program the shape-morphing of LCE materials under thermal stimuli or the mechanical response of photopolymerized materials.

DEDICATION

To my family.

TABLE OF CONTENTS

LIST OF FIGURES

FIGURE **Page**

NOMENCLATURE

A	absorbance of the material
$\boldsymbol{A}$	absorbance matrix of the FE discretized domain
b	length of a Kuhn's segment
$\boldsymbol{b}$	external body forces vector field
$\mathscr{B}$, $\mathscr{B}_0$	region occupied by the continuum body in the current and in the reference configuration, respectively
$\mathbf{C}$, C_{ij}	right Cauchy-Green deformation tensor
c_a	number of active polymer chains per unit volume (cross-link density, chain concentration)
$\overline{c}_a$	cross-link density corresponding to the optimal actuation of a LCE material
c_t	maximum cross-link density of a LCE material for which no actuation takes place
C_I	concentration of photo-initiators (PH_I), $\left[N/L^3\right]$
C_R	concentration of free-radicals (R), $\left[N/L^3\right]$
C_M	concentration of monomer molecules (M), $\left[N/L^3\right]$
$\boldsymbol{E}$, E_{ij}	Green-Lagrange strain tensor
$\boldsymbol{F}$, F_{ij}	deformation gradient tensor
$\boldsymbol{f}$, f_i	force vector of a polymer chain
$\mathbf{G}$	global vector of the nodal values of the light intensity, of the FE discretized domain
h_{1a}, $h_{1\beta}$	normalized objective functions for the optimum photopolymerization process
$\boldsymbol{H}$	light gradient matrix of the FE discretized domain
I	light intensity per unit area $\left[M/T^3\right]$
$\overline{\boldsymbol{I}}$	light intensity vector-field on the irradiated surface of the FE discretized domain
$\tilde{\mathbf{I}}$	global vector of the sought nodal values of the light intensity of the FE discretized domain
I_m	maximum light intensity on the irradiated surface of the body per unit area $\left[M/T^3\right]$
$J = \det\boldsymbol{F}$	volume change during deformation
k_B	Boltzmann constant, $k_B = 1.38 \cdot 10^{-23} J/K$
k_d	chain dissociation rate $[1/T]$
k_{pr}	photo-initiators decomposition rate $\left[T^2/M\right]$
k_p	propagation rate constant $\left[L^3/NT\right]$
k_t	termination rate constant $\left[L^3/NT\right]$

$\boldsymbol{L}$, L_{ij}	velocity gradient tensor
$\mathscr{L}$, $\mathscr{L}^{-1}$	Langevin function and its inverse, respectively
$\boldsymbol{\ell}$, $\boldsymbol{\ell}_0$	step length tensor in the current and in the initial nematic state, respectively
$\boldsymbol{l}$	unit vector indicating the direction of the incoming light intensity
$\boldsymbol{M}$	stabilization matrix required by the numerical solution of the light diffusion phenomenon
N	number of Kuhn's segment in a polymer chain
$\boldsymbol{P}$, P_{ij}	first Piola-Kirchhoff stress tensor
$\boldsymbol{Q}$, $\boldsymbol{Q}_0$	order tensor in the current and in the initial nematic configuration, respectively
Q, Q_0	current and initial order parameter, respectively
$\boldsymbol{r}$, r_i	end-to-end vector
$\boldsymbol{S}$, S_{ij}	second Piola-Kirchhoff stress tensor
t	time [T]
t_c	curing time
T	absolute temperature [Θ]
T_{NI}	nematic-isotropic transition temperature
$\boldsymbol{u}$, u_i	current displacement vector field
v	translational laser speed [L/T]
$\boldsymbol{x}$,$\boldsymbol{X}$	vector indicating the position of a material point, in the current and reference configuration of the continuum, respectively
λ	uniaxial stretch
μ	shear modulus
$\boldsymbol{\mu}$, $\boldsymbol{\mu}_0$	chain distribution tensor in the current and in the reference stress-free configuration, respectively
$\dot{\boldsymbol{\mu}}_F$, $\dot{\boldsymbol{\mu}}_v$, $\dot{\boldsymbol{\mu}}_n$	time rates of the chain distribution tensor due to the elastic deformation, the viscoelastic phenomena and the nematic-isotropic transition, respectively
ρ, ρ_0	Chain Configuration Density Function (CCDF) in the current and in the reference stress-free configuration, respectively
$\boldsymbol{\sigma}$, σ_{ij}	Cauchy stress tensor
τ	time variable referred to both the photopolymerization process and the mechanical problem
φ, φ_0	dimensionless statistical distribution function of polymer chains (classical polymer) in the current and in the isotropic stress-free configuration, respectively
φ_n, φ_{0n}	dimensionless statistical distribution function of polymer chains (liquid crystal elastomers) in the current and in the non-isotropic stress-free configuration, respectively
ψ_c	free energy of an individual polymer chain
Ψ	strain energy density of a polymer network
Ω, Ω_0	chain configuration space (microscale) in the current and in the reference stress-free configuration, respectively
π	hydrostatic pressure

CHAPTER 1

INTRODUCTION

Nowadays, the unique features of the fascinating and complex architectures of natural structures and materials, are noticeably promoting the interest of scientists and engineers. Natural structures can have intricate architectures across different scale-size (nano-, micro- and meso- scale); these particular structures are responsible for providing an impressive range of functional or multifunctional materials properties and behaviors. Natural structures can respond to environmental conditions or to peculiar external stimuli, for basic biological functions to occur, for protecting themselves by the surrounding, for performing locomotion, etc. If required, they can also exhibit multiple capabilities at the same time.

The increasing demand for smart and responsive devices to be used in many advanced and daily-life applications, has promoted the interest of researchers in developing new materials (often known as Smart Materials or Functional Materials) which can have, to some extent, several similarities to natural structures. Functional materials can adapt their physical-chemical properties, geometrical shape, mechanical response, etc., by properly responding to external stimuli.

Encoding functionalities in materials and composites has been recognized as a promising route to solve new issues in emerging applications, such as in robotics, biomedicine, nanotechnologies (sensors and actuators, nanorobots), energy harvesters, flexible electronics, etc.

Polymers have been often considered for developing innovative functional materials, thanks to their low cost and lightweight, ease of manufacturing, good corrosion resistance, ease of coupling with other materials or inserting particular molecules within their network, excellence in mechanically mimicking biological tissues and living organisms, etc.

A deep knowledge of the physical mechanisms underneath the responsive behaviour of functional materials and their engineering assessment, are key aspects in order to develop and expand their use in real applications as well as to open new insights in the research field. To achieve this goal, the

development of theoretical and computational physics-based models, suitable for a mathematical description of the functional response of this class of materials, is increasingly required.

1.1 Motivation of the work

The aim of the present work is to develop theoretical (physics-based) and numerical models for the assessment and design of innovative functional materials. The mathematical description of the mechanical response of functional materials is the key aspect to fully control, program and guide the development and production of innovative devices, as well as to engineer the microstructure of materials, enabling the functionalities required by novel applications following an engineering approach.

To this aim, the leitmotif of the present work is routed on the so called *process-microstructure-responsiveness* relationship. Modern fabrication technologies (*process*) are nowadays used for synthesizing functional materials. These technologies are capable of providing an opportune *microstructure* to the synthesized material, enabling to get a tailored and precise material's *responsiveness* under external stimuli. In this context, physics-based models which provide a mathematical description of the *process-microstructure-responsiveness* relationship, can be exploited for controlling and programming the responsiveness of functional materials, as well as for the design of new ones.

The present thesis focuses particularly on modeling and simulation of the functional mechanical response of:

(1) thermally-responsive Liquid Crystal Elastomer (LCE) materials;

(2) polymeric materials obtained through photopolymerization;

In both cases, the development of a physics-based model framed on the general idea of representing the polymer's mechanical behaviour through the description of its chain network configuration, has been considered. The chain configuration as well as its evolution induced by chemical-physical stimuli, is strictly related to the macroscopic response of the material. In this context, the initial process-dependent material's microstructure offers a wide design space for the development of new functional polymers.

1.2 Outline of the thesis

The thesis is organized as follows.

Chapter 2 briefly recalls the general concepts of the mechanics of polymers and polymer-like materials and illustrates the main concepts of the micromechanical-based model used across the thesis.

Chapter 3 presents an original overview on the programmable response and morphing of (a) natural structures and (b) synthetic functional polymer-like materials, by outlining an interesting parallelism between these two realms.

Chapter 4 presents a micromechanical-based model suitable to simulate the process dependent mechanical response of thermally-responsive LCEs. Core of this chapter is also the computational analysis devoted to control and program the shape-morphing of LCE-based elements.

Chapter 5 presents a multi-physics based model to describe the mechanical behaviour of photopolymerized materials by considering their synthesis process. Numerical analyses aimed at investigating the possibility of programming the mechanical response of elements through a tailored photopolymerization, are performed.

Chapter 6 closes the work with some final remarks and future perspectives.

CHAPTER 2

MECHANICS OF POLYMER-LIKE MATERIALS

Polymers and polymer-like materials include a vast class of materials which are today used in the most disparate application fields. They are typically synthesized from petroleum hydrocarbons (such as polyethylene, polypropilene, nylon, etc.), or they can be obtained from natural polymer-like materials like cellulose, collagen, silk, etc., such as in the context of bio-inspired polymers.

Generally speaking, these materials are characterized by desirable properties in real applications, such as light weight, good strength, high flexibility, chemical stability, etc., to name a few [1].

Polymers are materials chemically constituted of long molecules made of several repetition of identical units called monomers [2, 3]. However, polymers are more complex than this [4]; in fact, the chemical-physical variety of this material can be extremely high, for instance due to variations of molecular structure in the same network in terms of weight (length), branching, interconnections, presence of chemical defects, degree of alignement, etc. [4].

The mechanical response of these materials can be very different; depending on the chemical structure as well as the working temperature, a polymer can be soft (rubber, in common language) or it can be hard (commonly known such as plastic). However, this distinction commonly adopted in daily-life, can be non-trivial; for example, depending on the working temperature (above or below the characteristic glass transition temperature) polymers can have either a soft-like or a rigid-like mechanical behavior, [5].

The wide range of chemical and physical structures existing in polymers, or in polymer-like materials, makes very difficult a unique categorization of such materials [4]. With particular reference to polymers, a common classification subdivides these materials into thermoplastics, thermosets and elastomers, each one characterized by different properties [4].

From a mechanical viewpoint, the behavior of these materials can be treated by harnessing the concepts of the so-called rubber elasticity theory [2, 6].

According to [7], an implicit definition of a rubber-like material [6] comes from a set of three features related to its molecular structure: (a) the presence of long-chain molecules with freely rotating links, (b) the mutual exchanges of weak secondary forces, (c) connections (cross-link sites or junction points) along their length to form a coherent three-dimensional network, making it a solid rather than a liquid.

This schematic description originally drawn by Treloar [6], represents an important guideline to develop models suitable to describe the mechanical behavior of polymer-like materials (amorphous rubber-like materials, soft tissues, several biological and bioinspired materials, etc.) as well as to engineer and develop innovative functional polymer-based materials. Basically, all the materials characterized by the so-called entropic-elasticity (features a-b) and by a coherent solid state given by the interconnection existing among the molecules (c), belong to this category [7].

This chapter is organized as follows: sect. 2.1 illustrates some basic concepts of the non-linear solid mechanics. Sect. 2.2 gives an overview on the mechanical behavior description of polymer-like materials. Sect. 2.3 illustrates the main concepts of the micro-mechanical model of polymer-like materials used across the thesis.

2.1 Introduction to non-linear solid mechanics

This section, following the pioneer work of Holzapfel [8], briefly summarizes the main concept of the non-linear solid mechanics.

Let's consider a continuum body embedded in a three-dimensional Euclidean space, whose stress free state at $t = 0$ is known; in such a configuration, the continuum body occupies the domain $\mathscr{B}_0$.

The continuum body is assumed to be sufficiently restrained to avoid rigid body motion and it is subjected to external loads inducing deformation. In a generic deformed state at the time t, the continuum body occupies the region $\mathscr{B}$ of the Euclidean space.

Let's consider a generic material point $P_0 \in \mathscr{B}_0$ whose position is provided by the vector $\mathbf{X} = (X_1, X_2, X_3)$; on the other hand, in a generic deformed state $P \in \mathscr{B}$ and the position of such a material point is $\mathbf{x} = (x_1, x_2, x_3)$. Following a Lagrangian description, the corresponding current displacement vector field $\mathbf{u}$, evaluated with respect to the initial reference configuration, is [8]:

$$\mathbf{u}(\mathbf{X}, t) = \mathbf{x}(\mathbf{X}, t) - \mathbf{X}(t = 0) \tag{2.1}$$

By considering a generic line connecting two material points, denoted with $d\mathbf{X}$ and $d\mathbf{x}$ in the reference and in the deformed configuration, respectively, the deformation gradient tensor is defined as [8]:

$$\mathbf{F} = F_{ij} = \frac{\partial x_i}{\partial X_j} = \mathrm{Grad}\,\mathbf{u} + \mathbb{1} \tag{2.2}$$

where $\mathbb{1}$ is the second order unit tensor. The determinant of $\mathbf{F}$ quantifies the volume change taking place during deformation, $J = \det\mathbf{F}$. If the material is assumed to be incompressible, it holds $J = \det\mathbf{F} = 1$.

In order to quantify the rate of deformation of the continuum body, the material velocity gradient can be introduced [8]:

$$\dot{\mathbf{F}} = \dot{F}_{ij} = \frac{\partial \dot{x}_i}{\partial X_j} = \frac{\partial \dot{x}_i}{\partial x_k}\frac{\partial x_k}{\partial X_j} = L_{ik}F_{kj} = \mathbf{LF} \tag{2.3}$$

which represents the material time derivative of the deformation gradient, being $\mathbf{L}$ the velocity gradient tensor. From Eq. 2.3 follows $\mathbf{L} = \dot{\mathbf{F}}\mathbf{F}^{-1}$.

A commonly adopted deformation measure, suitable to be used in non-linear solid mechanics, is the so-called Green-Lagrange second order strain tensor, defined as [8]:

$$\mathbf{E} = \frac{1}{2}\left(\mathbf{F}^T\mathbf{F} - \mathbb{1}\right) = \frac{1}{2}(\mathbf{C} - \mathbb{1}) \tag{2.4}$$

being $\mathbf{C} = \mathbf{F}^T\mathbf{F}$ the right Cauchy-Green tensor. It is worth mentioning that other deformation measures exist [8].

The eigenvalues of $\mathbf{C}$ represent the square roots of the principal stretches (λ_i, $i = 1,2,3$ the three principal stretches). Being based on the principal stretches, some strain invariants can be introduced [8]:

$$I_1(\mathbf{C}) = \mathrm{tr}\mathbf{C} = C_{ii} = \lambda_1^2 + \lambda_2^2 + \lambda_3^2 \tag{2.5}$$

$$I_2(\mathbf{C}) = \frac{1}{2}\left[(\mathrm{tr}\mathbf{C})^2 + \left(\mathrm{tr}\mathbf{C}^2\right)\right] = \frac{1}{2}\left(C_{ii}^2 - C_{ij}C_{ij}\right) = \lambda_1^2\lambda_2^2 + \lambda_1^2\lambda_3^2 + \lambda_2^2\lambda_3^2 \tag{2.6}$$

$$I_3(\mathbf{C}) = \det\mathbf{C} = \lambda_1^2 + \lambda_2^2 + \lambda_3^2 \tag{2.7}$$

Concerning the stress measures in non-linear solid mechanics, it is worth recalling the First-Piola Kirchhoff (or *nominal*) stress tensor $\mathbf{P}$ (which is not symmetric) and the Cauchy (or *true*) stress tensor $\boldsymbol{\sigma}$ (which is symmetric). They are related through the following relationships [8]:

$$\mathbf{P} = J\boldsymbol{\sigma}\mathbf{F}^{-T} \tag{2.8}$$

$$\boldsymbol{\sigma} = J^{-1}\mathbf{P}\mathbf{F}^T \tag{2.9}$$

Another stress tensor used in non-linear solid mechanics is the second Piola-Kirchhoff stress tensor $\mathbf{S}$, which is a symmetric tensor related to $\mathbf{P}$ and $\boldsymbol{\sigma}$ as follows [8]:

$$\mathbf{S} = \mathbf{F}^{-1}\mathbf{P} = J\mathbf{F}^{-1}\boldsymbol{\sigma}\mathbf{F}^{-T} \tag{2.10}$$

Finally, it is worth recalling the linear momentum balance in continuum mechanics, written in the current configuration [8]:

$$\mathrm{div}\boldsymbol{\sigma} + \mathbf{b} = \mathbf{0} \qquad \text{or} \qquad \frac{\partial \sigma_{ij}}{\partial x_j} + b_i = 0 \tag{2.11}$$

with $\mathbf{b}$ the external body forces vector field.

The above-illustrated aspects concerning the deformation (kinematics), the stress state and the static balance principle in continuum mechanics, do not suffice to analyse the mechanical response of a deformable continuum body, since they do not take into account the specific constitutive relationship of the material.

The characterization of the mechanical response of a continuum body requires therefore to introduce the proper constitutive law of the constituting material [8]. Within this perspective, dealing with the so-called hyperelastic materials, the existence of a strain energy function (Ψ) is postulated [8]; typically Ψ is a function of $\mathbf{F}$ or of other deformation measures (see sect. 2.2). For an hyperelastic material, the stress state is related to its deformation through the following constitutive equations [8]:

$$\mathbf{P} = \frac{\partial \Psi(\mathbf{F})}{\partial \mathbf{F}} \qquad \text{or} \qquad P_{ij} = \frac{\partial \Psi}{\partial F_{ij}} \tag{2.12}$$

$$\boldsymbol{\sigma} = J^{-1} \frac{\partial \Psi(\mathbf{F})}{\partial \mathbf{F}} \mathbf{F}^T \qquad \text{or} \qquad \sigma_{ij} = J^{-1} \frac{\partial \Psi}{\partial F_{ij}} F_{ji} \tag{2.13}$$

It is worth mentioning that Ψ can be also expressed through the principal stretches; in such cases, the constitutive relations can be similarly obtained by differentiating such a function with respect to the corresponding principal stretches [8].

2.2 Mechanical description of polymer-like materials

The mechanical behavior of polymers and polymer-like materials can be described by following two main routes, namely phenomenological or physics-based approaches.

Phenomenological-based models (sect. 2.2.1) typically postulate the existence of a strain-energy function $\Psi = f(I_1, I_2, I_3)$ not related to the state of the materials microstructure [9].

On the other hand, physics-based models (sect. 2.2.2), typically starting from the statistical mechanics of individual polymer chains [10], aim at describing the mechanics of a polymeric material through considerations related to its microstructure. Within the latter approach, the strain-energy function is defined through thermodynamic principles by accounting for the entropy of the polymer related to the physical state of the polymer network (chain conformation).

The stress state of the material can be determined by differentiating the strain-energy function, expressed according to the adopted approach, with respect to the deformation gradient (sect. 2.1).

2.2.1 Phenomenological approach of the mechanics of polymers

The mechanical description of polymers through phenomenological approaches, is typically based on the definition of a strain energy function - postulated *a priori* - without any physical relationship to the nature of the materials.

The strain energy density function Ψ, provides a relationship between the continuum deformation and some empirical-material-related parameters, usually determined by experimental fitting.

It can be function of the material strain invariants (invariant-based mechanics) or, alternatively, it can be directly expressed through the principal stretches (stretch-based mechanics) [11].

In such a context, the problem is mainly to find the proper form of this function; to this aim, several models have been proposed [7].

The simplest strain energy function, suitable for the mechanical description of a polymer-like material, has been proposed by Rivlin (Neo-Hookean model) and is expressed by the following form of the energy density:

$$\Psi = \frac{\mu}{2}(I_1 - 3) \tag{2.14}$$

where μ is the shear modulus of the material and I_1 is the first invariant of the right Cauchy-Green tensor. This model can be also recovered through a physics-based statistical mechanics approach, thus providing the reconciliation of the physics-based statistical theory and the phenomenological approach (see sect. 2.2.2).

On the other hand, the Mooney-Rivlin model postulates the existence of the following strain energy function:

$$\Psi = C_1(I_1 - 3) + C_2(I_2 - 3) \tag{2.15}$$

where C_1 and C_2 are material-dependent parameters [7].

In the context of stretch-based continuum mechanics, one of the most important model was proposed by Ogden [11]:

$$\Psi = \frac{\mu_j}{\alpha_j}(\lambda_1^{\alpha_j} + \lambda_2^{\alpha_j} + \lambda_3^{\alpha_j} - 3) \tag{2.16}$$

where the sum over the index $j = 1,2,3$ is assumed. In Eq. 2.16, μ_j and α_j are material-dependent-parameters.

The Neo-Hookean model is suitable to describe the mechanics of polymers from small to moderate deformations, while the Mooney-Rivlin model can overcome this limit. For both models the accuracy achievable is related to the deformation experienced by the material (simple shear, uniaxial elongation, biaxial elongation etc.) see [11]. On the other hand, the strain energy proposed by Ogden represents one of the principal outcome of the nonlinear elasticity; it allows fitting a large range of experimental data for different types of deformation states and strain magnitudes [7]. Several other models, such as the Yeoh model, the Gent model, etc., not reported herein for the sake of brevity, have been also proposed [7, 11].

2.2.2 Physics-based mechanics of polymers: from network chain conformation to the continuum

The statistical mechanics of polymers considers the statistical description of the molecular conformation of its network chains, in the so-called chain configuration space. At the molecular level, a polymeric material is typically constituted of several repeated molecule units, which can form a very intricated entangled structure.

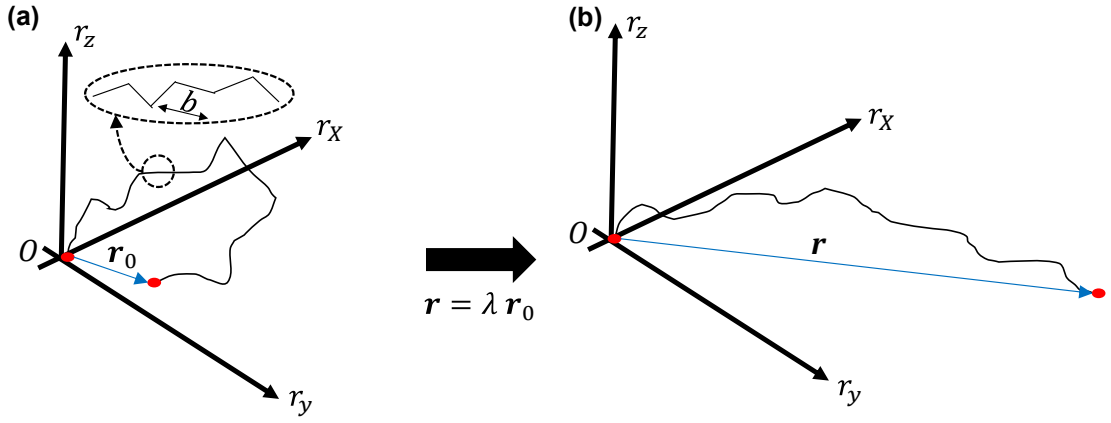

Figure 2.1: *Polymer chain in the chain configuration space, in the (a) undeformed and (b) deformed configuration, respectively.*

The polymer network can be reasonably assumed to be made of long polymer chains, joined together at cross-link sites (or junction points), each one made of N rigid Kuhn's segments with equal length b. The spatial orientation of each Kuhn's segment is assumed to be random (freely jointed chain model, FJC) [6]. The geometrical conformation of each chain can be represented by the so called end-to-end vector $\mathbf{r} = (r_x, r_y, r_z)$, linking the two ends of the chain, Fig 2.1.

By considering an isotropic polymer network in the reference stress-free state, the statistical distribution of the end-to-end vector can be expressed according to the Gaussian statistics as:

$$\varphi(\mathbf{r}) = \left(\frac{3}{2\pi N b^2}\right)^{3/2} \exp\left(-\frac{3|\mathbf{r}|^2}{2Nb^2}\right) \tag{2.17}$$

with mean value at $\mathbf{r} = 0$. However, it is worth mentioning that in the undeformed state the most probable distance between the ends of a chain is non zero; in fact, as illustrated in [10], the most probable conformation states of the polymer chains in the stress-free state are those characterized by the mean end-to-end distance $|\mathbf{r}_0| = b\sqrt{N}$, which represents the average end-to-end vector length of a polymer chain in the stress-free state, [2]. In a generic deformed state, in which the polymer chain is subjected to a uniaxial stretch λ, the reference end-to-end vector can be related to the deformed one as $\mathbf{r} = \lambda \mathbf{r}_0$. According to the hypothesis made on the chain structure, a polymer chain can be stretched up to a maximum length of $|\mathbf{r}_{max}| = \lambda_{max}\,|\mathbf{r}_0| = Nb$ (contour length) with $\lambda_{max} = \sqrt{N}$, [2].

The mechanical nature of polymers and polymer-like materials is governed by the entropic energy (S) of the system rather than by the enthalpic one (U). In fact, while the stress-strain relationship in crystalline solids (such as metals, etc.) is governed by the enthalpic energy, the elasticity of polymers stems from changes of entropy at constant internal energy, [8].

The entropy represents a measure of the disorder of a system; by referring to a single polymer chain, when it is stretched its Kuhn's segments orient in the direction of deformation, thus leading to a disorder decrease which corresponds to a reduction of the entropy and a variation of the end-to-end

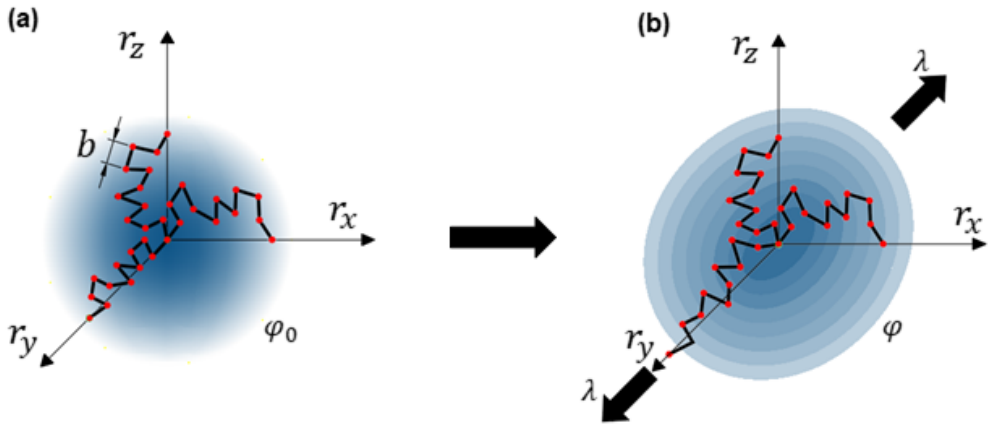

Figure 2.2: *Statistical distribution of the chains of a polymer network in the (a) reference and (b) in a generic deformed state, respectively. Three chains lying along the cartesian axes are also schematically illustrated in the reference (stress-free) state and when a stretch along the y-axis is applied.*

vector. By defining the free energy of a single chain as ψ_c [10]:

$$\psi_c = U - TS \tag{2.18}$$

and by differentiating, it happens to be $d\psi_c = dU - TdS$ at constant temperature. Moreover, by exploiting the first and the second law of thermodynamic:

$$d\psi_c = dW_c \tag{2.19}$$

where dW_c represents the infinitesimal work done by the external forces acting on the chain. As recalled above, no internal energy variation occurs ($dU = 0$), therefore:

$$d\psi_c = dW_c = -TdS \tag{2.20}$$

The entropy variation dS of a thermodynamic system can be evaluated according to the statistical theory developed by Boltzmann, as $dS = k_B \ln \frac{\Omega}{\Omega_0}$, where Ω and Ω_0 represent the number of conformations of the chain in the current and in the reference state, respectively [6, 12]. When the system is constituted by a generic individual chain, the number of possible conformational states can be evaluated according to Eq. 2.17; therefore, by assuming $\Omega = \varphi(\mathbf{r})$ and $\Omega_0 = \varphi(\mathbf{r} = \mathbf{0})$, it follows:

$$dS(\mathbf{r}) = k_B \ln \frac{\varphi(\mathbf{r})}{\varphi(\mathbf{0})} = -\frac{3k_B|\mathbf{r}^2|}{2Nb^2} \tag{2.21}$$

and by using Eq. 2.20:

$$\psi_c(\mathbf{r}) = \frac{3k_BT}{2Nb^2}|\mathbf{r}^2| \tag{2.22}$$

which represents the free energy of a single chain based on the Gaussian statistics.

Similarly, but adopting the Langevin statistics, the following free energy can be obtained [13]:

$$\psi_c(\mathbf{r}) = Nk_BT\left[\frac{|\mathbf{r}|}{bN}\beta + \ln\frac{\beta}{\sinh\beta}\right] \tag{2.23}$$

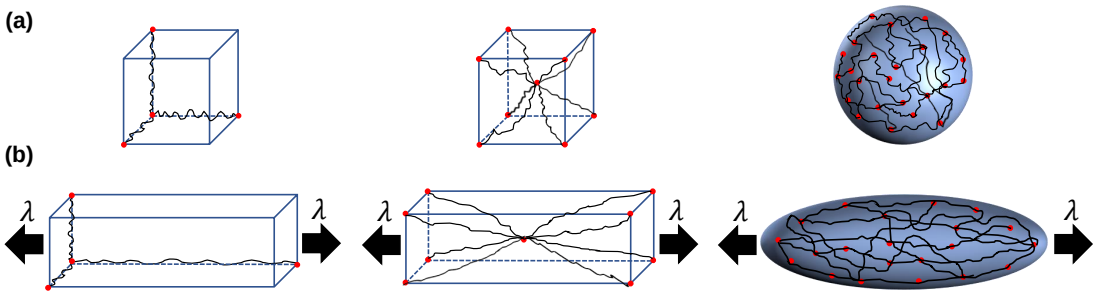

Figure 2.3: *Scheme of different models of polymer networks (from left to right): the 3-chain model, the 8-chain model and the full network model, in the (a) reference and (b) in a generic deformed configuration, respectively.*

being $\beta = \mathscr{L}^{-1}\left(\frac{|\mathbf{r}|}{bN}\right) = \mathscr{L}^{-1}\left(\frac{\lambda}{\sqrt{N}}\right)$, with $\mathscr{L}(\blacksquare) = \coth(\blacksquare) - (\blacksquare)^{-1}$ the Langevin function, [13, 14].

An interesting extension of the FJC model can be found in [15] (EFJC model), where the mechanics of a polymer chain is described by removing the hypothesis of rigid Kuhn's segments, i.e. by treating them as elastic elements; in this case, the free energy of a single chain is expressed by:

$$\psi_c(\mathbf{r}, \lambda_b) = N k_B T \left[\frac{|\mathbf{r}|}{N \lambda_b b} \beta_b + \ln \frac{\beta_b}{\sinh \beta_b} \right] + N \varepsilon_b(\lambda_b) \tag{2.24}$$

where λ_b denotes the Kuhn's segment stretch arising from the deformation of the constituent monomers, associated to the internal energy ε_b (enthalpic contribution to the free energy), while $\beta_b = \mathscr{L}^{-1}\left(\frac{|\mathbf{r}|}{N\lambda_b b}\right)$. Differently from the previous models, the free energy of a single chain is now given by an entropic and an enthalpic contribution. By increasing the deformation, the entropy of the system decreases whereas the enthalpic contribution, related to the monomer stretch λ_b, increases. This interplay has a solution corresponding to an optimum value of λ_b which minimizes the free energy; it can be evaluated by requiring $\partial \psi_c / \partial \lambda_b = 0$, which provides an implicit equation whose solution leads to λ_b, [15].

Finally, the force acting on a chain can be evaluated by the derivative of its free energy with respect to $\mathbf{r}$, i.e. $\mathbf{f}(\mathbf{r}) = \frac{\partial \psi_c}{\partial \mathbf{r}}$:

$$|\mathbf{f}| = \begin{cases} |\mathbf{f}(\mathbf{r})| = 3 k_B T \dfrac{|\mathbf{r}|}{N b^2} = 3 k_B T \dfrac{\lambda}{b\sqrt{N}} & (2.25) \\ |\mathbf{f}(\mathbf{r})| = k_B T \dfrac{\beta}{b} = k_B T \dfrac{\mathscr{L}^{-1}\left(\frac{\lambda}{\sqrt{N}}\right)}{b} & (2.26) \\ |\mathbf{f}(\mathbf{r}, \lambda_b)| = k_B T \dfrac{\beta_b}{b\lambda_b} = k_B T \dfrac{\mathscr{L}^{-1}\left(\frac{\lambda}{\sqrt{N}\lambda_B}\right)}{b\lambda_b} & (2.27) \end{cases}$$

whose expressions have been determined according to the FJC model by adopting the Gaussian and the Langevin statistics respectively (Eqs. 2.25-2.26), and the EFJC model (with Langevin statics), Eq. 2.27.

When the statistical mechanics of polymers is considered, one of the main issue relies on the way the statistics conformation of an individual polymer chain is related to the mechanics of the entire polymer network, and in turn on how to upscale these concepts to the macroscopic level (continuum mechanics); different models have been proposed, such as the 3-chain model [13, 16], the 4-chain model [10, 17], the 8-chain model [18] and the full network model [13, 19, 20], see Fig. 2.3.

Let's consider a continuum body made of an incompressible material whose polymer network is made of c_a polymer chains per unit volume (see sect. 2.3), subjected to a macroscopic deformation quantified by the stretches applied along the cartesian directions, i.e. $\boldsymbol{\lambda} = (\lambda_1, \lambda_2, \lambda_3)$.

The simplest 3-chain model assumes the mechanical response of the entire network to be represented by three independent sets of $c_a/3$ individual chains in three orthogonal directions, [13, 21]. By means of the affine deformation hypothesis (according to which the stretches applied to the continuum in certain directions are the same of those applied on the polymer chains embedded in the continuum itself, both in magnitude and directions) and in the context of the Gaussian statistics, the strain energy density of the material can be demonstrated to be [10]:

$$\Psi = \frac{1}{2} c_a k_B T \left(\lambda_1^2 + \lambda_2^2 + \lambda_3^2 - 3\right) \tag{2.28}$$

It is worth mentioning that, being $\mu = c_a k_B T$ [6], the Neo-Hookean model is recovered (sect. 2.2.1).

Within the 3-chain model but using the Langevin statistics, a similar expression has been found [11, 16]:

$$\Psi = \frac{1}{3} c_a k_B T \sqrt{N} \left[\lambda_i \beta_i + \sqrt{N} \ln\left(\frac{\beta_i}{\sinh \beta_i}\right)\right] \tag{2.29}$$

with $i = 1,2,3$ (the sum over the repeated indices is assumed), being $\beta_i = \mathscr{L}^{-1}\left(\frac{\lambda_i}{\sqrt{N}}\right)$.

The 4-chain model as well as the 8-chain model are suitable to describe a more cooperative deformation state; in these models, the affine deformation hypothesis is usually removed; in fact, within these models, the stretch on a chain is effective (since polymer chains deform in a non-affine manner according to the interior junction point of the ideal unit in which they are embedded) though to be still dependent on the deformation applied to the continuum [11] (see below).

In the 8-chain model [18], the mechanical response of the entire polymer network is governed by eight equivalent chains, assumed to be placed along the diagonals of a cubic cell, [11]. The equivalent stretch on each of the eight chains can be evaluated from symmetry considerations to be $\lambda_{chain} = \sqrt{\frac{1}{3}\left(\lambda_i^2\right)}$. By considering the Langevin statistics, the strain energy density of the material is [11]:

$$\Psi = c_a k_B T \sqrt{N} \left[\lambda_{chain} \beta_{chain} + \sqrt{N} \ln\left(\frac{\beta_{chain}}{\sinh \beta_{chain}}\right)\right] \tag{2.30}$$

with $\beta_{chain} = \mathscr{L}^{-1}\left(\frac{\lambda_{chain}}{\sqrt{N}}\right)$.

To summarize, all these models aim at describing the actual spatial distribution of the polymer chains in a simplified way, by attributing the mechanical response to particular chains arrangement.

On the other hand, when a full network model is considered, all the chains constituting the network are taken into account, without any restriction to particular representative directions; the

strain energy per unit volume of the material can be found by integrating the strain energy of each chain, over the entire chain configuration space, see sect. 2.3.

2.3 A micromechanical-based description of polymer-like materials

To describe the mechanical behavior of a polymer-like material, a full network model [19, 22] is adopted across this work. The chains constituting the polymer network are assumed to be randomly distributed in the chain configuration space according to the Gaussian distribution (Eq. 2.17); thus, a distribution function (CCDF, Chain Configuration Density Function) is introduced:

$$\rho(\mathbf{r},t) = c_a(t)\varphi(\mathbf{r},t) \tag{2.31}$$

where $c_a(t) = \langle\rho(\mathbf{r},t)\rangle$ represents the active chain concentration (cross-link density), i.e. the total number of active (those connected at both ends, which are responsible for the material stiffness) polymer chains per unit volume of the material [19], being the operator $\langle\blacksquare\rangle$ the integral of the quantity $\blacksquare$ over the chain configuration space, i.e. $\langle\blacksquare\rangle = \int_0^{2\pi}\int_0^{\pi}\left(\int_0^{\infty}\blacksquare r^2 dr\right)\sin\theta d\theta d\omega$, where $\langle\varphi(\mathbf{r},t)\rangle = 1\forall t$ if damage or self-healing are neglected.

In fact, if no damage or self-healing mechanisms occur, and an incompressible polymer is considered, the number of active chains per unit volume does not change over time, i.e. $\frac{\partial c_a(t)}{\partial t} = 0$ and so $c_a(t) = c_a$. Such an hypothesis is still valid also by considering the viscoelastic behavior of polymers; by modeling the viscoelastic behavior by adopting the concept of bond exchange, the chain concentration is constant at the steady state (i.e. at the time of cross-linking) [19].

The CCDF quantifies the number of active chains whose end-to-end vector falls within the interval $\mathbf{r}$ and $\mathbf{r}+d\mathbf{r}$ [23], being $\mathbf{r} = \mathbf{F}\mathbf{r}_0$, with $\mathbf{F}$ the macroscopic deformation gradient.

In a generic deformed state, the strain energy per unit volume can be evaluated by integrating the free energy of each single chain over the whole chain configuration space [22, 23]:

$$\Psi = \langle\rho(\mathbf{r})\psi_c(\mathbf{r})\rangle + \pi(\det\mathbf{F} - 1) \tag{2.32}$$

where π is the hydrostatic stress introduced for enforcing the incompressibility condition.

In order to have a zero strain energy in the reference (undeformed) state, the energy difference $\Delta\Psi$ must be used [19, 22]:

$$\Delta\Psi = \Psi - \Psi_0 = c_a\langle(\varphi-\varphi_0)\psi_c\rangle + \pi(\det\mathbf{F}-1) = \langle(\rho-\rho_0)\psi_c\rangle + \pi(\det\mathbf{F}-1) \tag{2.33}$$

thus, at $t = 0$ it holds $\Delta\Psi(\mathbf{F} = \mathbb{1}) = 0$.

The current value of the CCDF, is the main quantity to be used for linking the mechanical response at the continuum level to the network arrangement at the molecular scale. In other words, this distribution can be modified by macroscopic deformation (at the continuum level) and

by other phenomena taking place at the molecular level (such as chain detachment-reattachment, nematic-isotropic transition, etc.).

Let's assume a viscoelastic polymeric material to be subjected to a deformation state quantified through $\mathbf{F}$. The CCDF rate can be decomposed as follows [22, 23]:

$$\frac{\partial \rho(\mathbf{r},t)}{\partial t} = \dot{\rho}(\mathbf{r},t) = \dot{\rho}_F + \dot{\rho}_v \tag{2.34}$$

where $\dot{\rho}_F$ and $\dot{\rho}_v$ are the time rates of the CCDF, corresponding to the elastic distortions of the chains and to viscoelastic phenomena (providing chains re-arrangement). They are expressed as [19, 22]:

$$\dot{\rho}_F = -\left(\nabla\rho(\mathbf{r},t)\otimes\mathbf{r} + \rho(\mathbf{r},t)\mathbb{1}\right):\mathbf{L} \tag{2.35}$$

$$\dot{\rho}_v = -k_d\left[\rho(\mathbf{r},t) - \rho_0\right] \tag{2.36}$$

where k_d is the so-called chain dissociation rate which quantifies the number of chains per unit volume which detach from the network (in the current configuration) and instantaneously reattach into the stress free configuration [19].

Once the CCDF rates are known, they can be used for evaluating the current chain distribution function as follows [22]:

$$\rho(\mathbf{r},t) = \rho_0(\mathbf{r}) + \int_0^t \dot{\rho}(\mathbf{r},t)dt = \rho_0(\mathbf{r}) + \int_0^t \left(\dot{\rho}_F(\mathbf{r},t) + \dot{\rho}_v(\mathbf{r},t)\right)dt \tag{2.37}$$

whose knowledge allows computing the actual stored deformation energy (Eq. 2.33). Finally, the stress state in the material can be obtained as follows [24]:

$$\begin{aligned}\boldsymbol{\sigma} &= J^{-1}\mathbf{P}\mathbf{F}^T = J^{-1}\left(\frac{\partial\Delta\Psi}{\partial\mathbf{F}} + J\pi\mathbf{F}^{-T}\right)\mathbf{F}^T = \\ &= \langle\left(\rho-\rho_0\right)\left[\frac{\partial\psi_c}{\partial\mathbf{r}}\otimes\mathbf{r}\right]\rangle + \pi\mathbb{1}\end{aligned} \tag{2.38}$$

which, as indicated by the operator $\langle\ \ \rangle$, requires an integration over the chain configuration space. It is worth mentioning that such an integration can be computationally very expensive.

The conformation of the polymer chains can be also conveniently described by means of the so-called chain distribution tensor; according to [19] it is defined as follows:

$$\boldsymbol{\mu}_0 = \langle\varphi_0(\mathbf{r},t=0)\mathbf{r}\otimes\mathbf{r}\rangle \tag{2.39}$$

$$\boldsymbol{\mu} = \langle\varphi(\mathbf{r},t)\mathbf{r}\otimes\mathbf{r}\rangle \tag{2.40}$$

where $\boldsymbol{\mu}_0$ and $\boldsymbol{\mu}$ are the chain distribution tensors in the reference configuration and in the current one, respectively.

In the context of Gaussian statistics, $\boldsymbol{\mu}_0$ assumes the simple form $\boldsymbol{\mu}_0 = \frac{Nb^2}{3}\mathbb{1}$, as can be demonstrated by integrating Eq. 2.39 over the chain configuration space [19, 25].

By means of the chain distribution tensor, the strain energy difference per unit volume of the material is expressed as follows [25]:

$$\Delta\Psi = \frac{3c_a k_B T}{2Nb^2}\mathrm{tr}\left(\boldsymbol{\mu}-\boldsymbol{\mu}_0\right)+\pi(\det\mathbf{F}-1) \tag{2.41}$$

Similarly to what has been shown for the CCDF, the current value of the chain distribution tensor allows us to compute the stress state in the material; the chain distribution tensor rate is given by:

$$\dot{\boldsymbol{\mu}}(t) = \dot{\boldsymbol{\mu}}_F(t) + \dot{\boldsymbol{\mu}}_v(t) \tag{2.42}$$

where the term related to the elastic deformation is expressed as:

$$\dot{\boldsymbol{\mu}}_F(t) = \mathbf{L}(t)\boldsymbol{\mu}(t) + \left[\mathbf{L}(t)\boldsymbol{\mu}(t)\right]^T \tag{2.43}$$

The current value of the chain distribution tensor can be evaluated by an integration over the time interval $0-t$:

$$\boldsymbol{\mu}(t) = \boldsymbol{\mu}_0 + \int_0^t \left(\dot{\boldsymbol{\mu}}_F(t) + \dot{\boldsymbol{\mu}}_v(t)\right) dt \tag{2.44}$$

Finally, the stress state in the material is expressed as [25]:

$$\boldsymbol{\sigma} = \frac{3c_a k_B T}{Nb^2}\left(\boldsymbol{\mu}-\boldsymbol{\mu}_0\right)+\pi\mathbb{1} \tag{2.45}$$

which does not require any integration over the chain configuration space. The evaluation of the stress state based on Eq. 2.38 is required any time the polymer network undergoes damage, i.e. chains loss takes place [26].

In conclusion, the basic ingredients necessary to describe the mechanical behaviour of polymers and polymer-like materials have been briefly discussed in this chapter.

In particular, the micromechanical-based approach has been illustrated; it will be extended in chapters 4-5 to model the mechanical response of thermally-responsive LCEs and of polymers obtained via photopolymerization, a class of materials suitable to get functional elements with proper programmable mechanical responses.

CHAPTER 3

MORPHING AND PROGRAMMABLE RESPONSE: FROM NATURE TO SYNTHETIC FUNCTIONAL POLYMERS, AN OVERVIEW

Animals, insects, fishes, flowers, plants, or more generally natural structures usually respond to external stimuli capable of triggering particular functionality to perform some tasks, such as to enable self-protection, to perform locomotion or simply to live. This functional behavior stems from an intrinsic programming coded in some natural way within the structures. These structures display intricate natural architectures across the nano-, micro- and meso- scales, whose features are reflected in an impressive range of functional or multifunctional materials properties.

Shape and properties of natural and synthetic materials can be changed over time in response to external stimuli. This is sometimes referred to as morphing. On the other hand, a certain natural or a synthetic material can respond to environmental stimuli in an encoded way, in this work referred to as programmable response, to perform a desired functional behavior, which not necessarily involves change of properties or shapes over time. Many examples related to controlled morphing and programmable response exist in both natural living matter and in synthetic materials.

This chapter is organized as follows: sect. 3.1 illustrates some source of inspiration involving morphing and/or programmable responses taken from the natural world; in each subsections (e.g. in sect. 3.1.1 collective actions inducing functionality, in sect. 3.1.2 camouflage inducing morphing of living organisms, in 3.1.3 morphing inducing locomotion in animals, etc.) an attempt of discussing a parallelism between the natural phenomena and synthetic functional polymer-based materials is drawn. This section aims at providing some insights and intriguing links between programmed phenomena of natural matters, and currently developed synthetic functional polymers-based materials. One of the aims of the present chapter is to identify the features shared between natural matter and synthetic functional polymers, whose development can benefit from

the strategies adopted in nature. Finally, sect. 3.2 presents a brief overview of synthetic responsive-polymer based materials, in order to outline a clear and schematic picture of the current development in the field.

3.1 From naturally programmed matters to functional synthetic polymers inspired by nature

This section illustrates some intriguing insights taken from the natural world, which represent a precious source of inspiration especially in the context of active/functional materials and devices, which has greatly inspired myself during the PhD studies.

Before entering in some intriguing natural functional behaviors and showing some insights of functional synthetic materials, it is worth clarifying the meaning of morphing and programmable response adopted herein. Morphing is a general word that can assume a vast range of different meanings. It is always referred to a time-dependent structure which changes from a certain initial configuration to another one strictly related to the applied environmental stimulus in turn: it can involve shape-change (well-known as shape-morphing in solid mechanics), but it can also involve color and texture variations of a surface (e.g. the ability of camouflage of certain living organisms), stiffness variations, chemical transformations, etc. While morphing is generally strictly related to a change of shape (or feature) because of an applied stimulus and can be often seen as a programmable response (a material can be programmed to morph in a certain way when stimulated), a programmable response not always involves morphing. In fact, a programmable response does not necessarily imply a time-dependent change of the intrinsic properties of a material: for instance, a certain beam-like structural element can be designed in such a way to ensure that its load-displacement curve follows a pre-defined path or displays a particular mechanical response when loaded.

3.1.1 Collective actions inducing functionality: from living materials to super-organisms

New frontiers in the development of active materials with controlled morphing capabilities and programmable response are represented by the so-called living materials; in these matters, the proliferation, movement or tasks performed by living cells embedded in the constituent material matrix, stimulated by environmental cues, can be exploited to get a controlled shape-change or other functional responses, similarly to what occurs in several biological phenomena involved in natural structures [32, 33]. In nature, a well-known example of living material is represented by the yeast: it can provide a growth of the entity in which it is embedded, see Fig. 3.1(a). Inspired by such an active behavior, in [27] an hybrid hydrogel has been developed by embedding *Saccharomyces cerevisiae* (i.e. baker's or brewer's yeast) within a polyacrylamide hydrogel. Such an active composite material proliferates in response to a combination of environmental stimuli by showing a shape

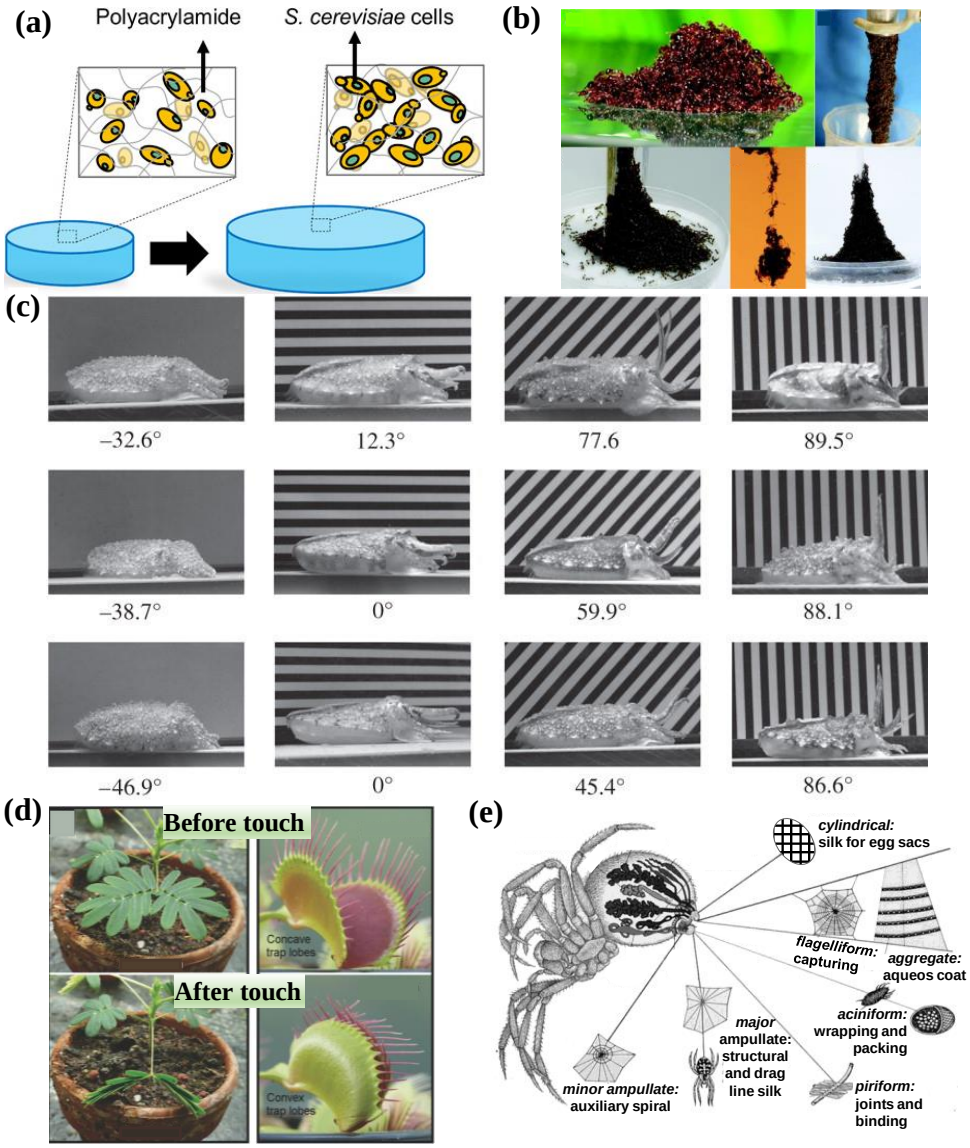

Figure 3.1: *Some examples of naturally programmed structures: (a) Growth inducing morphing of a living natural material under air-exposure. (b) Cluster of fire ants whose overall shapes can change over time for functional purposes (float, food supply, etc). (c) Postural arm camouflage of cuttlefish, illustrating a different bending behavior of cuttlefishes' arm according to the visual background they detect. (d) Active nastic morphing (open-close of the leaf) of a vegetable under mechanical stimulus (touch). (e) Different types of spider silks, each one with encoded tailored physico-chemical-mechanical properties for gaining functionality .* **Copyright: (a) Adapted from Rivera-Tarazona et al. [27], under a Creative Commons Attribution License 4.0 (CC BY) from American Association for the Advancement of Science, Copyright 2020. (b) Reproduced from Foster et al. [28], with the permission from The Company of Biologists Ltd., Copyright 2014. (c) Adapted from Barbosa et al. [29], with the permission of Royal Society (Great Britain), Copyright 2012. (d) Adapted from Poppinga et al. [30], with the permission from John Wiley and Sons, Copyright 2018. (e) Adapted from Vollrath [31], with the permission from Elsevier, Copyright 2000.*

and a volume-change. As shown in [27], the tunability of the mechanical properties of the hydrogel matrix can be exploited to control the proliferation-induced shape change; as experimentally shown, as the stiffness of the hydrogel increases, the volume change provided by the cell proliferation decreases. This decrease may be attributed to the increase of the elastic resistance of the hydrogel matrix to the expanding colonies, resulting in limited cell proliferation. This aspect may be exploited to get controlled morphing by spatially tuning the stiffness of the material, for instance by adopting different exposure to UV light (controlled photopolymerization). Differently, but with some analogy, in [27] a UV light was used to kill living cells in programmed regions, in order to obtain a spatially controlled proliferation leading to a 2D to 3D transformation.

In the world of living materials but scaling up to the human body, a very intriguing example of a living entity showing functional morphing and adaptable programmable response is represented by the bone tissue: its shape, structure, mass and overall mechanical behavior can continuously adapt to external forces. In fact, the bone tissue can be remodelled by exploiting the synergic collective behavior of bone cells (osteoblasts and osteoclasts) in relations to the auto-detected load level; in particular, osteoblasts add bone tissue at locations with high stress while, on the contrary, osteoclasts remove this tissue at locations with low stress levels, [34]. In some way, this represents a sort of functional load-driven-natural build structure. Inspired by this behavior, researchers have developed a composite material that is able to continuously increase its stiffness as a function of force, time and frequency of mechanical vibrations, by exploiting the so-called mechanically controlled polymerization (i.e. a mechanical-driven cross-linking reaction) [35]. In other words, a chemical specie (ZnO) embedded in the polymer matrix acts as mechano-chemical transducer; this specie is able to detect the mechanical stimulus and to promote a chemical reaction of polymerization regulating the cross-link density of the material. This functional response provides a material having a shear modulus distribution dependent on the shaking frequency and the force intensity, enabling the adaptation to mechanical inputs; such a functional behavior, recalls the bone tissue remodelling. The material developed in [35], can adapt its stiffness only via increasing (never decreasing) its shear modulus. The complete dynamic restructuring (i.e. a material which can either increase or decrease its elastic properties, either by cross-linking or de-cross-linking in response to mechanical stimulus) which completely recalls the smart behavior of the bone, remains a challenge [35].

Within the field of living materials, it is worth mentioning the exploitation of so-called biomolecular motors to leverage motions and force of individual cells embedded in bio-materials [36–38], to get a controlled shape-change. In other words, motions and organizations of cells occurring at a microscale level can be exploited to get macroscopic deformation or locomotion. For instance, in [39] a UV-light-induced hierarchical organization of biomolecular motors has been exploited to develop a contractile active network: when the material is not exposed to stimuli, biomolecular motors can be viewed as filaments dispersed in certain way (first level of hierarchical organization) in the material; on the other hand, when the material is exposed to UV-light, those filaments rearrange into a second level of hierarchical organization, inducing a macroscopic contraction of the material.

As shown in [39], these active components can be integrated into engineering systems to promote actuation. A more awkward challenge is represented by the design of the whole engineering system by exploiting biomolecular motors, in such a way that biomolecular motors are not simply integrated into an engineering system but instead they constitute the overall engineering system.

What has been explained so far for living materials is based on the general concept of collective motion, i.e. a form of collective behavior where individual units (cells) can interact in a simple or complex way. In such a collective behavior, a singular cell interacting with many other cells behaves differently from how it would behave if it was alone [40]; in other words, an individual cell action is influenced by other cells actions and all the cells cooperate together to achieve a common goal corresponding to a particular functionality. At a different scale, this approach is very useful to introduce the shape-morphing in groups of individuals in nature. Clusters of social insects, birds, bacteria, volvox, etc., or more generally of natural organisms which used to live in swarms (so called super-organism), can interact in different ways, thus inducing a functional controlled change of the cluster's shape they form. For instance, honeybee swarms can tune their density and surface area to volume ratio to maintain a near constant core temperature despite large fluctuations in the environmental temperature, [41]. Another example in this context is represented by the world of fire ants, incredible cooperators in the animal kingdom: they can organize themselves in a single giant buoyant raft for surviving during floods, as well as creating living bridges or ladders useful for their food supply [42, 43], see Fig. 3.1(b).

3.1.2 Morphing inducing camouflage of living organisms

Camouflage inducing morphing is common among living organisms. It can be recognized as the ability to morph the organism appearance and/or behavior according to changes in the surrounding, for a functional response to occur. Camouflage can be thus exploited to elude visual detection or recognition, but it can be also harnessed for launching signals. Different types of camouflages exist. The most obvious and well-known is the ability of living organism to morph the color, texture or roughness of their skin, such as chameleons that can blend into the background by tuning the arrangement of guanine nanocrystals in the cells to change the wavelength of reflected light. Some aquatic living organisms such as jellyfish, octopus and cuttlefish are able to change color of their skin by exploiting the ability to produce light in response to some environmental stimuli (bioluminescence).

As chameleon changes its color in response to external stimuli, synthetic functional polymer-based materials capable of changing their colors or to emit luminescence, have been developed by exploiting the capability of smart molecules embedded in polymer matrix to switch from different stable states in response to external stimuli, such as mechanical stress. This functionality has been particularly investigated in the field of self-diagnostic polymers, see Sect. 3.2.4 for more details.

In the natural world, it is worth mentioning another type of camouflage in living organisms, i.e. the so-called postural camouflage: living organisms can move their body parts in particular way or

can adapt their bodies' positions (and so basically they can morph the appearance of their shape) in order to camouflage in a specific environment or microhabitat, [29]. For instance, salamanders are known to use their head, tail and legs in multiple postures with an anti-predator functions [44]. In the marine environment, there are lots of example of the so-called shape-morphing camouflage. For instance, cuttlefish and squid can bend their arms according to the visual environment they detect; such a morphing is limited to their arms because of the internal rigid body structure (typically a 2D shape-morphing). A surprising experimental study [29] has investigated the influence of the visualized environment on the posture of the arms of cuttlefish: these organisms were stimulated by distinct backgrounds displaying different textures (either a wall of uniform grey colour or various grey and white alternate strips distributed with different orientation on the wall); cuttlefishes morphed their body regulating their arms position according to the background (stimulus) they detected, see Fig. 3.1(c). More specifically, their arm rotated according to the orientation of the strips texture of the wall, whereas they did not bend when a wall of uniform grey colour was used as background. On the other hand, other marine living organisms such as octopus, lacking any rigid internal structures, can exhibit very complex three-dimensional shape-morphing, [29].

3.1.3 Morphing inducing locomotion in animals

Living organisms, such as soft-bodied animals like octopus, worms, snakes, insects, etc., can functionally morph their shapes in order to perform locomotion in the most disparate environmental conditions they encounter, showing an extreme ability to adaptively morph their body to accomplish such a task, [46].

For instance, looking at air mode locomotions (flight) a very intriguing question arises: how an insect is able to fly in presence of both rest air as well as of turbulence? In this sense the air movement can be viewed as an external stimulus: it can be static, unsteady or fully turbulent (in presence of wind), but still the insect can fly, even if with some limitations [47]. This functional response relies on passive and active morphing of wings and body kinematics, allowing to stabilize the body posture during aerial perturbations, [48]. Passive morphing of wing kinematics is typically related to elastic deformations of wings arising because of the interplay between wings' material properties and inertial effects as well as aerodynamic forces [49]; on the other hand, active morphing is related to the animal body-parts shape-change induced by the sensomotor system, harnessing muscle activation [50].

In terrestrial motion, the morphing inducing locomotion on land (such as walking, running, crawling, jumping, etc.), involving contact with a solid substrate, can be influenced by the features of the substrate itself, such as roughness, texture, geometry, mechanical properties, etc., [47, 51–54]. For example, in [51], the locomotions of ants has been demonstrated to be influenced by the roughness' sand: ants move significantly faster and their trajectories were slightly more sinuous on fine sand rather than on coarse sand. Morphing inducing locomotion of aquatic organisms can be influenced by hydrodynamic mechanisms, such as vortices or other hydrodynamic stimuli which can

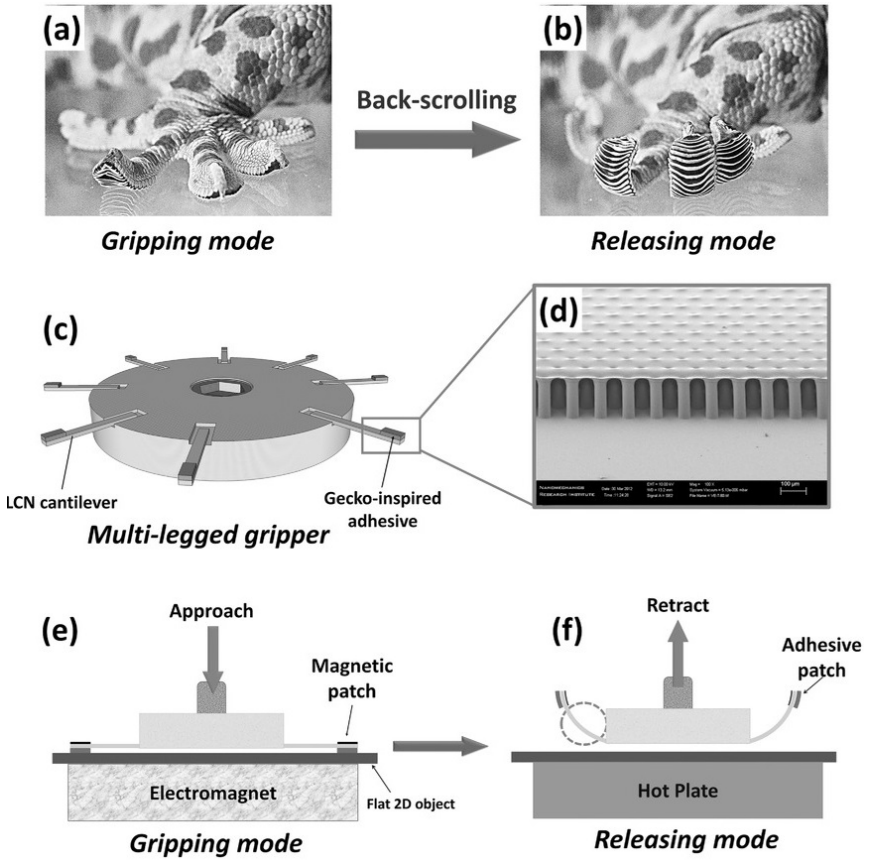

Figure 3.2: *Images of Gecko toes during (a) gripping mode and (b) releasing mode. (c) Scheme of the functional multilegged LCE gripper with (d) a zoom of the biomimetic film-terminated fibrillar adhesives structure. (e) Mechanism of gripping promoted by an electromagnetic stimulus and (f) releasing induced by thermally-driven deformation of the LCE network. Adapted from Shahsavan et al. [45], with the permission from John Wiley and Sons, Copyright 2016.*

affect the swimming performance.

Functional morphing of animals' structure inducing locomotions has inspired researchers and engineers in developing synthetic responsive polymer-based material which, to some extent, are able to mimic these natural features. For instance, an hybrid adhesive-LCE cantilever to mimic both the attachment/gripping and detachment/releasing mode of the gecko toes during its locomotion has been developed in [45]. The functional multi-legged gripper has been realized by assembling several cantilevers whose structure was entirely realized with LCE material, while at one extremity, a gecko-inspired magnetic adhesive was used. The developed hybrid material exploits an electromagnetic stimulus applied on a substrate to allow the gecko-inspired adhesive attachment to flat objects (attachment/gripping mode of the Gecko). On the other hand, it exploits a thermally-driven stimulus to induce bending of the LCE part (see sect. 3.2 for more details), so causing peeling of the adhesive patch (detachment/releasing mode of Gecko), see Fig. 3.2. Such an engineering system must fulfil some basic criteria in order to perform gripping and releasing; for gripping, the magnetic field

must be sufficient to impose the necessary adhesive strength between the adhesive patch and the flat object. In fact, the magnetic stimulus is exploited only for gripping to occur while, when it is removed, a pure adhesion strength takes place. On the other hand, for releasing, the bending deformation induced by the LCE must be high enough to trigger crack-like detachment during peeling.

Inspired by locomotion of living organisms, in [55], a light-driven liquid crystal polymer-based swimming robot has been designed; it exploits a periodic and reversible transformation of trans/cis isomeric azobenzene liquid-crystal moieties. Such a transition occurring upon light irradiation, induces a reordering of liquid-crystal moieties that provides bending upon UV-light exposure [56, 57] (see sect. 3.2 for more details). In particular, when a white light is irradiated the azobenzene liquid crystal moieties stay (or return) to the trans configuration (flat configuration at the macroscale) while when a UV-light is used the trans-cis transition occurs and the material bends, see Fig. 3.3. The developed miniaturized robot can be controlled by different sources of light by means of periodic and synchronized ON-OFF cycles, inducing the capability of swimming (Fig. 3.3).

3.1.4 Morphing in plants and vegetables

Morphing because of moving or growing in response to external stimuli, exists in the natural kingdom of plants and vegetables. Morphing in plants can be generally subdivided into two types: tropic and nastic, [58]. Tropic movements, which are typically represented by plants growth, are associated with the stimulus direction. A typical tropic morphing can be recognized in the roots growth: in the underground, roots come out of the seed and spreads in the direction of the water (i.e. the stimulus). Sunflowers' head moves during the day according to the position and direction of the sunlight (sun-tracking), providing an example of tropic movements. Nastic morphing is referred to something which occurs because of an external stimulus but whose responsiveness is not stimulus-direction-dependent. For instance, the ability of some plants to close leaves for capturing insects by simply responding to a touch-type stimulus, is an example of nastic movement, see Fig. 3.1(d); there is no a directional relationship between stimulus and response, so the responsiveness occurs regardless of the position of touching (laterally, from above, from below, etc.). The so called "sleep movement" of some plants which can move their leaves during night is another example of nastic movement, [59]. From a certain point of view, nastic movements always follow the same kinematical "patterns", irrespectively of the direction of the applied stimulus.

In the field of functional materials inspired by plants (sometimes referred to as "plant bionics"), modern polymer-based materials have been developed and used for reproducing the complex plant structures by exploiting the new Additive Manufacturing (AM) technologies. According to [60], the two representative research directions in this field are (1) development of water-driven materials for simulating the morphological changes of plants and vegetables and (2) development of light-driven or heat-driven materials for simulating the blooming process of flowers. The implementation of the smart behaviors of plants into daily-life or advanced applications, represents an intriguing challenge

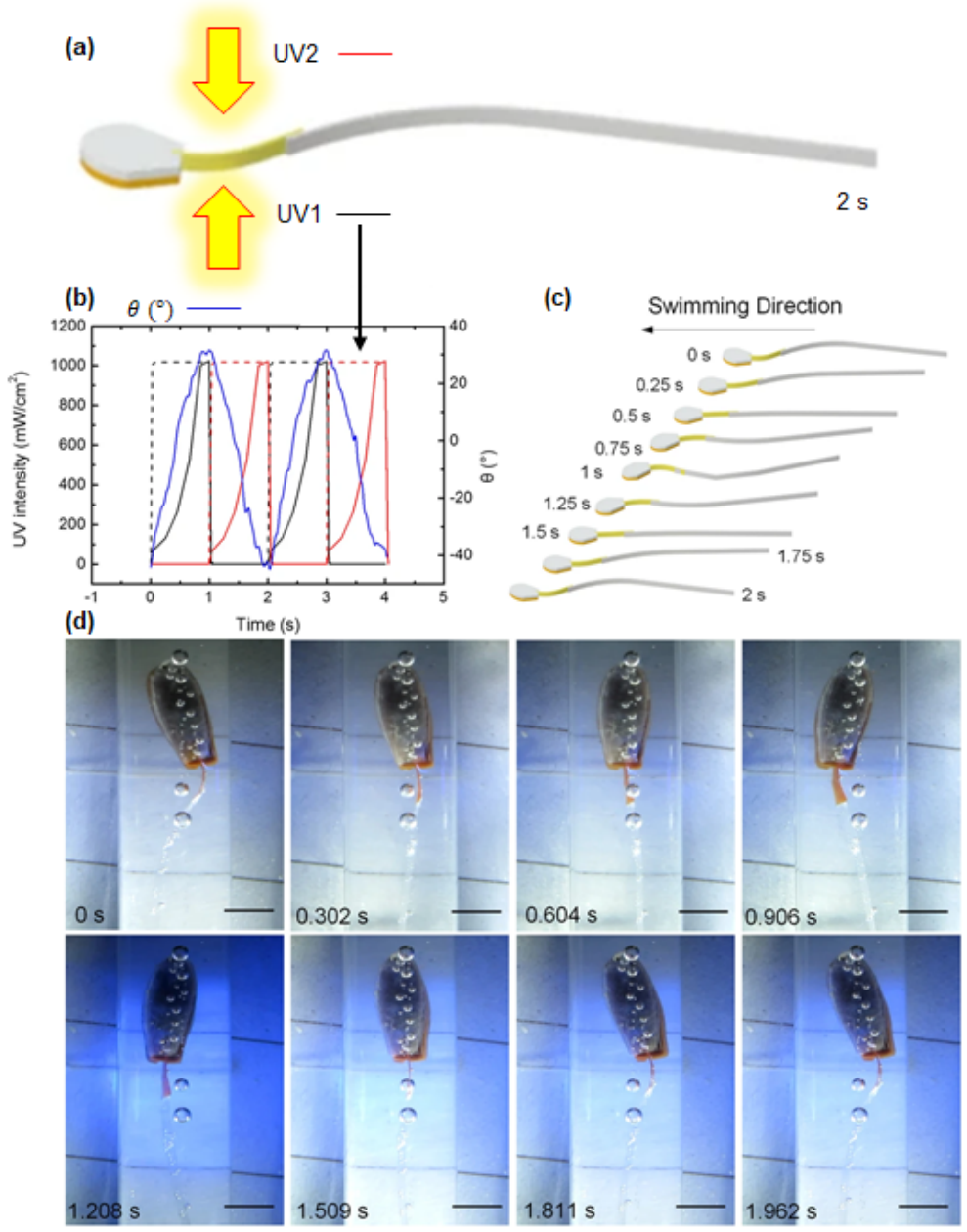

Figure 3.3: *(a) Deformed configuration of a LCE-based-robot during swimming, with illustration of the light irradiation system. (b) Plot of the UV light intensity vs bending angle. (c) Scheme of the swimming locomotion and (d) experimental images showing the periodic swing of the LCE-based-robot. Adapted from Huang et al. [55], under Creative Commons Attribution License 4.0 from Springer Nature, Copyright 2015.*

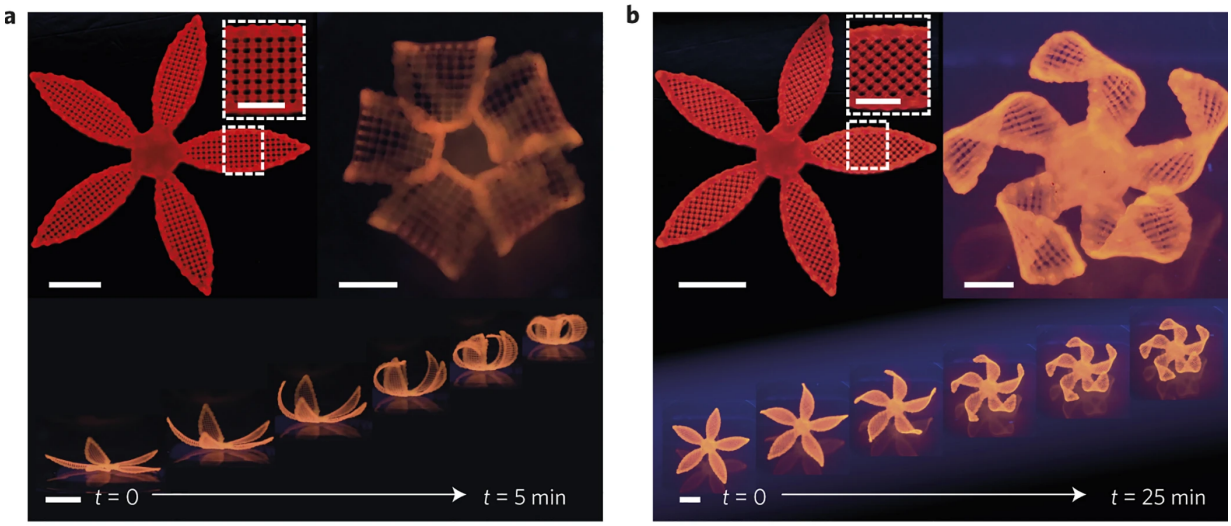

Figure 3.4: *Flowers composed of (a) 90°/0° and (b) -45°/45° bilayers, with respect to the long axis of each petal. Each figure shows both the printed architecture of the flower as well as the time-dependent shape-changing provided by the anisotropic swelling due to fluid uptake (upon flower immersion in water). Adapted from Gladman et al. [61], with the permission from Springer Nature, Copyright 2016.*

to be faced. One of the earliest intriguing research in this field was conducted by the Jennifer Lewis' group at Harvard University: inspired by plants exhibiting hydration-triggered changes in their morphology because of differences in local swelling, they developed a biomimetic hydrogel composite with encoded localized swelling anisotropy that induces complex shape changes upon immersion in water, [61]. In fact, the stiffness of fibrils within plant cell walls induces differences in the elastic properties of the natural structures which provide anisotropic swelling, more intensely in the direction perpendicular to the fibrils. In this way, in [61], an hydrogel composite ink made of stiff cellulose fibrils embedded in a soft acrylamide matrix (which mimics the composition of plant cell walls) was used for printing different architectures. The possibility to easily align fibrils as well as to realize bilayer configurations enabling bending (due to strain mismatch between different layers) by exploiting AM technology, has enabled the production of complex architectures with different elastic properties, see Fig. 3.4.

3.1.5 Morphing for protection of living organisms

Basically, in nature three strategies exist for protection: hiding (camouflage, see sect. 3.1.2), running and so escaping (locomotion, see sect. 3.1.3) or exhibiting specific actions for protection. An example of the last behavior (morphing for protection) in nature is that shown by the pillbugs *Armadillidum vulgare*, which can morph by rolling and closing into a ball. This conglobation behavior is triggered by strong vibrations or pressure promoting morphing into an external spherical shell for protection, [62]. From a mechanical viewpoint, such a conglobation mechanism can be considered a mechanically

unstable-like response. In the field of functional synthetic materials, a research direction harnessing the instability mechanisms (buckling) for developing smart materials and structures has been deeply studied [63]. In this context, despite usually instability is dangerous for structures and materials, buckling can be exploited to get a desired response. For instance, silicon-based shell structures patterned with a regular array of circular voids and mechanically stimulated by controlling the difference between internal and external pressure were fabricated in [63]. Below a critical pressure, the narrow ligaments between the voids exhibit buckling, leading to a synergistic buckling cascade, inducing the closure of the ball structures (encapsulation), mimicking the conglobation exhibited by the *Armadillidum vulgare*.

3.1.6 Programmable response: complex structural design built by insects

Programmable response does not necessarily mean a time-dependent change of properties or shapes. For instance, the mechanical response arising in different types of spider silks is an example of programmable response. In fact, spiders can build up to seven types of silks used for various biological functions (reproduction, locomotion, prey capture, etc.) [64]. Spider silk can exhibit a large diversity of mechanical properties which are naturally-programmed and optimized for performing specific functions, [31, 65]. Generally speaking, spider silks can have different chemical-physical-mechanical-geometrical properties, according to the functional purpose they are devoted to; each specific type of a spider silk is naturally programmed (and so designed and built) in order to properly meet its needs, see Fig. 3.1(e). The dragline thread (or major ampullate, MA thread), to be used for escaping from a predator, is characterized by a combination of strength and extensibility providing an incredible toughness, greater to that shown by modern industrial materials, including Kevlar. The flagelliform silk constitutes the core thread of the spiral in spider web: its tensile strength is lower than the MA thread but it is much more extensible; together with the aciniform silk, it is used for wrapping preys caught in the web. The minor ampullate silk is used for stabilizing the platform during web construction, etc.

Structures built by bees consist of large arrays of regular hexagons used as nest. Bees' honeycombs are capable of supporting large masses; each kilogram of beeswax is capable of supporting about 22 kg of honey [66]. Furthermore, honeycomb cells are geometrically arranged in a precise way in order to achieve functionality: regular hexagons have the smallest perimeter within polygon family that fills a plane without gaps, making them the most efficient geometry for packing honey, pollen, and brood. Moreover, the surface of the walls of the honeycoomb cells are not perfectly horizontal: they form an angle of about 9°-14° above the horizontal plane to prevent honey from leaving out of uncapped cells [66]. Bees can make their wax less strong, more easily susceptible to fracture and more deformable at high temperature in order to facilitate its use for building purposes. Nests made entirely of pure wax completely collapse around at 45°C [66]. For this reason, after comb cells have been built, fertilized eggs are deposited: larvae which emerge from the eggs surround themselves with silk cocoons before their pupation; this noticeably improves the mechanical

response of the nest in terms of tensile strength, breaking strain, stiffness and toughness. Thus, their structural integrity at 45°C noticeably surpasses that of the pure wax at the same temperature [67, 68]. Even though the pure beeswax has not good mechanical properties, the whole design and building process of an honeycoomb is naturally-programmed and optimized in order to provide a structure with the desired mechanical response and functionality.

Like the functional mechanical behavior of spider silks or honeycoombs, novel materials and structural systems with programmable response are highly desirable in several engineering applications. For instance, in [69] composite structures obtained through a multi-material topology optimization method have been designed to achieve a vast range of programmed force-displacement response under finite deformations. Structural elements developed in [69] have been functionally designed to respond in a specific tailored way to external actions (programmable response): they deform in a pre-designed way when stimulated or show a specific target force-displacement curve. Other approaches, based on material topology, have been used for obtaining programmable response such as in the cases of auxetic materials [70, 71], energy-absorbing materials [72], materials with tunable elastic properties [73] and tunable deformation [74].

3.2 Synthetic functional polymer-based materials

Inspired by nature, engineers and scientists have been developing smart polymers for advanced applications, that can respond in a tailored way to environmental stimuli such as temperature, light, pH, electric fields, chemical, mechanical, etc. This section is aimed at providing a schematic summary in the realm of functional synthetic polymer-based materials.

The first aspect to be considered when dealing with functional materials is how to classify them; unfortunately, such a classification is not trivial and cannot be done in a unique way. For instance, functional materials may be grouped by considering the stimulus providing their responsiveness. However, such an approach could be not appropriate by considering that, in some cases, a same functional material can respond to different types of stimuli.

Another choice could be a classification based on the speed in exhibiting the functional responses: for instance, generally speaking, the shape-morphing induced by the swelling phenomenon in polymer networks is typically slower than that provided by the nematic-isotropic transition occurs in liquid crystal polymers. This aspect is quite important when dealing with soft-robotics, where the speed of responsiveness could be crucial.

In this section, functional polymer-based materials are grouped by following a classification based on the different type of mechanism inducing the functional response: Sect. 3.2.1 illustrates liquid crystal-based (LC) polymers whose functional response is based on the order-disruption of LC mesogens. Sect. 3.2.2 deals with the swelling-driven hydrogel structures. Sect. 3.2.3 illustrates functional polymers whose functionality comes from the interaction between the polymer matrix and electric charges and/or ions (Electroactive polymers). Sect. 3.2.4 is devoted to the functional

behavior of polymers with embedded smart molecules. Finally, Sect. 3.2.5 illustrates metamaterials and topological-functional-based polymers.

3.2.1 Liquid crystal polymer networks

Liquid crystals elastomers (LCEs) are unusual materials belonging to a state of matter that lays between the crystalline solid state (ordered) and the amorphous liquid state (disordered). They are typically made of relatively stiff rod molecules with a well defined orientational order; such an order can be functionally modified (distrupted) by applying stimuli, such as heat, light or solvents. Therefore, such an order-disorder switching represents the mechanism enabling the functionality of liquid crystal networks. Typically, a standard polymer network is characterized by a microstructure made of chains randomly arranged (coil-state or isotropic-state); it can become ordered (nematic) by exploiting the incorporation of aligned rigid units of liquid crystal (mesogens). In the nematic state, the resulting polymer network exhibits a preferential orientation of the polymer chains according to the direction (nematic director) displayed by the LC units.

The microstructure of a LCE material, characterized by a particular conformation of polymer chains, can be changed over time due to stimuli capable of changing the mesogens arrangement from ordered to isotropic and vice versa. This microscopic change induces the appearance of strain detectable at the macroscopic level. During an isotropic-nematic transition, polymer chains either elongate in a specific direction (parallel to the nematic director) while they contract in the perpendicular directions. On the other hand, during the reverse transition (i.e. nematic-isotropic) a random-coil conformation is recovered, corresponding to a contraction along the direction parallel to the initial nematic director and an elongation in the other directions [75], see chapter 4 for further details.

The nematic-isotropic transition in LC polymer networks can be driven by heat (thermo-mechanical response), light (photo-mechanical response) and by hybrid mechanisms (indirect heat) such as the photo-thermal-mechanical response.

In thermo-responsive LCEs, heat is used to induce the order disruption of LC mesogens in the polymer network. In such a case, LC mesogens (and so the polymer chains) below a critical temperature value (the so-called nematic-isotropic transition temperature) are in the nematic state. When the material is heated above this temperature, the nematic-isotropic transition occurs and the polymer network changes its conformation from the nematic state to the isotropic one, inducing a macroscopic deformation. As it has been experimentally shown in literature, this mechanism can be used in bilayer structures with different orientation of mesogens [76], or by exploiting the cross-link-density-actuation dependence [77], etc. (see the micromechanical model presented in chapter 4), to get simple bending or other intriguing shape-changes.

In photo-responsive LCEs, a chemical transformation induced by a UV light provides a conformational change triggering the order-disruption of the mesogens; this occurs for instance in the trans-cis isomerization of azobenzene mesogens [55]. Differently from thermally-driven LCEs,

light-driven LC networks have shown a bending responsiveness even in sample with unidirectional aligned moieties (regardless any effect of the cross-link density related responsiveness). This effect can be explained by the material absorbance: in fact, because of the large concentration of azobenzene in most LCEs, the strong absorbance of the material localizes the response at the surface irradiated by the light or in its immediate neighborhood, resulting in bending [75] due to a localized order disruption.

The photo-thermal-induced response is in between the two above mentioned responses: typically, it exploits a light stimulus for indirectly heating the material, and thus for inducing the standard thermally-driven transition. Differently from the above discussed photo-induced response where light modifies the chemical structure of the moieties, in photo-thermal response no chemical changes occur. Thanks to their high photothermal conversion efficiency, several photo-thermal agents have been recently employed for inducing a photo-thermal response in LCEs, such as gold nanoparticles (GNPs), gold nanorods (GNRs), carbon nanotubes (CNTs), graphene, iron oxide nanoparticles etc., [78, 79].

3.2.2 Swelling-driven in hydrogels

Hydrogels can be considered to as functional materials; they are used in a wide range of applications, such as soft-robotics, drug delivery, tissue engineering, etc. The most known and exploited mechanism to get functionality from hydrogels is their swelling-deswelling behavior, i.e. the ability to swell or shrink when interacting with a certain solvent.

Hydrogels can be defined as solvent-friendly materials. In fact, due to the particular conformation of their microstructure and their chemical-physical hydrofilic properties, they allow solvent molecules to enter into their network, thus inducing swelling (expansion). In order to control this response or for obtaining multi-stimuli responsive materials, some modification in the responsiveness of hydrogels have been investigated, and so thermal-responsive, pH-responsive, light-responsive, etc. hydrogels, have been developed.

For instance, thermal-responsive hydrogels shrink/swell by fluid uptake when the temperature crosses the lower/higher critical solution temperature (LCST/HCST). In other words, the polymer-solvent affinity can be controlled by means of the temperature. A well-known example of a thermal-responsive-swelling-driven polymer based material is represented by the poly(N-isopropylacrylamide) (PNIPAm) [80]. Analogously, in pH-driven hydrogels the affinity of the hydrogel matrix is typically controlled by means of pH-variation.

Thanks to the possibility to control the swelling behavior of hydrogels, they have been used in many applications, such as in drug release devices. By exploiting different mechanical responsiveness of hydrogels, intriguing shape-change has been achieved as shown in synthetics flowers bionics [61].

3.2.3 Electroactive polymers

Polymers whose shape-change can be triggered by electrical stimuli, Electroactive polymers (EAPs), have been also proposed. According to the specific chemical-physical mechanism triggering the functional response, EAPs can be subdivided into two sub-classes: (1) electric EAPs (piezoeletric polymers or dielectric elastomers), whose functional response is driven by electric fields or Coulomb forces, and (2) ionic EAPs whose response is instead related to the mobility and/or diffusion of mobile ions embedded in the polymer matrix, [81].

Piezoelectricity, the physical property of providing voltage in response to a deformation, was discovered in 1880 by Pierre and Paul Jacques Curie. The capacity of certain types of natural crystals (such as quartz, tourmaline, etc.) to display a voltage on their surface upon mechanical compression was observed. Later on, the reverse effect, i.e. the possibility to obtain deformation upon an electric stimulus, was discovered. This fact has opened new frontiers in the development of electric EAPs. By embedding in the polymeric matrix, which is typically a dielectric material (i.e. a very poor conductor), some conductive fillers such as graphene, Carbon nanotubes, carbon black and other materials, the piezoelectric performance can be improved, [80].

In polymeric structures with integrated piezoelectric ceramics responsible for the piezoelectric effect, the piezoelectric actuation is associated with tensile or compressive stress that distorts the distribution of charged atoms within the structure of the material. On the other hand, the piezoelectric response of pure polymeric materials is the result of a transformation occurring at the molecular-scale based on the presence of permanent molecular dipoles capable to reorient, align and maintain their alignment when electrically stimulated. [80].

Dielectric elastomers are elastomeric materials that have been synthesized in a functional way to be electrically active; this is typically obtained by ionic charges surface coating or by inserting an elastomeric film between compliant electrodes [80, 82]. The mechanical response of dielectric elastomers is provided by the application of an electric fields: this triggers the attraction of opposite material surfaces resulting in an electrostatic compressive force on the elastomer film and on a corresponding lateral expansion because of the incompressibility of the material. A rigorous discussion on this topic from a mechanical viewpoint can be found in [82].

Differently from electric EAPs whose response is related to electrostatic forces, ionic EAPs are electro-chemical materials whose mechanical responsiveness is related to the mobility of the constituent ions. Their behavior is strongly related to the nature of the constituent ions and to the way they are embedded in the polymeric material, [80]. The mechanism inducing functionality in ionic EAPs is based on the mobility of the ionic species: upon application of an electric stimulus, the ionic species redistribute within the polymer thus providing an osmotic pressure gradient across the thickness responsible for producing large bending. It is worth mentioning that, since the mechanical response of ionic EAPs is based on the mobility and diffusion of the ionic species within the material, the actuation speed can be slow (fraction of seconds) in comparison to electric EAPs who instead can actuate even in fraction of milliseconds. On the other hand, compared to electric EAPs which

require high voltage to induce deformation, ionic EAPs show large actuation even with low voltage [83].

3.2.4 Polymers with embedded switchable molecules

Embedding smart molecules (switchable molecules) within a polymer matrix, can result in materials with some peculiar and intriguing responsiveness [14, 84–87]. The mechanism inducing functionality typically consists in a switching (triggered by external applied stimuli such as light, temperature, fluid uptake, mechanical stress, etc.) of the embedded molecules from one stable state to another (see Fig. 3.5), which may also result in a macroscopic detectable deformation.

Stress-sensible molecules (mechanophores) have been investigated especially in the field of self-diagnostic polymers. Approaches based on the introduction of mechanochromic molecules, usually excimer-forming dyes capable of changing color upon mechanical stress, can be harnessed to quantify deformations and detect damage in polymer matrices. For instance, the mechanically-induced transition of Spiropyran molecules (first stable state, typically colorless) into Merocianine molecules (second stable state), the latter being characterized by a detectable color, is well-known [84, 85, 88].

Despite this interesting property, the color change in self-diagnostic polymers is difficult to be measured, and change of colors appears for very high level of strain. Other approaches in this field have been proposed, such as those based on supramolecular mechanoluminophores using the so-called host-guest technology, [89]. Supramolecular mechanophores embedded in the polymer matrix are held together by weak interaction forces; in the stress-free state these host-guest complexes are non-emissive (no fluorescence is emitted). Upon stretching, host-guest complexes dissociate, i.e. the guest chemical specie detach from the host inducing a fluorescence light emission. This supramolecular technology has shown to provide smart polymeric materials whose damage detection capabilities are effective also for low strain values. Although switchable molecules are well-known in the field of self-diagnostic polymers, their functionality can be also exploited for other purposes. For instance, some mechanophores can change their geometrical conformation after reaching a threshold strain. Since mechanophores behave as energy absorbers, they can be added to polymeric matrix to enhance the toughness of the polymer network [90]. In practice, when mechanophores are integrated into a polymer chain, such a chain elongates more than its contour length (related to the number of Kuhn's segments) without exhibiting rupture [90]. The same geometrical conformation change may be also potentially exploited for developing molecular-scale auxetic materials which expand in the directions perpendicular to that of the applied tensile stretch; however, this behavior has not been yet demonstrated by experiments. For this reason, mechanophores with a large stored length are desirable for the development of new materials, [90, 91].

Among the research studies carried out in this thesis in the field of responsive materials, the model of the mechanics of polymers with embedded switchable molecules has been also developed [14, 84–87], despite it does not fall exactly within the leitmotif of the present dissertation. In the

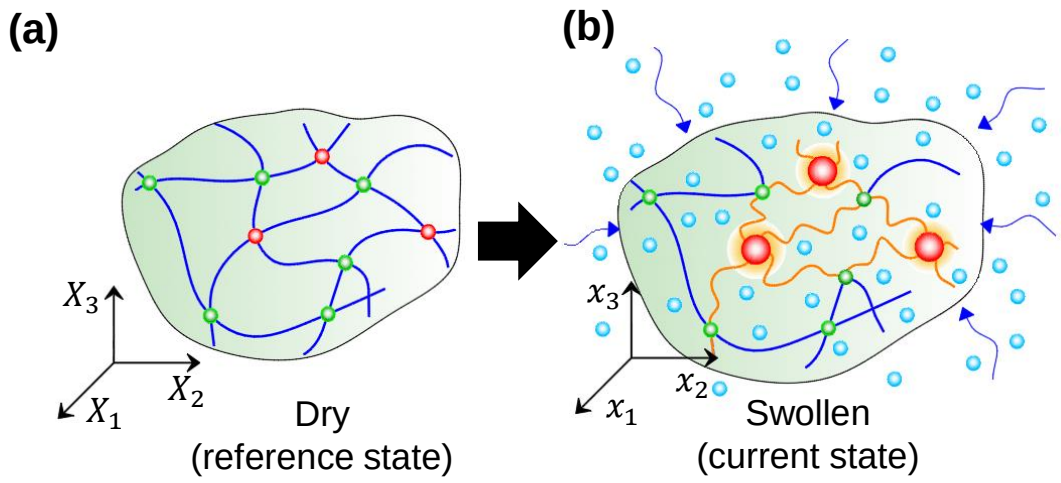

Figure 3.5: *Polymer network with embedded switchable molecules whose activation is triggered by fluid uptake; the figure displays the material in the (a) dry (reference state) with un-switched molecules and (b) in the swollen (current state) characterized by active molecules.*

following part of this subsection, a brief outline of the research done in this context is presented. The mechanical response of polymers containing embedded switchable molecules which can be activated by both chemical agents and mechanical stress, has been mathematically described. The corresponding chemical and mechanical activation mechanisms interplay has been considered in the micromechanical model [14]. When a solvent enters into a polymer network containing un-switched molecules (inactive state), the material expands its volume (swelling phenomenon); this induces a tensile stretch of the polymer chains which, eventually coupled with the chemical-induced activation, enables the embedded molecules to switch in the active state (Fig. 3.5), thus providing particular functionalities to the material. To describe this phenomenon, the strain energy per unit volume of material containing a certain amount of molecules in the active state, is written as:

$$\Psi = [\Psi_e(\mathbf{F}) + \Psi_{mix}(C_s) + \Psi_\pi(\mathbf{F}, C_s)] + n_{act}\psi_{rm} \tag{3.1}$$

where $\Psi_e(\mathbf{F})$ and $\Psi_{mix}(C_s)$ are the energy terms related to the purely elastic contribution and to the polymer-solvent mixing phenomenon, respectively, being C_s the nominal concentration (amount of solvent per unit volume) within the polymer, while $\Psi_\pi(\mathbf{F}, C_s)$ is the energy term necessary to enforce the incompressibility condition. ψ_{rm} is the Helmotz free energy of the responsive molecules, typically associated with the energy barrier which must be overcome to promote the molecules switching from one state to another, and n_{act} is the number of activated molecules per unit volume of the polymer (Eq. 3.1), [14]. According to chapter 2, the total strain energy difference per unit volume can be thus evaluated by means of the CCDF by updating Eq. 2.33 as follows:

$$\Delta\Psi = \langle(\rho - \rho_0)\left[(1-\zeta)\psi_c + h(C_s)\,\zeta\,\psi_{rm}\right]\rangle + \pi\left[\det\mathbf{F} - (1 + v_s C_s)\right] \tag{3.2}$$

where ζ is the total volume fraction of switchable molecules contained in the polymer. The last term in Eq. 3.2 is used as usual to enforce the incompressibility condition, being v_s the solvent molar volume. In Eq. 3.2, $h(C_s) = \langle h_r(C_s)\varphi \rangle$ mathematically quantifies the fraction of molecules which have been activated; it can be related to the effectiveness of the detectable functionality induced by the molecules switching (e.g. geometrical expansion level achieved, color change intensity, etc.) [14, 87]. The amount of activated molecules can be evaluated by computing $h_r(C_s)$, i.e. the fraction of activated molecules joined to chains with end-to-end distance $\mathbf{r}$; this parameter can be quantified by a time-dependent evolution law, obtained by solving the classical kinetic equilibrium equation, where the opportune molecules activation mechanisms are accounted for:

$$h_r(t) = \frac{k_A}{k_A + k_D}\left[1 - e^{-(k_A+k_D)t}\right] \tag{3.3}$$

where k_A and k_d are the activation and deactivation rates of the switchable molecules, respectively. The latter parameters can be evaluated as:

$$k_A = k_{A0} \cdot k_{Af} \cdot k_{As}, \qquad k_D = k_{D0} \cdot k_{Df} \cdot k_{Ds} \tag{3.4}$$

where k_{A0} is the activation rate in absence of any triggering stimulus (characteristic of the molecule being used), $k_{Af} = k_{Af}(f(C_s))$ is the activation rate dependent on the force f acting on polymer chains (mechanical activation, provided by the stretch induced by the swelling phenomenon), while $k_{As} = k_{As}(\frac{C_s}{C_{s,a}})$ is the activation rate corresponding to the chemical properties of the solvent (chemical activation, being $C_{s,a}$ the solvent concentration required to activate all the responsive molecules embedded in the unit volume of the polymer). Similar considerations can be done for the deactivation rates k_{D0}, k_{Df} and k_{Ds}, [14].

3.2.5 Metamaterials and topological-functional-based polymers

This last subsection briefly illustrates metamaterials and topological-functional-based polymers (or functionally-graded materials), whose functionality stems from the particular arrangement of materials' unit cells, properties, etc. This topological arrangement can be either at the level of the microstructure as well as at the level of the structural element.

It is worth mentioning that all the previously illustrated functional materials may eventually fall into this category. For instance, LCE networks can be assembled in pattern of several units (LCE blocks) having distinct nematic order. The main mechanism inducing functionality in this case is yet an order-disorder transition but it is also related to the particular arrangement of LCE blocks in the element. This emphasizes how complex and vast the field of functional materials is, and how their classification is non-trivial.

Metamaterials are rationally designed materials made of several tailored building blocks, whose individual properties and space arrangement allows obtaining particular properties of the overall material, [92]. Although the concept of incorporating architecture into materials is not new, recent developments in the field of AM technologies has further promoted the limitless fabrication

possibilities of materials with intricate architectures across different length scales, [93]. Whereas originally the field of metamaterials was mainly based on discovering materials with unusual properties, new classes of metamaterials including shape-morphing, topological and nonlinear metamaterials have recently emerged [94].

Origami/kirigami-inspired metamaterials, whose functionality is based on the principle of folding/cutting and assembling planar or 2D materials to get intricate 3D structures, have shown to provide functionality (such as multistability), extreme large deformations, programmable stiffness, programmable deformations, negative Poisson's ratio, etc. [74, 93, 95].

It is worth mentioning also the concept of topological-based functional materials or graded materials, whose functionality is based on the continuous distribution of material with variable properties. It is worth highlighting that the topological-based functionality can be introduced either at a level of material (for instance by harnessing the particular arrangement of properties within a material) or at the level of the structure. Also metamaterials, which are typically constituted of several units cells of material arranged in a functional way, can be viewed as topological-based materials.

Looking at the material level, it is well known that the microstructure of the material plays a crucial role in determining the material behavior. Engineers and material scientists have typically focused their studies in optimizing the materials' microstructural characteristics to improve the resulting materials' properties [96]. On the other hand, functionally graded materials or topological-based functional materials are produced with a desired non-uniform spatial arrangement for gaining functionality.

An example of topological-based functionality at the structural element level has been given in [69], where composite functional structures based on a multi-material topology have been proposed. Both the structural geometry and the types and amount of different materials constituting the system have been considered in order to achieve the target force-displacement curve; this has enabled the capability of building functional structural system made of highly nonlinear material, characterized by a linear force-displacement response. Another example is represented by the capability to control the distribution of residual stresses arising during the photopolymerization used in the Direct Laser Writing technology (DLW), to provide programmable self-bending response of polymer sheets, [97].

For sake of completeness, it is worth recalling that in the field of polymer-based functional materials, other functional materials have been developed. Their functionality is provided by different mechanisms which have not been discussed herein for the sake of brevity [30, 80].

CHAPTER 4

MORPHING OF LIQUID CRYSTAL ELASTOMERS

Liquid crystal elastomers (LCEs) are relatively new materials capable of enabling the development of elements with intriguing morphing capability, whose tasks can be exploited in the most disparate fields of innovative applications involving functional materials. The aim of this chapter is to develop a physics-based theoretical model suitable to describe the microscale response of the polymer network by considering the effect of the LCE synthesis process.

This chapter is organized as follows: in Sect. 4.1 a brief literature overview and an introductory discussion on LCEs is drawn. Sect. 4.2 presents a micromechanical-based model describing the thermo-mechanical response of LCE materials. Then, the developed micromechanical model is enriched by taking into account the role played by the cross-link density on the responsiveness of LCEs (see Sect. 4.3). The Finite element implementation of the proposed model is presented in Sect. 4.4. In order to validate the proposed model, results obtained by numerical simulations are compared with experimental data in Sect. 4.5. Finally, the developed model is used for investigating the morphing capability and tunability of LCE-based elements, and the related results are shown in Sect. 4.5.

4.1 Overview and introductory discussion

Research on liquid crystal polymer networks has been attracting scientists from different disciplines, such as theoretical and experimental physics, organic and physical chemistry, material science, engineering, etc. [98].

The synthesis of LCEs can be obtained by following different techniques, which differ in the way the mesogens (and so the polymer chains) are aligned. Generally speaking, the most recently developed techniques can be grouped into two main categories: (1) mechanical-based- and (2) AM-

based- orientation, though different techniques have been used in the past, such as the orientation driven by strong magnetic fields [99].

In the mechanical orientation, a LCE sample is synthesized in the absence of any external fields (magnetic, etc.) and successively subjected to mechanical stress (typically uniaxial deformation) in order to induce the isotropic-nematic transformation (chains alignment). In fact, several experiments have demonstrated that in a LCE network initially in the isotropic state subjected to a mechanical stress, the mesogens embedded in the polymer network can reorient according to the direction of the deformation, leading to a roughly uniform nematic state. In order to avoid recovering the isotropic state because of the relaxation taking place upon removing the load, the nematic LCE is typically subjected to a second photopolymerization process, [98]. In the mechanical orientation, the degree of alignment achieved (usually quantified by means of the order parameter) is directly related to the magnitude of the applied stretch; the higher the stretch applied during the mechanical orientation, the higher will be the alignment inferred to the nematic mesogens and so the higher will be the actuation of the LCE sample under thermal stimulus, [100].

On the other hand, techniques allow synthesizing LCE materials through the use of AM technologies have been recently proposed, [101]. In this context, the DIW (Direct Ink Writing) operates by depositing filament-by-filament a photosensible LCE ink following different printing paths. After printing, the material is subjected to a photopolymerization reaction by using a UV light, Fig. 4.1(a). In comparison to the above described mechanical alignment, technologies based on AM allow producing LCE elements with a non-uniform nematic director (patterned configuration of the mesogens).

Among the different methods of producing LCE elements, AM technologies are promising candidates for developing innovative functional materials with complex morphing capabilities. The local control of the director alignment, achievable through DIW, has enabled the possibility to program the most disparate shape-morphing of LCE-based actuators, Fig. 4.1(b); through an integrated design based on AM [76, 101], different LCE-based elements were obtained (untethered soft robotic matter). More recently, such a process-response link procedure has been exploited in [102] to demonstrate the possibility of producing innovative LCE actuators by using the so-called parameter-encoded 4D printing. The printing process parameters, such as the speed of filament deposition or the nozzle temperature, were used as design parameters to encode a gradient in the director field at the level of single filament. Molecularly-engineered LCE actuators obtained by assembling different LCE inks characterized by distinct nematic-transition temperatures, have been fabricated in [103].

Recent works have also shown the possibility to obtain a controlled actuation by tuning the cross-link density of the polymer network [77, 104], see Sect. 4.3.1 for further details.

All the different existing technologies share the common feature to encode, though in different ways, a desired microstructure in the polymer network. Despite the increasing capacity in fabricating LCEs and in exploiting their actuation capabilities, proper simulation tools are still in their infancy.

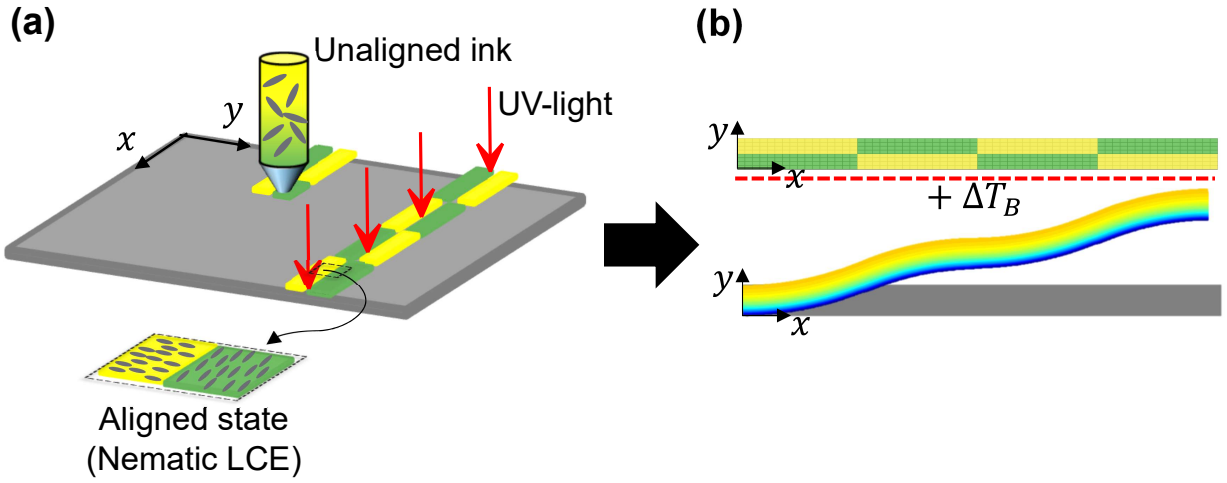

Figure 4.1: *(a) Synthesis process of a LCE element through DIW technique and successive photopolymerization. (b) Corresponding synthesis-process-dependent shape-morphing of a LCE element under thermal stimulus.*

Because of the extreme complexity of the mechanics of LCEs, and because of the very large number of degrees of freedom and variables involved in the functional response of LCE materials, this represents a fundamental challenge to be overcome in order to guide the development and production of advanced devices, through modeling, simulation and design.

A very important concept that must be considered in studying LCEs, is the so called process-microstructure-responsiveness relationship, which is fundamental for modeling, designing, simulating and producing innovative responsive materials. Tuning the fabrication process (synthesis) allows producing different LCE materials characterized by different microstructures, enabling distinct tailored responsiveness. A physics-based model, capable to describe the mechanics of a polymer network, enables us to properly link the microstructure inferred during synthesis, to the desired functional responsiveness.

The first proposed model to describe the theory of liquid crystals, was based on the molecular interactions, [105, 106]. On the other hand, continuum models based on the extension of the Navier-Stokes equations for anisotropic liquids based on the conservation of mass, linear and angular momentum, have been also proposed [107, 108].

When liquid crystals are solidified in a polymer network, the response still exhibits some characters typical of liquids, even if the deformation upon nematic-isotropic transition takes place without material flow. In other words, a LCE material, in addition to its conventional high polymer properties, can display the properties of conventional liquid crystals, except the flow capability [99]. Within this context, the main physics-based theory of LCEs relies on the fundamental development of Warner, Terentjev et al. They extended the rubber elasticity of standard polymers to nematic elastomers by considering the shape anisotropy of the polymer network induced by the LC mesogens, [25, 109–111]. Similarly, other theoretical approaches postulated the existence of different energy

functions linking elastic and nematic deformations [112, 113]. On the other hand, structural models specifically based on the structural element of interest (such as plates, membranes, etc.) made of LCEs have been also proposed [114–116].

4.2 A micromechanical-based model of thermally-responsive liquid crystal elastomers

A LCE network consists of polymer chains joined at discrete points (cross-links) and coupled with mesogens entities integrated in the polymer network. When dealing with LCEs, a fundamental aspect stems from the particular arrangement of the polymer chains forming the network. In the nematic state, mesogens entities are aligned according to a preferential direction which correspondingly induces a preferential orientation also of the polymer chains. Upon thermal stimulus, i.e. by heating above the nematic-isotropic transition temperature, the nematic mesogens reorient passing from an aligned configuration (nematic state) to a random orientation (isotropic state), thus providing a corresponding reorientation of the polymer chains, see Fig. 4.2(a). This reversible transition, occuring at the microscale level, induces a deformation detectable at the macroscale, see Fig. 4.2(b). The mechanical behavior of a LCE network can be quantitatively described by means of a statistical approach. The basic concept of the statistical description of a polymer network has been already described in Chapter 2 for a standard polymer; in this chapter, this concept is extended to develop a micromechanical-based model for describing the process-dependent thermo-mechanical response of LCE materials.

4.2.1 Statistical based description of polymer network: from standard polymers to liquid crystal elastomers

The main physics-based theory of LCEs relies on the fundamental findings and development of Warner, Terentjev et al. They extended the classical rubber elasticity to nematic elastomers by introducing the effect of the molecular anisotropy of the mesogens entities responsible for providing a preferential orientation of the polymer chains, [110, 111, 117].

The approach adopted herein follows the classical rubber elasticity theory of LCEs [109–111, 117]; however, it introduces the description of the LCE network through the distribution tensor [25], a mathematical quantity related to the physical state of a LCE network. As it will be shown, the distribution tensor takes into account: (1) the physical state of the LCE network at the time of cross-linking (usually assumed to coincide with the stress-free state of the network) characterized by the way the LCE material has been synthesized; (2) the change (evolution) of the network conformation upon thermal stimulus. In fact, the reorientation of the mesogen units upon heating, which provides a rearrangement of the polymer chains and in turn shape-morphing of LCE-based elements, can be quantified by the distribution tensor evolution.

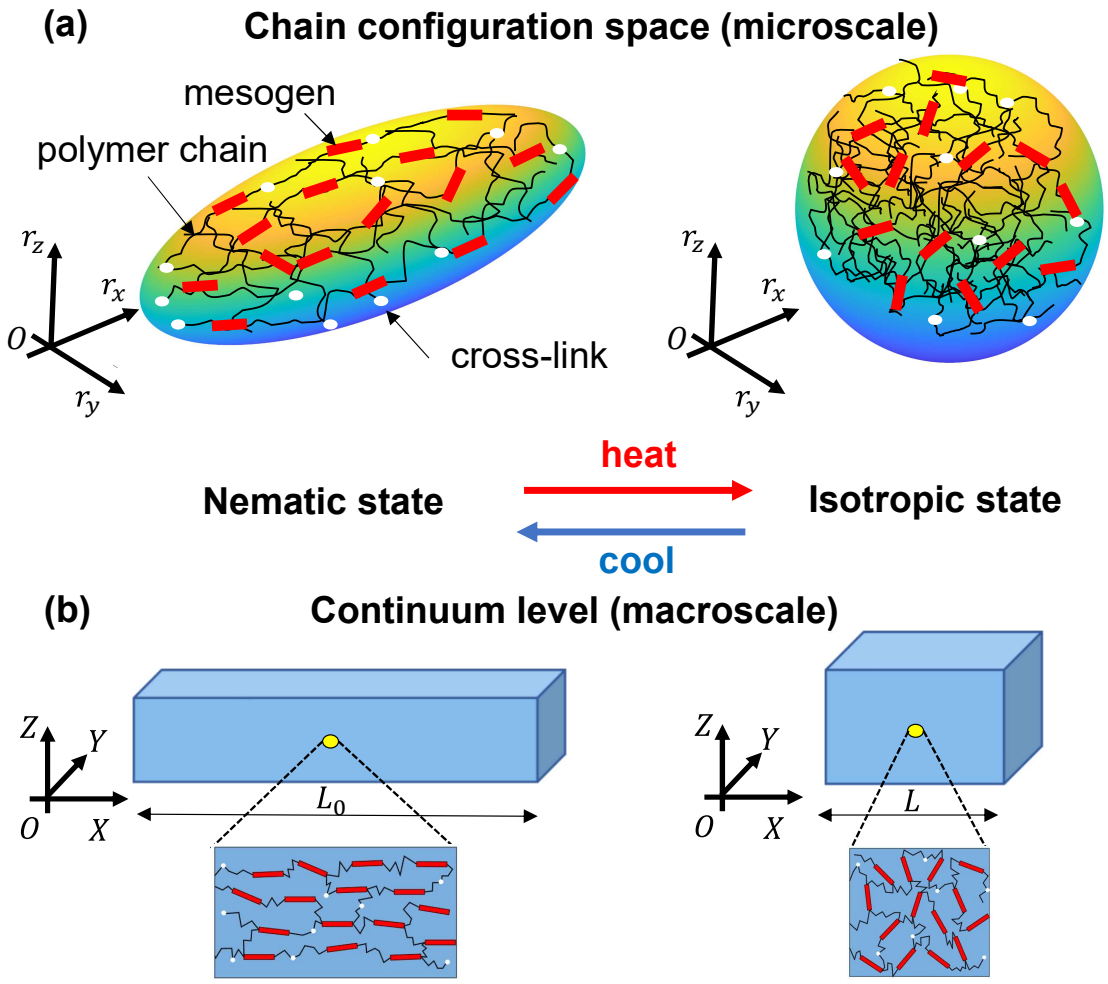

Figure 4.2: *(a) Conformation of a LCE network in the nematic state and in the isotropic one, in the chain configuration space (microscale). (b) Corresponding deformation of a continuum body (macroscale) due to the nematic-isotropic transition of mesogen entities inducing order-disruption of polymer chains and detail of the phenomenon at the microscale.*

In their stress-free state, standard polymers are typically characterized by a uniform distribution of polymer chains orientation. In this case, the distribution tensor $\boldsymbol{\mu}_0$ is characterized by three identical eigenvalues $\mu_{01} = \mu_{02} = \mu_{03}$, (isotropic distribution): this implies a spherical distribution function describing the polymer chains in the chain configuration space. In the nematic state of LCE networks, the polymer chains are arranged according to a preferential direction, resulting in a distribution function whose shape is an ellipsoid with the major semi-axis oriented along the nematic director; similarly to standard polymers, in the isotropic state of LCE networks this ellipsoid becomes a sphere characterized by equal semi-axes whose lengths are proportional to the above mentioned eigenvalues of $\boldsymbol{\mu}_0$.

The nematic director orientation represents an internal degree of freedom which, by interacting with the polymer network, can be modified enabling the material to show spontaneous distortion,

instabilities and deformation, [110, 111, 117]. In particular, in the stress-free state (here assumed to coincide with the nematic state), the statistical distribution function of polymer chains assumes a non-isotropic expression [109]:

$$\varphi_{0n}(\mathbf{r}) = \left[\left(\frac{3}{2\pi N b}\right)^3 \left(\frac{1}{\det \boldsymbol{\ell}_0}\right)\right]^{1/2} \exp\left[-\frac{3\mathbf{r}\cdot\boldsymbol{\ell}_0^{-1}\mathbf{r}}{2Nb}\right] \tag{4.1}$$

As can be noticed, the distribution function φ_{0n} in Eq. 4.1 depends on the so-called initial step-length tensor of the chain distribution, namely $\boldsymbol{\ell}_0 = \ell_{0\perp}\mathbb{1} + (\ell_{0\parallel} - \ell_{0\perp})\mathbf{n}\otimes\mathbf{n}$, [111], where $\ell_{0\perp}$ and $\ell_{0\parallel}$ are the effective initial step lengths measured perpendicular and parallel to the director $\mathbf{n}$, [109, 117]. This quantity gives information on the degree of alignment of polymer chains and so it quantifies the anisotropy of the nematic network just after cross-linking. In a highly ordererd chain network it is $\ell_{0\parallel} >> \ell_{0\perp}$: the higher the alignment degree, the higher the deformation capability obtainable upon stimulus (other parameters being fixed).

The statistical distribution in Eq. 4.1 is conceptually identical to the statistical distribution discussed in chapter 2 for a standard isotropic polymer (Eq. 2.17); in this case, it is written in a general form by generalizing the concept of the average square of the end-to-end vector [109]. In fact, when preferential directions of the polymer chains exist, as occurs in the case of a LCE network, three different average square of the end-to-end vector can be generally defined and their values are related to the step length tensor as $\langle r_i r_j\rangle = \frac{Nb}{3}\ell_{0ij}$, $i = j = 1,2,3$. When the polymer network is in the isotropic state, no preferential directions exist and the step length tensor reduces to $\boldsymbol{\ell}_0 = b\mathbb{1}$ (see below); in this case, the average square of the end-to-end distance does not depend on the considered direction and it can be simply evaluated as $\langle r_i^2\rangle = \frac{Nb^2}{3}$, $i = 1,2,3$ [118].

Similarly to what has been shown in chapter 2, the generalized statistical distribution 4.1 can be related to the chain distribution tensor as: $\boldsymbol{\mu}_n(\mathbf{r}, t=0) = \boldsymbol{\mu}_{0n}(\mathbf{r}) = \langle\varphi_{0n}(\mathbf{r})\mathbf{r}\otimes\mathbf{r}\rangle$, see sect. 2.3.

A fundamental quantity for the mechanical description of LCEs is the so-called order parameter Q. It represents the average degree of alignment of polymer chains provided by the mesogens. It is an average value since nematic mesogens can have locally quite different orientations while, globally, they display a single average orientation. More specifically, by assuming that the nematic mesogens are preferentially aligned with the 3^{rd} coordinate axis (z-axis), the value $Q = 1$ refers to nematic mesogens perfectly aligned with such a direction, while the value $Q = 0$ indicates randomly oriented nematic mesogens. All the degrees of alignment which ranges in between the perfectly nematic phase and the isotropic one are represented by $0 < Q < 1$, with an increase of orientation dispersion as $Q \to 0$. The nematic director $\mathbf{n}$ is a vector whose direction is parallel to the average direction of the nematic mesogens; therefore, being θ the average angle formed by the mesogens axes with the reference direction (here z), the order parameter at the time t is given by $Q(t) = \langle\frac{3}{2}\cos^2\theta(t) - \frac{1}{2}\rangle$, [109]. The degree of alignment of polymer chains in the three directions of the space can be also

conveniently expressed in a tensor form as (order tensor), [99]:

$$\mathbf{Q}(t) = \begin{bmatrix} -Q(t)/2 & 0 & 0 \\ 0 & -Q(t)/2 & 0 \\ 0 & 0 & Q(t) \end{bmatrix} \tag{4.2}$$

where the dependency on the instant time t has been emphasized. At the time of cross-linking, $t = 0$, the polymer network is assumed to be in the nematic state, $Q(t=0) = Q_0$ being Q_0 the initial order parameter. The orientations of the nematic mesogens can be controlled by thermal stimulus, and so $\theta(t) = \theta(T(t))$ and $Q(t) = Q(T(t))$. The nematic-isotropic-transition takes place when crossing the characteristic temperature T_{NI} (see Sect. 4.2.2 for more details).

Importantly, the order tensor is related to the so-called step length tensor and, thus, to the distribution tensor. By following [99], the step length tensor and the order tensor are related by the following relationship:

$$\boldsymbol{\ell}(t) = 2b\left(\mathbf{Q}(t) + \frac{\mathbb{1}}{2}\right) = b\begin{bmatrix} 1-Q(t) & 0 & 0 \\ 0 & 1-Q(t) & 0 \\ 0 & 0 & 1+2Q(t) \end{bmatrix} \tag{4.3}$$

According to Eq. 4.1 and by considering the definition of the chain distribution tensor for standard polymers (sect 2.3), the tensor $\boldsymbol{\mu}_n$ written in its principal directions frame of reference (here assumed to be aligned with the Cartesian framework) is related to the step length tensor as follows:

$$\boldsymbol{\mu}_n(t) = \frac{Nb}{3}\boldsymbol{\ell}(t) = \frac{Nb^2}{3}(\mathbb{1} + 2\mathbf{Q}) = \frac{Nb}{3}b\begin{bmatrix} 1-Q(t) & 0 & 0 \\ 0 & 1-Q(t) & 0 \\ 0 & 0 & 1+2Q(t) \end{bmatrix} \tag{4.4}$$

At the time of cross-linking, the initial chain distribution tensor is related to the initial step-length tensor as (Eq. 4.4):

$$\boldsymbol{\mu}_{0n} = \boldsymbol{\mu}_n(t=0) = \frac{Nb}{3}\boldsymbol{\ell}(t=0) = \frac{Nb}{3}\boldsymbol{\ell}_0 = \frac{Nb}{3}b\begin{bmatrix} 1-Q_0 & 0 & 0 \\ 0 & 1-Q_0 & 0 \\ 0 & 0 & 1+2Q_0 \end{bmatrix} \tag{4.5}$$

If the principal directions of the distribution tensor are aligned with the coordinate axes, the eigenvalues of $\boldsymbol{\mu}_n$ are related to the standard deviation of the chains end-to-end distance components. In fact, when for example the mesogens are aligned with the 3^{rd} space direction, the three eigenvalues of $\boldsymbol{\mu}_n$ are $\mu_{n1} = \langle r_1^2(t)\rangle = \mu_{n2} = \langle r_2^2(t)\rangle \sim 1 - Q(t)$ and $\mu_{n3} = \langle r_3^2(t)\rangle \sim 1 + 2Q(t)$. Therefore, in the principal direction frame of reference, the distribution tensor can be graphically represented by an ellipsoid whose axes are the eigenvalues of $\boldsymbol{\mu}_n$. In the nematic state this ellipsoid is elongated along the nematic director (with major semi-axis length $\sim 1 + 2Q_0$). In the isotropic state (i.e. $Q \to 0$) the standard deviation of the end-to-end distance components recovers those of standard polymers.

The chain distribution tensor evolves in time because of two main contributions. The first stems from a purely mechanical deformation, the second one is related to the spontaneous deformation

induced by the nematic-isotropic transition. In order to not introduce further dependencies, the contribution related to chains rearrangement because of viscoelasticity is neglected. In Sect. 4.2.2, it is shown how the responsiveness of LCEs can be assessed through the chain distribution tensor.

4.2.2 Mechanics of stimulus-responsive LCE

The evolution of the chain distribution tensor $\boldsymbol{\mu}(t)$ allows us to quantitatively assess the mechanical response of LCEs. As recalled above, the evolution of the chain distribution tensor is governed by two contributions, both responsible for a conformational change of the polymer network. The first contribution to the distribution tensor change is related to the rearrangement of polymer chains provided by mechanical deformation, $\dot{\boldsymbol{\mu}}_F(t)$, whereas the second one affects the evolution of the distribution tensor due to the rearrangement of chains induced by the reorientation of nematic mesogens upon thermal stimulus, $\dot{\boldsymbol{\mu}}_n(t)$. Therefore, the evolution of the chain distribution tensor can be expressed as [25]:

$$\dot{\boldsymbol{\mu}}(t) = \dot{\boldsymbol{\mu}}_F(t) + \dot{\boldsymbol{\mu}}_n(t) \tag{4.6}$$

In the proposed model, these two terms are evaluated by means of the following expressions:

$$\dot{\boldsymbol{\mu}}_F(t) = \left.\frac{\partial \boldsymbol{\mu}(t)}{\partial t}\right|_n = \langle \varphi_n(t)\mathbf{r}\otimes\mathbf{r}\rangle \mathbf{L}(t) = \mathbf{L}(t)\boldsymbol{\mu}(t) + \left[\mathbf{L}(t)\boldsymbol{\mu}(t)\right]^T \tag{4.7}$$

$$\dot{\boldsymbol{\mu}}_n(t) = \left.\frac{\partial \boldsymbol{\mu}(t)}{\partial t}\right|_F = 2\frac{Nb^2}{3}\left[\dot{\mathbf{Q}}(t) - \mathbf{W}(t)\mathbf{Q}(t) + \mathbf{Q}(t)\mathbf{W}(t)\right] \tag{4.8}$$

where $\blacksquare|_n$, $\blacksquare|_F$ indicate the evaluation of the quantity $\blacksquare$ at constant nematic order parameter and at constant deformation, respectively. The term $\mathbf{W}$ in Eq. 4.8 is the so-called spin tensor; it is defined as $\mathbf{W} = 1/2(\nabla\dot{\mathbf{u}} - \nabla\dot{\mathbf{u}}^T)$ being $\mathbf{u}$ the displacements vector, [119], and is required, similarly to the rate in Eq. 4.7, to make the rate (Eq. 4.8) objective. In fact, looking at the nematic-isotropic counterpart of the time rate of the chain distribution tensor, $\dot{\boldsymbol{\mu}}_n(t)$, a rotation of the mesogens upon thermal stimulus occurs and thus requires the frame-indifference to be correctly evaluated. From this perspective, the nematic time rate of the chain distribution tensor represents the Jaumann-Zaremba rate [8] of the order tensor $\mathbf{Q}$.

By assuming that the above time derivatives are independent each other, the temporal evolution of the chain distribution tensor can be immediately evaluated by integration over the time domain $0-t$:

$$\boldsymbol{\mu}(t) = \boldsymbol{\mu}_n(t=0) + \int_0^t \left[\dot{\boldsymbol{\mu}}_F(\tau) + \dot{\boldsymbol{\mu}}_n(\tau)\right] d\tau \tag{4.9}$$

being $\boldsymbol{\mu}(t=0) = \boldsymbol{\mu}_n(t=0) = \boldsymbol{\mu}_{0n}$ the initial chain distribution tensor in the stress-free nematic state existing at the time of the synthesis of the polymer network. The distribution tensor at the time t can be used, as described in Chapter 2, for evaluating the stress state of the material:

$$\boldsymbol{\sigma}(t) = \frac{3c_a k_B T}{Nb^2}\left(\boldsymbol{\mu}(t) - \boldsymbol{\mu}_{0n}\right) + \pi(t)\mathbb{1} \tag{4.10}$$

where the hydrostatic pressure $\pi(t)$ ensuring incompressibility of the material can be determined from the boundary conditions.

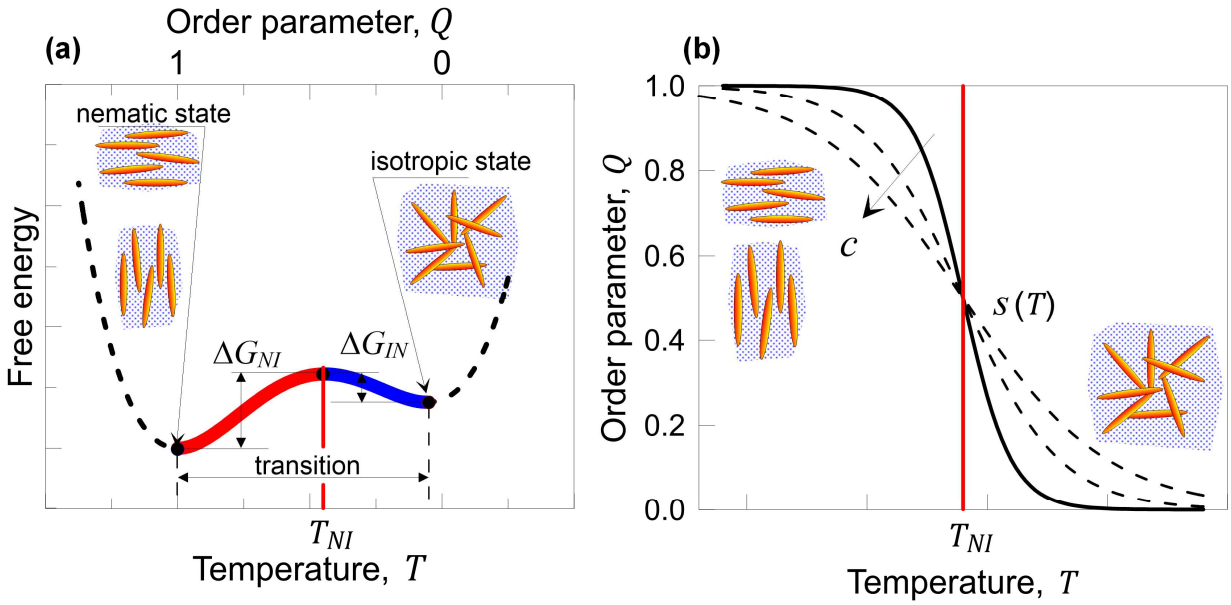

Figure 4.3: *Scheme of the nematic-isotropic transition of a LCE material; (a) energy barrier that must be overcome for passing from the nematic state ($Q = 1$) to the isotropic one ($Q = 0$) upon crossing the T_{NI} and (b) corresponding sigmoid function describing the evolution of the order parameter value.*

Now, let's introduce a simple mathematical model for the nematic-isotropic transition suitable to evaluate $\dot{\boldsymbol{\mu}}_n$ which, in the absence of mechanical deformation ($\dot{\boldsymbol{\mu}}_F = 0$), is the only responsible of the chain distribution tensor evolution.

Similarly to other phenomena involving active molecules or moieties embedded in polymer network undergoing physical or chemical transition between two states upon external stimuli [14, 120], the transition between the nematic state and the isotropic one can be assumed to occur when a sufficient amount of energy is provided to the system. Therefore, when a LCE is exposed to thermal or light sources possessing a sufficient intensity, it looses its initial nematic character and attain the isotropic state. By denoting with ΔG_{NI} the energy barrier that must be overcome in order the nematic-isotropic transition to occur (forward process) and with ΔG_{IN} the energy barrier for the reverse transition (backward process), (Fig. 4.3), a simple mathematical law can be defined. In particular, a sigmoid function (logistic function) is introduced for modeling the aformentioned nematic-isotropic transition. It is expressed as $s(T) = Q(T) = \frac{Q_0}{1+\exp\frac{T-T_{NI}}{c}}$ where Q_0 is the initial order parameter, c is a material-dependent parameter regulating the steepness of the transition, while T_{NI} is the nematic-isotropic transition temperature, (Fig. 4.3(b)), [25]. As can be noticed, the energy barriers (ΔG_{NI} and ΔG_{IN}) have been implicitly used in the definition of the sigmoid function through the transition temperature, while an Arrhenius-type equation [86, 120] requiring the explicit knowledge of the energetic barriers is usually adopted in kinetics chemistry. On the other hand, the terms involved in the proposed sigmoid function are all physics-based and can be simply

measured. For instance, the order parameter of a nematic polymer network can be experimentally measured by means of X-ray measurements to get information on the mesogen alignment. Recently, innovative experimental methods based on polarized and fluorescence optical microscopy [121] have been introduced to quantitatively assess the local order parameter.

According to modern classifications of phase transitions, two types of phase transitions can be defined: first-order and second-order. They are characterized by different relationship between the free energy and thermodynamic variables. First-order phase transitions are those displaying a discontinuity of the free energy with respect to a certain thermodynamic variable (such as the temperature) upon the equilibrium transition point. Examples of first-order phase transitions are those related to the different physical state of matter (liquid, solid, gas). Second-order phase transitions do not display discontinuity of the free energy; typical examples of second-order phase transitions are those associated with magnetic phenomena.

In conventional liquid crystals, the nematic-isotropic transition is strictly first-order, with a discontinuity of the order parameter Q at the thermodynamically equilibrium transition point, [121, 122]. In LCEs, the nematic-isotropic transition has been typically defined to be weakly first order [109] and several experiments have shown a smooth, continuous transition of the order parameter as a function of temperature [121], though the sharpness or the smoothness of such a transition can depend on the specific LCE material properties.

Modeling the nematic-isotropic transition by adopting a continuous sigmoid function, whose steepness can be regulated by acting on the parameter c, is related to the nature of the LCE transition (first order, weakly first order or second order). The sigmoid function time derivative can be evaluated for computing the time rate of the order parameter as $\dot{Q}(t) = \frac{\partial s}{\partial T}\frac{\partial T}{\partial t} = -\frac{\exp\frac{T-T_{NI}}{c}}{Q_0 c}s^2\dot{T}$. This rate is zero when the order parameter is constant in time, occuring for instance when the temperature is constant ($\dot{T} = 0$) or the actual temperature T is far away from the nematic-transition temperature, [25].

By adopting the affine deformation hypotesis, the conformational change of the polymer network can be immediately upscaled at the continuum level for investigating the morphing of LCE-based elements.

Since functionality in LCE materials stems from the order-disruption of the nematic mesogens, which are responsible for providing conformational change of the polymer network, here modelled through the chain distribution tensor, the proposed approach can be easily extended for any type of stimulus triggering the deformation response of the LCE material in turn.

4.3 Cross-link density actuation dependence of liquid crystal elastomers

In this section, according to what has been shown in experimental findings of literature, the presented model is enriched by introducing the role played by the crosslink density in tuning the

morphing capability of LCE materials.

The tunability of the cross-link density and its distribution within a LCE element can trigger a tailored shape-morphing. This model extension represents an important improvement in the field of the design of innovative functional LCE-based materials.

4.3.1 Effect of the cross-link density on the actuation of LCEs: some experimental evidences

The possibility to realize complex shape morphing of LCE materials by exploiting the cross-link-actuation dependency, is a new challenge recently emerged in the literature.

As it has been shown in [104], by photocrosslinking a LCE element in a non-uniform manner (i.e. in spatially selected regions), complex shape-change of the element can be obtained. Similarly, in [123] complex shape-change has been obtained, based on the concept of creating spatial arrangement of actuation and non-actuation domains, by properly non-uniformly de-crosslinking a LCE element. In [77], the possibility to realize programmable actuation by coupling LCE layer domains whose responsiveness is tuned by different degree of cross-link, has been shown.

LCE samples with varying cross-link densities have been investigated in [124]: the maximum actuation strain was obtained by decreasing the cross-link density of the sample. Similarly, LCE films synthesized by varying the percentage of the cross-linker have been fabricated in [125]: the increase of the cross-linker concentration has shown to provide a decrease of the maximum actuation strain (and an increase of the elastic modulus of the material).

Though different experimental studies can be found in literature, a physics-based understanding of the cross-linked-related mechanical response of LCEs has not been provided yet.

4.3.2 Modeling the cross-link actuation dependence of LCEs materials

The role played by the cross-link density on the self-deformation capabilities of LCEs can depend on many factors, such as the type of nematic mesogens, the chemical structure of the cross-linker, the polymer composition, the order state during cross-linking, the technology used for synthesizing the LCE matrix, etc. [77, 124, 126]. In particular, the cross-link density of the LCE matrix affects the intrinsic self-deformation capability of the material (see Fig. 4.4), and of course its stiffness as it is well-known. In addition, it has been experimentally shown that such a feature can also play a role in modifying the nematic-isotropic transition temperature of the material.

In this section, a physics-based model suitable to relate the intrinsic self-deformation capability of LCE materials to the cross-link density is proposed [127]. In doing this, two hypotheses are introduced: (1) a constant nematic-transition temperature is assumed. (2) The initial order parameter does not depend on the cross-link density; in other words, the chemical structure of the cross-links (source of anisotropy, [109]) does not affect the degree of alignment of the LC mesogens.

From a physical viewpoint, the cross-link density can be tuned during the synthesis process by regulating the photopolymerization parameters, (typically UV light intensity and/or exposure time,

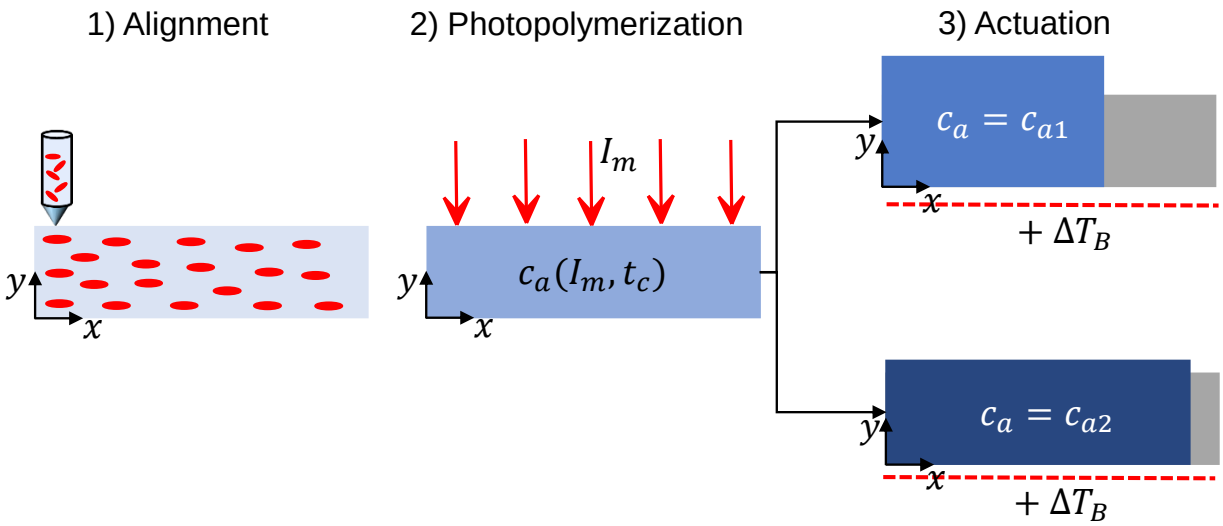

Figure 4.4: *Cross-link density related responsiveness: from the synthesis process to the actuation of LCE materials. The LCE specimens is assumed to be printed with a fixed setup (mesogen alignment, 1); then the material is subjected to the photopolymerization process (characterized by tailored values of the maximum laser light intensity I_m and/or exposure time t_c, 2). This provides a particular cross-link density value which can be tuned through the photopolymerization setup: $c_a = c_{a1}$, $c_a = c_{a2}$, etc. The cross-link density is responsible for the degree of actuation of the LCE material (actuation, 3).*

see Fig. 4.4 and chapter 5) without modifying the composition of the material or, alternatively, by using a fixed photopolymerization setup but tuning the material composition (typically by increasing the concentration of the cross-linker).

Since polymer chains are reciprocally connected, the order variation induced by the thermally-triggered nematic mesogens rotation results in a macroscopic deformation of the material. This response occurs when the cross-link density is low enough to allow the thermal motions of polymer chains upon stimulus, [113]. On the other hand, a too high cross-link density may result in a decrease of the deformation capability, because of the constraint that hinders the thermal motion of polymer chains. Let's consider the actuation of a LCE element undergoing a temperature change crossing the nematic-transition temperature; the amount of deformation is quantified by the measure of its macroscopic self-deformation effectiveness; in the following, this quantity will be indicated through the variable f, with $0 \leq f \leq 1$, where $f = 0$ indicates no actuation while $f = 1$ corresponds to the maximum achievable actuation:

$$f(c_a) = \frac{\varepsilon(c_a)}{\varepsilon(\overline{c}_a)} = \frac{\varepsilon(c_a)}{\varepsilon_{max}} \tag{4.11}$$

where $\varepsilon(c_a)$ is the deformation relevant to the problem in turn for the actual cross-link density c_a, while $\varepsilon(\overline{c}_a) = \varepsilon_{max}$ is the corresponding maximum deformation obtained for the optimal cross-link density $\overline{c}_a$ of the LCE. The scalar function f represents a macroscopic measure of the mesogens effectiveness in inducing the deformation of the LCE network. It can be experimentally determined

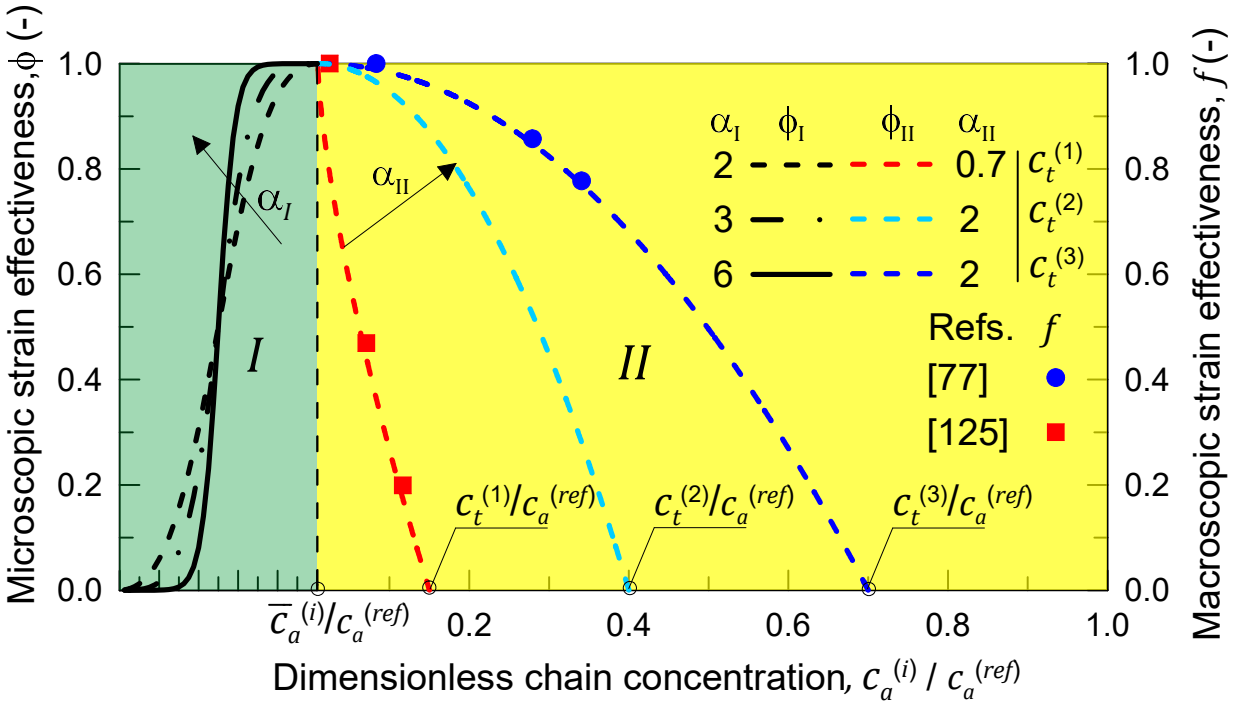

Figure 4.5: *Cross-link density effect on the strain effectiveness of LCEs: macroscopic strain effectiveness vs microscopic strain effectiveness.*

by synthesizing several LCE samples by varying their cross-link density and by measuring the actuation obtained upon the application of the proper stimulus; data from the literature have been elaborated by adopting Eq. 4.11 and plotted in Fig. 4.5.

The above defined macroscopic self-deformation effectiveness, has to be scaled down to the microscopic self-deformation effectiveness.

A thermal stimulus can induce the maximum macroscopic deformation for a proper cross-link density [113], here denoted with $\bar{c}_a$ (optimal cross-lik density). It is assumed that the actuation capability of a LCE material increases by increasing the cross-link density from $c_a = 0$ to $c_a = \bar{c}_a$, region I in Fig. 4.5. On the other hand, the cross-link density value for which no actuation takes place because of the too strong constraint between the chains, is here indicated as $c_a = c_t$. The actuation capability of the LCE is assumed to decrease from the maximum value taking place at $c_a = \bar{c}_a$ up to zero for $c_a = c_t$, region II in Fig. 4.5.

In order to model the above-described actuation capability of LCEs, the microscopic self-deformation effectiveness ϕ is introduced [127]:

$$\phi_I(c_a) = \frac{1}{1 + \left(\frac{\bar{c}_a - c_a}{c_a}\right)^{\alpha_I}} \tag{4.12}$$

$$\phi_{II}(c_a) = 1 - \left(\frac{c_a - \bar{c}_a}{c_t - \bar{c}_a}\right)^{\alpha_{II}} \tag{4.13}$$

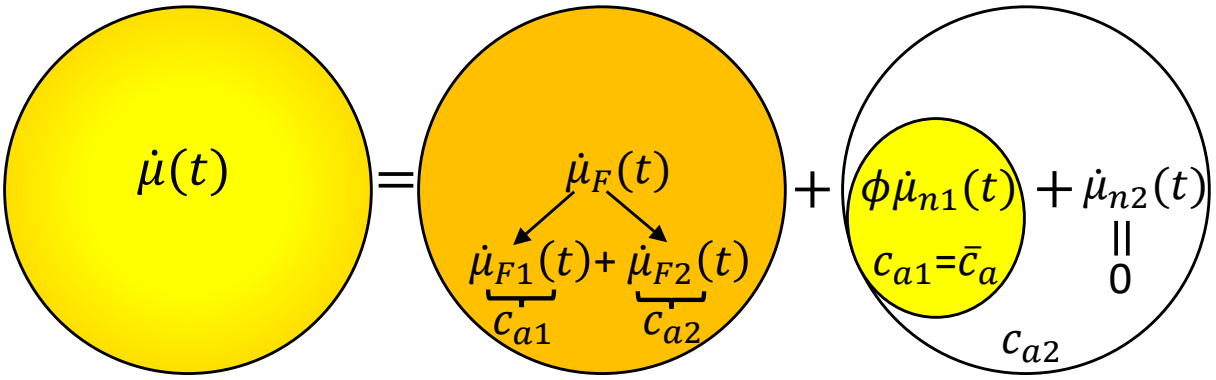

Figure 4.6: *Scheme of the dual network assumption for the evaluation of the chain distribution tensor evolution, in modeling the LCEs cross-link density related self-deformation capability.*

where α_I and α_{II} are material's dependent parameters referred to region I and region II, respectively, Fig. 4.5. Since according to experimental evidences the self-deformation capability of a LCE material can either increase or decrease by changing its cross-link density, it is worth mentioning that two expressions describing the microscopic self-deformation effectiveness have been introduced. Eq. 4.12 quantifies the microscopic self-deformation effectiveness which increases by increasing the cross-link density; it has to be used when the actual cross-link density is lower than $\bar{c}_a$. On the other hand, in the second expression (Eq. 4.13), the microscopic self-deformation effectiveness decreases by increasing the cross-link density, and has to be used when $\bar{c}_a \leq c_a \leq c_t$, i.e. when the material cross-link density falls in region II, Fig. 4.5.

By exploiting the affine deformation hypothesis, the macroscopic self-deformation effectiveness f can be assumed to be equal to the microscopic effectiveness ϕ, i.e. $f = \phi$. This relation can be used for estimating the parameters $\bar{c}_a$, c_t and α. In Fig. 4.5 the microscopic self-deformation effectiveness is plotted for different LCE materials ($i = 1,2,3..$) each one characterized by its own optimal ($\bar{c}_a{}^{(i)}$) and maximum ($c_t{}^{(i)}$) cross-link density. For sake of simplicity, in the graphical visualization the same value of the optimal chain concentration has been used for different materials. Data from the literature (macroscopic self-deformation effectiveness) are also reported for comparison in Fig. 4.5. In order to compare data referred to different materials, a reference cross-link density ($c_a{}^{(ref)}$) is adopted for expressing the cross-link density c_a in a dimensionless form.

From a general viewpoint, the mechanics of a polymer network can be extended to consider the case of multiple networks (see appendix). The concept of multiple network is exploited herein to quantify the nematic-isotropic driven deformation of a LCE network whose actuation capability is affected by the cross-link density. According to Eqs. 4.12-4.13, the microscopic self-deformation effectiveness provided by the mesogens entities is maximum when $c_a = \bar{c}_a$; correspondingly, the LCE network can be reasonably assumed to be made of a single network where the mesogens have the maximum effectiveness.

On the other hand, in region I ($0 < c_a < \overline{c}_a$) and region II ($\overline{c}_a < c_a < c_t$), the microscopic self-deformation effectiveness is lower than the maximum one achievable for $c_a = \overline{c}_a$. Therefore, in these cases the LCE network is fictitiously assumed to be made of a double network. The first one, i.e. the effective network, with a cross-link density $c_{a1} = \overline{c}_a$: it is the only responsible for the actuation of the LCE; in order to take into account the influence of the actual cross-link density c_a, its microscopic effectiveness is weighted by the parameter $\phi(c_a)$. The second network constituting the LCE has a cross-link density $c_{a2} = c_a - \overline{c}_a$; this network is assumed to not have self-deformation effectiveness, i.e. it can be seen as a network without mesogens linked to its backbone. Despite this latter network is characterized by a cross-link density which formally restores the actual one of the LCE network, it ideally represents one of the two limits where no actuation takes place (i.e., $c_a = 0$ in region I or $c_a = c_t$ in region II).

In other words, the actual network is made of two sub-networks: the first one produces the maximum achievable actuation but its effectiveness is weighted by the microscopic parameter ϕ, (region I or region II). The second fictitious sub-network has no effect on the self-deformation because of the absence of cross-link sites (region I) or because of too high cross-link density (region II), both conditions implying no self-deformation effectiveness of the actual LCE network.

The splitting of the actual LCE network into two sub-networks can be now used for evaluating the evolution of the chain distribution tensor (Sect. 4.2.2). Eq. 4.6 must be updated accordingly as follows [127]:

$$\dot{\boldsymbol{\mu}}(t) = \dot{\boldsymbol{\mu}}_F(t) + \dot{\boldsymbol{\mu}}_n(c_a, t) \tag{4.14}$$

where the time rate of the chain distribution tensor related to nematic-isotropic transition is now dependent also on the cross-link density c_a. By exploiting the introduced splitting of the actual LCE network, Eq. 4.14 can be rewritten as:

$$\dot{\boldsymbol{\mu}}(t) = \dot{\boldsymbol{\mu}}_{F1}(t) + \dot{\boldsymbol{\mu}}_{F2}(t) + \phi(c_a)\dot{\boldsymbol{\mu}}_{n1}(\overline{c}_a, t) \tag{4.15}$$

having assumed:

$$\dot{\boldsymbol{\mu}}_F(t) = \dot{\boldsymbol{\mu}}_{F1}(t) + \dot{\boldsymbol{\mu}}_{F2}(t) \tag{4.16}$$

$$\dot{\boldsymbol{\mu}}_n(c_a, t) = \phi(c_a)\dot{\boldsymbol{\mu}}_{n1}(\overline{c}_a, t) + \dot{\boldsymbol{\mu}}_{n2}(c_{a2}, t) \tag{4.17}$$

It is worth mentioning that, since the second sub-network does not produce any actuation, it holds $\dot{\boldsymbol{\mu}}_{n2}(c_{a2}, t) = 0$. The concept of splitting the chain distribution tensor is graphically depicted in Fig. 4.6.

The theory presented in Sect. 4.2.2, where the actuation capability was not affected by the cross-link density, can be recovered as a particular case of the theory developed in this subsection (cross-link density dependent actuation capability) by imposing $c_a = \overline{c}_a$.

It is worth mentioning that the split of the actual LCE network into two sub-networks has been introduced only for quantifying the microscopic strain effectiveness in modelling the cross-link density dependent actuation capability of the nematic-isotropic transition in LCEs, defined by the

rate $\dot{\boldsymbol{\mu}}_n(c_a,t)$. The split of the mechanical deformation counterpart of the time rate of the chain distribution tensor, $\dot{\boldsymbol{\mu}}_F$, is actually not required despite formally correct; in this case, the stress state of the material is evaluated similarly to what shown in sect.4.2.2 (Eq. 4.10), by computing $\dot{\boldsymbol{\mu}}_n(c_a,t)$ as illustrated in this subsection and evaluating the current chain distribution tensor similarly to as illustrated in sect.4.2.2.

4.4 Finite element implementation

In order to obtain a suitable formulation of the problem for its finite element implementation, it is useful to introduce its variational formulation. To this aim, let us consider the potential energy functional Π:

$$\begin{aligned}\Pi &= \int_{\mathscr{B}_0} \Psi_e dV + \Psi_{ext} \\ &= \int_{\mathscr{B}_0} \Psi_e(\mathbf{F})\, dV - \int_{\mathscr{B}_0} \mathbf{B}\cdot\mathbf{u}\, dV - \int_{\partial\mathscr{B}_0} \mathbf{t}\cdot\mathbf{u}\, dA = 0\end{aligned} \tag{4.18}$$

where $\mathscr{B}_0$ and $\partial\mathscr{B}_0$ represent the domain of the body and its boundary, respectively, Ψ_e is the internal energy of the system, whereas Ψ_{ext} represents the energy term related to the external mechanical loads, $\mathbf{B}$ and $\mathbf{t}$, i.e. the body forces and the surface tractions, respectively, while $\mathbf{u}$ is the displacement field. The stationary condition of the above potential with respect to the displacement field $\mathbf{u}$, leads to the following variation:

$$\begin{aligned}\delta_{\mathbf{u}}\Pi &= \int_{\mathscr{B}_0} \frac{\partial\Psi}{\partial\nabla\mathbf{u}}\cdot\delta\nabla\mathbf{u}\, dV - \int_{\mathscr{B}_0} \mathbf{B}\cdot\delta\mathbf{u}\, dV - \int_{\partial\mathscr{B}_0} \mathbf{t}\cdot\delta\mathbf{u}\, dA = \\ &= \int_{\mathscr{B}_0} [\nabla\cdot\mathbf{P}-\mathbf{B}]\cdot\delta\mathbf{u}\, dV + \int_{\mathscr{B}_0} [\mathbf{P}\cdot\mathbf{n}-\mathbf{t}]\cdot\delta\mathbf{u}\, dA = 0\end{aligned} \tag{4.19}$$

where $\mathbf{P}$ represents the first Piola-Kirchhoff stress tensor and $\mathbf{n}$ (not to be confused with the nematic director) is the outward unit vector normal to the boundary $\partial\mathscr{B}_0$. By expressing the stationary condition in residual form, and introducing a discretization of the problem, for a single finite element with volume V_0^e and surface A_0^e (reference configuration) whose shape function matrix and the standard compatibility matrix are $[N]$ and $[B]$, respectively, Eq. 4.19 in matrix notation becomes:

$$\begin{aligned}\{R\}^e_{\mathbf{u}} &= \{R\}^{e,int}_{\mathbf{u}} - \{R\}^{e,ext}_{\mathbf{u}} \\ &= \int_{V_0^e} [B]^T\mathbf{P}\, dV - \left(\int_{V_0^e} [N]^T\mathbf{B}\, dV + \int_{V_0^e} [N]^T\mathbf{t}\, dA\right) = \{0\}\end{aligned} \tag{4.20}$$

which represents a force balance condition [25]. Upon linearization, Eq. 4.20 is expressed as:

$$[K]^e_T\,\Delta\mathbf{u}^e = -\{R\}^e_{\mathbf{u}} \tag{4.21}$$

where $\mathbf{K}^e_T = \dfrac{\partial\mathbf{R}^e_{\mathbf{u}}}{\partial\mathbf{u}} = \displaystyle\int_{V_0^e} [B]^T \frac{\partial^2\Psi}{\partial\mathbf{E}^2}[B]\, dV$ represents the standard tangent stiffness matrix of the finite element e, $\mathbf{E}$ is the Green-Lagrange deformation tensor. Upon assembly, Eq. 4.21 becomes:

$$\mathbf{K}_T\Delta\mathbf{u} = -\mathbf{R}_{\mathbf{u}} \tag{4.22}$$

where $\mathbf{K}_T = \mathbb{A}_{e=1}^{ne} \mathbf{K}_T^e$, with $\mathbb{A}$ the assembly operator and ne is the number of finite elements in which the entire domain has been discretized.

It is worth mentioning that the problem is solved according to the so-called total Lagrangian formulation, according to which all the above equations, as well as stresses and strains, have been written with respect to the initial undeformed configuration $\mathscr{B}_0$. Of course, all the involved quantities are evaluated by accounting for the effect of finite strains taking place in the problem under study. Alternatively, the so-called updated Lagrangian approach, in which the integrals and all the involved quantities are evaluated with respect to the current deformed configuration $\mathscr{B}$, can be also used.

In the reference configuration, corresponding to that at the time of cross-linking, the nematic LCE material is assumed to be in the stress-free state. It is assumed the presence of the thermal stimulus only, without external loads. The temperature field is evaluated by solving the standard heat conduction Fourier equation with the proper boundary conditions. The evolution of the chain distribution tensor allows evaluating the stress state of the material (see Eq. 4.10). Starting from the initial chain distribution tensor $\boldsymbol{\mu}_{0n}$ in the reference configuration, its evolution is evaluated according to Eqs. 4.7-4.8, when the cross-link density effect is neglected, or by using Eq. 4.15 when such an effect has to be considered. The current chain distribution can be thus evaluated by adopting Eq. 4.9 using the corresponding rate evolution terms.

4.5 Numerical examples and model validation

In the perspective of controlling and programming the shape-morphing of LCE-based elements through their synthesis process, several examples are considered in this section. In particular, the first part is focused on the validation of the model, Sect. 4.5.1. The second part of this section is devoted to a deep investigation of the controlled morphing of LCE-based elements: in 4.5.2 architected-LCE-based-elements are investigated while sect. 4.5.3 presents different morphing capabilities of LCE-based elements obtained by exploiting the cross-link-actuation-dependence.

4.5.1 Numerical examples and validation with experimental results

4.5.1.1 Contraction of a simple LCE strip with unialigned mesogens

In this subsection, the simple contraction of a rectangular strip made of polysiloxane monodomain nematic elastomer is investigated [128].

The LCE strip has initial length L_0, whit nematic director oriented parallel to the y-axis. For investigating the effect of the material dependent parameter c, three different values are considered, namely $c = 6; 10; 16$. In the experimental test a LCE specimen, initially in the isotropic state, is cooled down at room temperature starting from an initial temperature of $120\,^{\circ}C$. Such a thermal stimulus induces the material to expand in the y-direction ($\lambda_y \geq 1$), [128]; according to [128] we assume $T_{NI} = 86\,^{\circ}C$ and $Q_0 = 0.46$. The initial conditions of the experimental test and of the FE

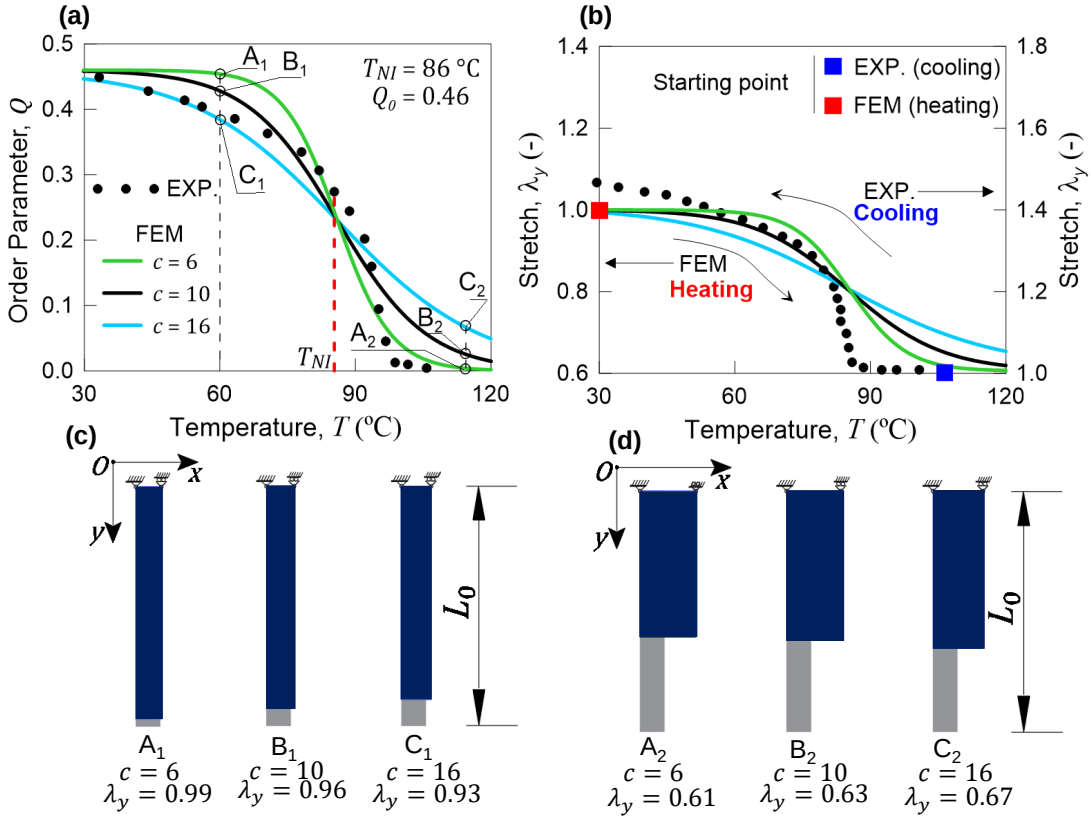

Figure 4.7: *(a,b) $Q-T$ dependence and corresponding $\lambda_y - T$ curve, for different values of the parameter c, obtained by the FE model. The comparison with the $Q-T$ curve and the stretch upon temperature variation, obtained from experimental test of polysiloxane monodomain nematic elastomer [128] is also reported. (c,d) Comparison of the undeformed (grey) and deformed (blue) shapes of the LCE element, obtained from the FE model for different values of the parameter c; in particular, configuration at different temperature values are shown, $T = 60\,°C$ (A_1, B_1, C_1) see sub-figure (c), $T = 110\,°C$ (A_2, B_2, C_2) see sub-figure (d).*

analysis are displayed by the blue and red squares, respectively, see Fig. 4.7(b). Only the absolute value of the stretch difference between different states is meaningful [25]. Overall, the model results are in reasonable agreement with the experimental ones (Fig. 4.7), both in terms of the $Q-T$ transition, (Fig. 4.7(a)), and of the stretch evolution vs thermal stimulus, (Fig. 4.7(b)). The material's dependent parameter c plays a determinant role in tuning the steepness of the $Q-T$ transition, and thus on the stretch-temperature evolution in time. In particular, lower values of c provide a sharp nematic-isotropic transition whereas greater values induce a smooth transition. Although this is not the purpose of the present work, this observation could be exploited for developing and optimizing LCE materials by tuning their responsiveness speed.

The deformed shapes of the LCE element obtained by the FE simulations for different values of c and two values of the temperature, are reported in Fig. 4.7. In particular, Fig. 4.7(c) illustrates the deformed shapes of the element at $T = 60\,°C$ (corresponding to the points A_1, B_1 and C_1 of the

$Q-T$ curves reported in Fig. 4.7(a)). Similarly, Fig. 4.7(d) illustrates the deformed shapes of the LCE element at $T = 110\,^{\circ}C$, (points A_2,B_2 and C_2 of Fig. 4.7(a)). The parameter c plays a role in determining the time evolution of the order parameter, whereas for $T >> T_{NI}$ the stretch does not depend on c but only on the initial order parameter, [25].

4.5.1.2 Investigation of 3D printed LCE actuators

In this subsection numerical and experimental analysis of 3D printed LCEs-based actuators are illustrated. The experimental investigation has been conducted at the Caltech Division of Engineering and Applied Science whereas the LCE material and the 3D printed LCE-actuators were synthesized at the John A. Paulson School of Engineering and Applied Sciences, Harvard University.

3D printed polymeric actuators made of LCE bilayers with orthogonal nematic director alignment interconnecting polymeric tiles, have been prepared [76]. The scheme of the element is presented in Fig. 4.8. The particular arrangement of the nematic mesogens across the bilayer forms an active hinge which induces bending of the actuator upon heating, see Fig. 4.8(a). In fact, each layer exhibits a contraction along the printing direction (parallel to the nematic mesogens) and an expansion in the orthogonal directions; the resulting strain mismatch across the thickness of the LCE bilayer induces a bending response. In the experimental measurements, rotation angles of the LCE actuators were measured through subsequent images of the bending process. In order to investigate the possibility to tune the bending responsiveness of the fabricated actuators, specimens were fabricated by varying the geometrical parameters of the LCE bilayer hinges as well as by using different oligomeric LCE inks to obtain different nematic-isotropic transition temperatures. In particular, two types of specimens denoted with LT_{NI} and HT_{NI}, respectively, were prepared; LT_{NI} specimens start display bending near $25\,^{\circ}C$ and become fully isotropic at $92\,^{\circ}C$, while, HT_{NI} specimens start show bending roughly at $60\,^{\circ}C$, and become fully isotropic at $127\,^{\circ}C$. LT_{NI} specimens are made of a bilayer LCE hinge with thickness $h = 0.25\,mm$ and width $w = 1\,mm$, while HT_{NI} specimens are prepared with different hinges having thickness $h = 0.25\,mm$ and widths $w = 1\,mm$ and $w = 2\,mm$, respectively.

In modelling the behavior of LCE hinges, it is assumed $T_{NI} = 50\,^{\circ}C$ and $T_{NI} = 95\,^{\circ}C$ for the LT_{NI} and for the HT_{NI}, respectively. Both these temperatures are about halfway within the range of the experimentally observed actuation. Nematic mesogens are oriented parallel to the z-axis in the bottom part of the element (i.e. for $0 \le y/h \le 0.5$, Fig. 4.8) while the nematic director is assumed to be parallel to the x-axis in the top part of the element (i.e. for $0.5 \le y/h \le 1$). According to the experimental findings, such an orientation will generate a bending response with curvature towards the upper layer. By fitting experimental results, the initial order parameter has been found to be $Q_0 = 0.3$, while the material parameter c has been assumed equal to $c = 10$. Other parameters, such as the mechanical ones, have been determined by means of standard tensile tests led on LCE bilayers and on the acrylate material composing the rigid parts of the actuator, see [76].

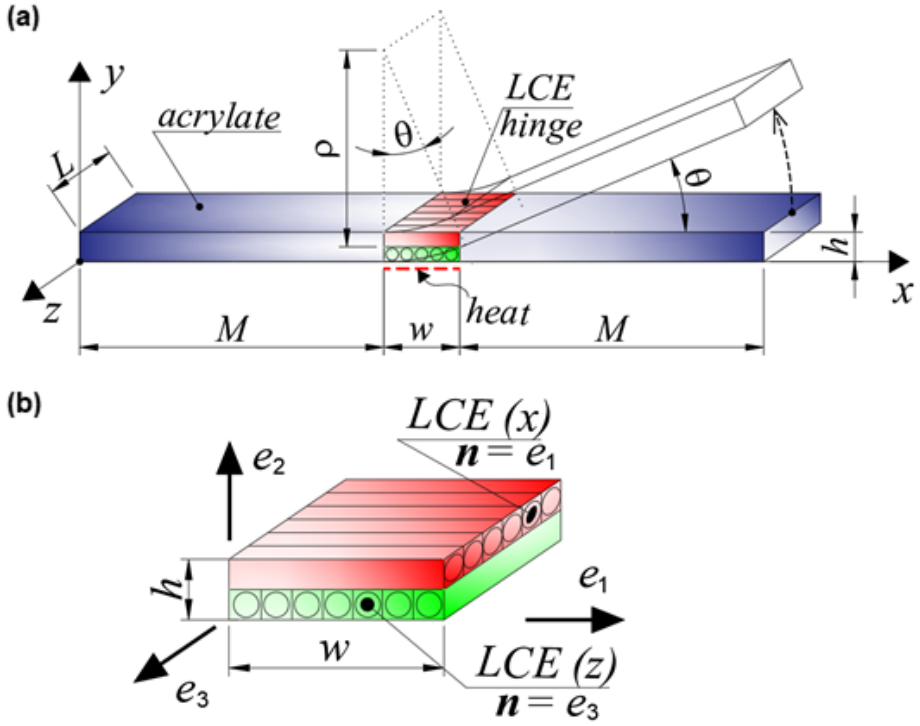

Figure 4.8: *(a) Scheme of the 3D printed LCE-based actuator with indication of the frame of reference used in the modeling and (b) particular of the bilayer LCE hinge of the actuator.*

All the numerical analyses have been performed by assuming a plane stress condition. During the experimental campaign LCE-based specimens were heated in an oil bath, while in the numerical simulations it is assumed to heat the element from the bottom face of the LCE hinge. The temperature evolution within the material is determined by solving the heat conduction problem, adopting a thermal conductivity coefficient $k = 0.2\,W/mK$ and specific heat $C = 1050\,J/kgK$, which are typical values for polymeric materials [129–131]. The thermal expansion of the material is assumed to be negligible within the considered temperature range, and therefore the bending response arises only because of the order-disruption upon nematic-isotropic transition. The bending response of the LCE-based actuators are displayed in Fig. 4.9. In particular, the results for the LT_{NI} specimen having thickness $h = 0.25\,mm$ and width $w = 1\,mm$ and the results of two HT_{NI} specimens of same thickness $h = 0.25\,mm$ and different widths $w = 1\,mm$ and $w = 2\,mm$, are plotted in Fig. 4.9. In the experimental tests of LT_{NI} specimens, the initial angle was negative at room temperature due to the residual stresses induced by 3D printing, Fig. 4.9(a). Therefore, for the sake of comparison with numerical modelling which neglects the residual stresses, the rotation vs temperature obtained from the simulation, has been shifted in order to initially match with the experimental measurements. The rotation angle vs temperature of the LT_{NI} specimen, in which residual stress effects play a role in the measured rotation angle and hinders the comparison with

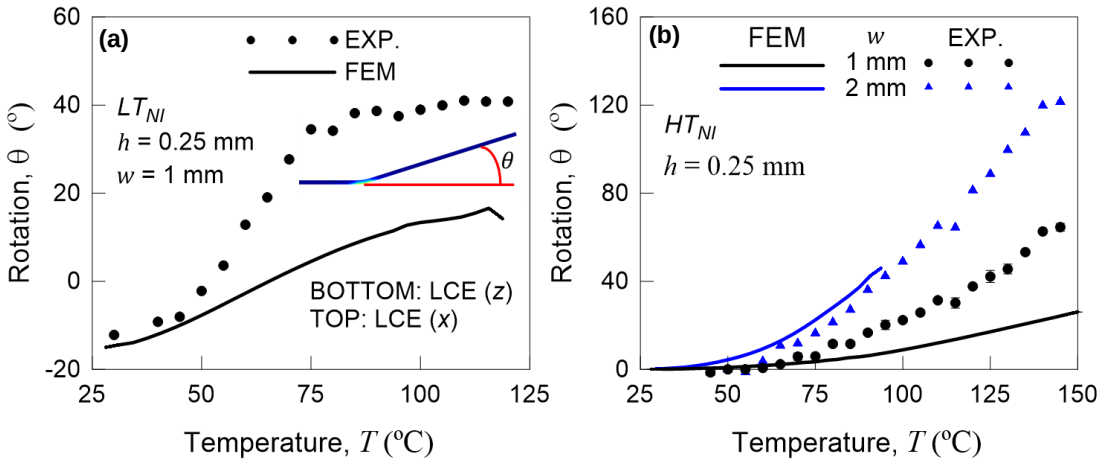

Figure 4.9: *Rotation angle vs temperature for (a) the LT_{NI} specimen with a bilayer LCE hinge having thickness $h = 0.25\,mm$ and width $w = 1\,mm$ and for (b) HT_{NI} specimens fabricated with two different hinges of same thickness $h = 0.25\,mm$ and distinct widths namely $w = 1\,mm$ and $w = 2\,mm$, respectively. For each case, experimental measurements and results obtained by the presented FE model are displayed.*

the model assessment which results to be underestimated, is shown in Fig. 4.9(a). On the other hand, when HT_{NI} specimens are considered, no residual stresses effects have been observed; in this case, the comparison between experimental and numerical results shows a better agreement, see Fig. 4.9(b). The bending responsiveness is more pronounced by increasing the LCE hinge width. The temperature profiles, the order parameter and the strain ε_x along the vertical center line of a LT_{NI} specimen ($h = 0.25\,mm$ and $w = 1\,mm$) provided by the model are plotted in Fig. 4.10. The profiles are plotted for three different values of the T_B/T_{NI} ratio, namely $T_B/T_{NI} = 0.75; 1.25; 1.75$, where T_B is the bottom boundary temperature. Such a temperature ratio quantifies the applied stimulus triggering the order-disruption. As it can be noticed (Fig. 4.10(a)), by increasing the T_B/T_{NI} ratio, the temperature profile moves to the right whereas the corresponding order parameter profiles moves to the left (decrease of Q), Fig. 4.10(b). According to the orientation of the nematic mesogens, the bottom part of the LCE hinge expands while the top part contracts, i.e. the strain mismatch (Fig. 4.10(c)) provides a bending responsiveness of the LCE. When the temperature is well below the T_{NI} (Fig. 4.10(d1)), the order parameter is uniform and tends to its initial value $Q_0 = 0.3$, Fig. 4.10(d2), and the LCE does not display bending. A temperature increase induces a reduction of the order parameter which induces the LCE actuator to bend, Fig. 4.10(e1-e2,f1-f2).

4.5.1.3 Effect of the cross-link density on the contraction of a simple LCE strip

The aim of this subsection is to verify the capability of the developed model, in assessing the morphing tunability of LCE materials by harnessing the role played by the cross-link density.

Three different LCE strips, whose matrix has been prepared by synthesizing the LCE material

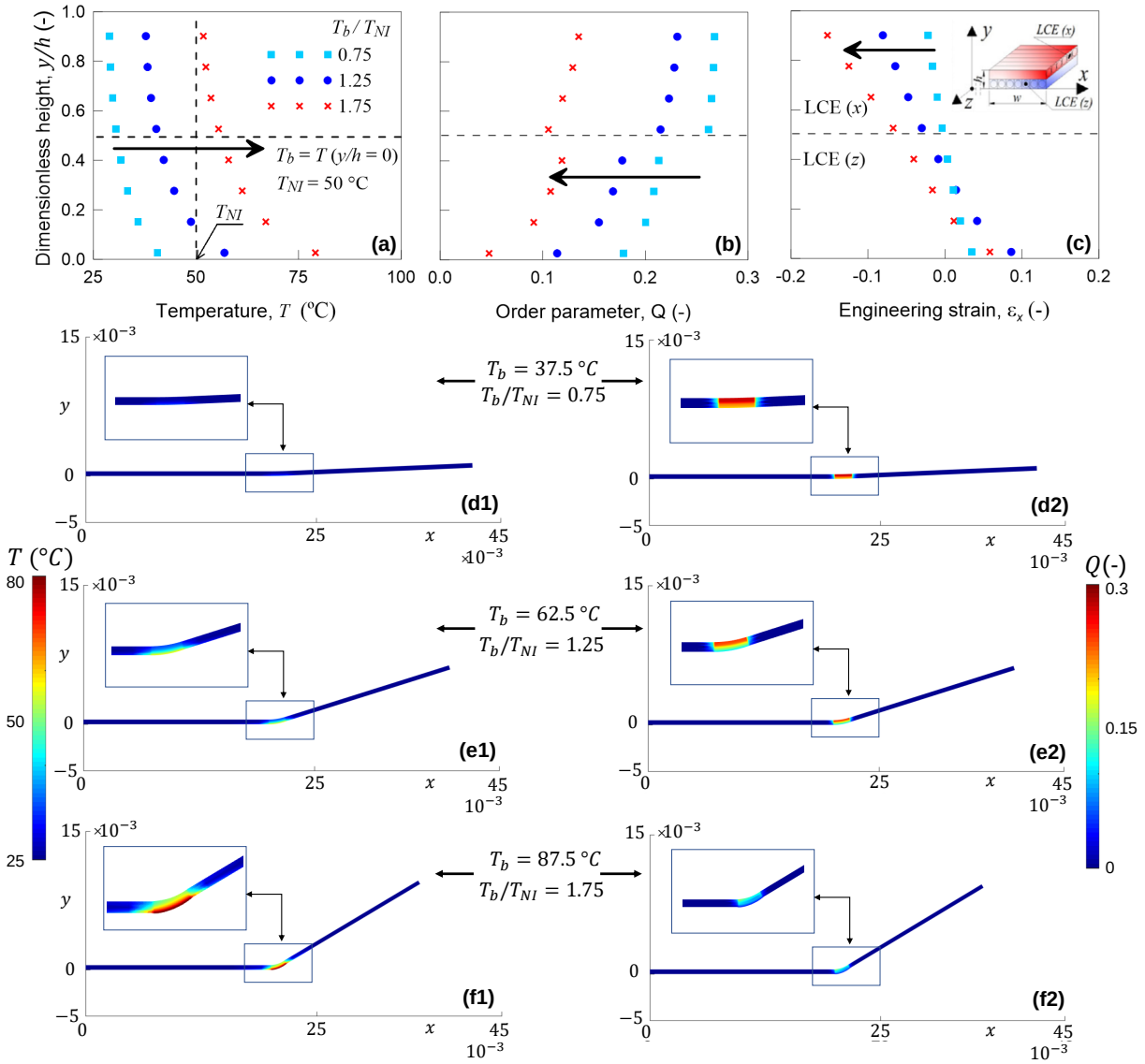

Figure 4.10: *Profiles along the vertical line centered in the LCEs hinge of the LT_{NI} specimen, of the (a) temperature, (b) order parameter and (c) longitudinal strain ε_x, provided by the FE model. Different values of the dimensionless temperature T_B/T_{NI} are considered, namely $T_B/T_{NI} = 0.75; 1.25; 1.75$. For each of the three considered T_B/T_{NI} ratios, the corresponding contour map of the temperature (d1,e1,f1) and of the order parameter (d2,e2,f2) are plotted within the deformed configuration of the LCE actuator.*

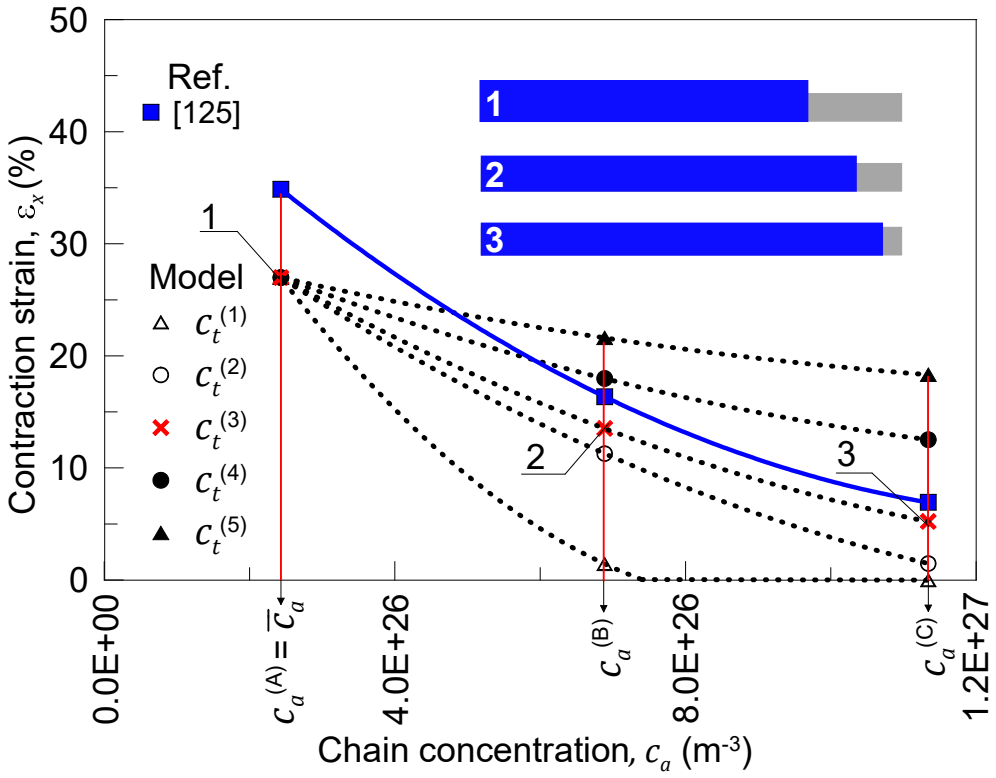

Figure 4.11: *Contraction of a LCE strip vs chain concentration for a fixed optimal cross-link density ($\overline{c}_a$) and different ideal chain concentration hindering the self-deformation effectiveness of mesogens (c_t). Comparison with experimental data adapted from [125] are also reported.*

using a cross-linker in three different percentages, are considered. The elastic properties (Young's Modulus) of the three LCEs are $E^{(A)} = 3\,MPa$, $E^{(B)} = 8.5\,MPa$ and $E^{(C)} = 14.5\,MPa$, corresponding to a cross-linker concentration of $5; 10; 15\%\,mol$, respectively, [125]. The corresponding shear moduli are $\mu^{(A)} = 1\,MPa$, $\mu^{(B)} = 2.83\,MPa$ and $\mu^{(C)} = 4.83\,MPa$, see Fig. 4.11. The nematic mesogens have been assumed to be aligned with the horizontal direction (x-direction), in order to provide contraction of the strip upon heating. The initial order parameter has been assumed to be $Q_0 = 0.5$, while the parameter governing the transition has been assumed to be $c = 8$. As emphasized in [125], a slight dependence of the nematic-isotropic transition temperature on the cross-link density has been found. Since the maximum actuation is herein considered ($T >> T_{NI}$), such a dependence is neglected and the nematic-isotropic transition temperature is assumed to be constant and equal to $T_{NI} = 65\,°C$.

As it can be noticed from the experimental tests in [125], the actuation strain capability decreases by increasing the cross-linker content. Therefore, it is assumed the LCE material to be in region II where the deformation capability decreases by increasing the cross-link density (sect. 4.3.2). Furthermore, the optimal cross-link density $\overline{c}_a$ is evaluated by adopting the optimal shear modulus $\overline{\mu}_a = 1\,MPa$. The parameter α_{II} required for defining the microscopic self-deformation

effectiveness is assumed to be 0.65. Five different values of the cross-link density hindering the self-deformation, namely $c_t^{(1)}$, $c_t^{(2)}$, $c_t^{(3)}$, $c_t^{(4)}$, and $c_t^{(5)}$, are assumed for each of the three investigated LCE materials. The values of the above-mentioned cross-link density have been determined by assuming five different values of the corresponding shear modulus, $\mu_t^{(1)} = 3\,MPa$, $\mu_t^{(2)} = 5\,MPa$, $\mu_t^{(3)} = 6\,MPa$, $\mu_t^{(4)} = 10\,MPa$, and $\mu_t^{(5)} = 20\,MPa$.

The results of the numerical simulations as well as of the experimental results are displayed in Fig. 4.11. As it can be noticed, the maximum cross-link density $c_t^{(3)}$ provides a contraction strain vs chain concentration which better approximates the experimental results. Regardless of the adopted parameters, all the curves present a trend compatible with that observed in experimental tests. It is important to highlight that when c_a is greater than the ideal limit c_t, the self-deformation effectiveness disappears; in this example, this is the case characterized by the smallest c_t, namely $c_t^{(1)}$, Fig. 4.11. When the actual concentration overcomes the value $c_t^{(1)}$ (corresponding to $\mu_t^{(1)} = 3\,MPa$), the actuation vanishes: in fact, by adopting the value $c_a^{(B)}$ (whose cross-link density corresponds to $\mu^{(B)} \sim 2.83\,MPa$), the strain vs cross-link density goes to zero when $\mu^{(B)} < \mu_t^{(1)} \leq \mu$.

4.5.2 Controlled morphing of architected LCEs

In this subsection, the developed model is exploited to perform a computational analysis aimed at controlling and programming the shape-morphing of architected LCE-based elements by encoding different patterns of nematic mesogens (different orientations) and by exploiting different transition temperatures, [132]. The actuation capability of the investigated 2D beam-like LCE-elements is assumed to be independent on the cross-link density. The nematic mesogens orientations, the geometrical size of the constituent blocks and the transition temperature, are made to change.

In the following examples, a 2D beam-like element whose length to thickness ratio is $L/h = 16$, $h = 500\,\mu m$ and $t = h$ is considered (t indicates the out of plane dimension of the element). The shear modulus of the material is $\mu = 13.33\,kPa$, and a plane stress condition is assumed. The element is thermally stimulated by heating up its bottom surface from $T_B = 25\,^\circ C$ to $T_B = 150\,^\circ C$. The thermal conductivity and specific heat are assumed to be $k = 0.2\,W/mk$ and $C = 1050\,J/KgK$, respectively. In order to avoid introducing further dependencies, the thermal expansion of the material is neglected within the temperature range considered. Unless differently explicitly stated, the nematic-isotropic transition temperature is assumed to be $T_{NI} = 50\,^\circ C$ and the parameters governing the transition are $Q_0 = 0.3$ and $c = 20$.

In the first example, the cantilever beam-like element is assumed to be made of a non-actuation domain (standard polymers, blue region Fig. 4.12) and by four bilayer LCE blocks (localized hinges) with nematic mesogens oriented parallel to the horizontal (LC_X blocks, yellow regions of Fig. 4.12) and parallel to the vertical (LC_Y blocks, green regions of Fig. 4.12), [132]. The height of a single layer is assumed to be $h/2$. By changing the position of the localized hinges and/or by switching the orientation of the mesogens within the hinge, LCE-based elements can morph in different ways as illustrated in Fig. 4.12, [132]. In the second example, the element is entirely made of

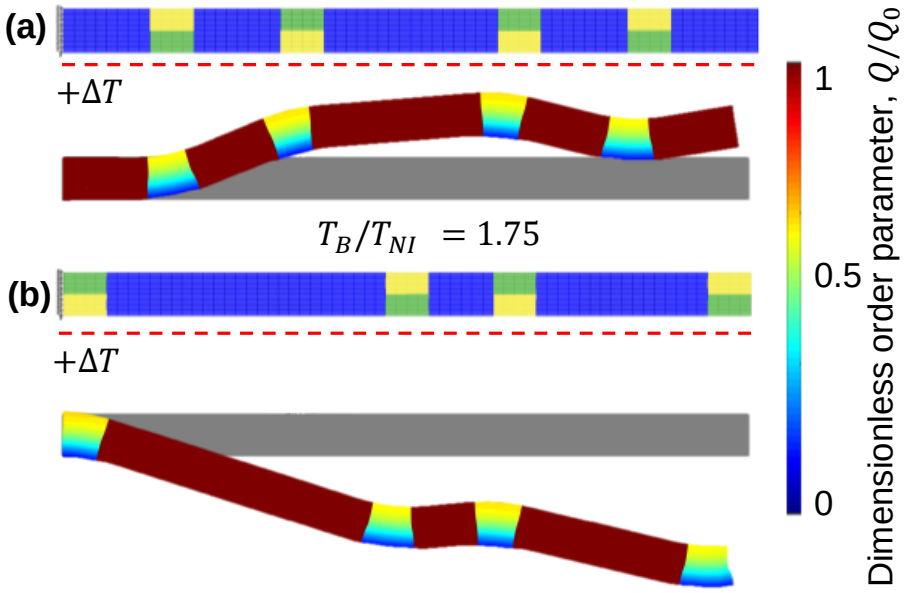

Figure 4.12: *Examples of controlled morphing of LCE-based elements, by changing the position of LCE hinges and/or by switching the orientation of the mesogens within the hinge.*

LCEs blocks opportunely arranged in its backbone. Three beam-like elements made of LCE blocks arranged as shown in Fig. 4.13 are considered; each element is characterized by different widths of the constituent LCE blocks, namely $w/L = 0.125; 0.25; 0.5$, Fig. 4.13(top-to-bottom elements), [132]. In this example the same value of the nematic-isotropic transition temperature is assumed for all the LCEs blocks constituting the element, whereas the case of LCE-based elements with the transition temperature varying from block to block will be also considered in the following. The shape-morphing capability of the elements reported in Fig. 4.13 is studied by adopting either a cantilever boundary condition (BC) along the edge ① (displacements $\delta_x = \delta_y = 0$ at $X = 0$) or by assuming the element lying on a rigid horizontal frictionless plane (unilateral constraint, displacements $\delta_y \geq 0$ at $Y = 0$), see Fig. 4.13. The results obtained are reported in Fig. 4.14; in particular, for each architected beam-like element in Fig. 4.13, the deformed shapes of the middle line of the element at three different temperatures, namely $T_B/T_{NI} = 0.7; 1; 1.5$, are illustrated in Fig. 4.14(a,c,e). Moreover, Fig. 4.14(b,d,f) shows the corresponding contour of the temperature fields as well as of the order parameter at $T_B/T_{NI} = 1$ plotted in the deformed configuration. As can be noticed from Fig. 4.14, the deformed shapes of the element can be controlled by regulating the pattern and the width of the constitutive LCE blocks. From a functional perspective, it can be noticed that the designed elements can assume different wavy-like shapes depending on the pattern of the LCE blocks and on the thermal stimulus provided. Analogously, the deformation responsiveness of the architected LCE beam-like elements on an horizontal rigid and frictionless plane, is displayed in Fig. 4.15. As occurs in the case of cantilever LCE elements, the higher the widths of the LCE blocks the higher the amplification of the resulting deformed shape. Furthermore, due to the

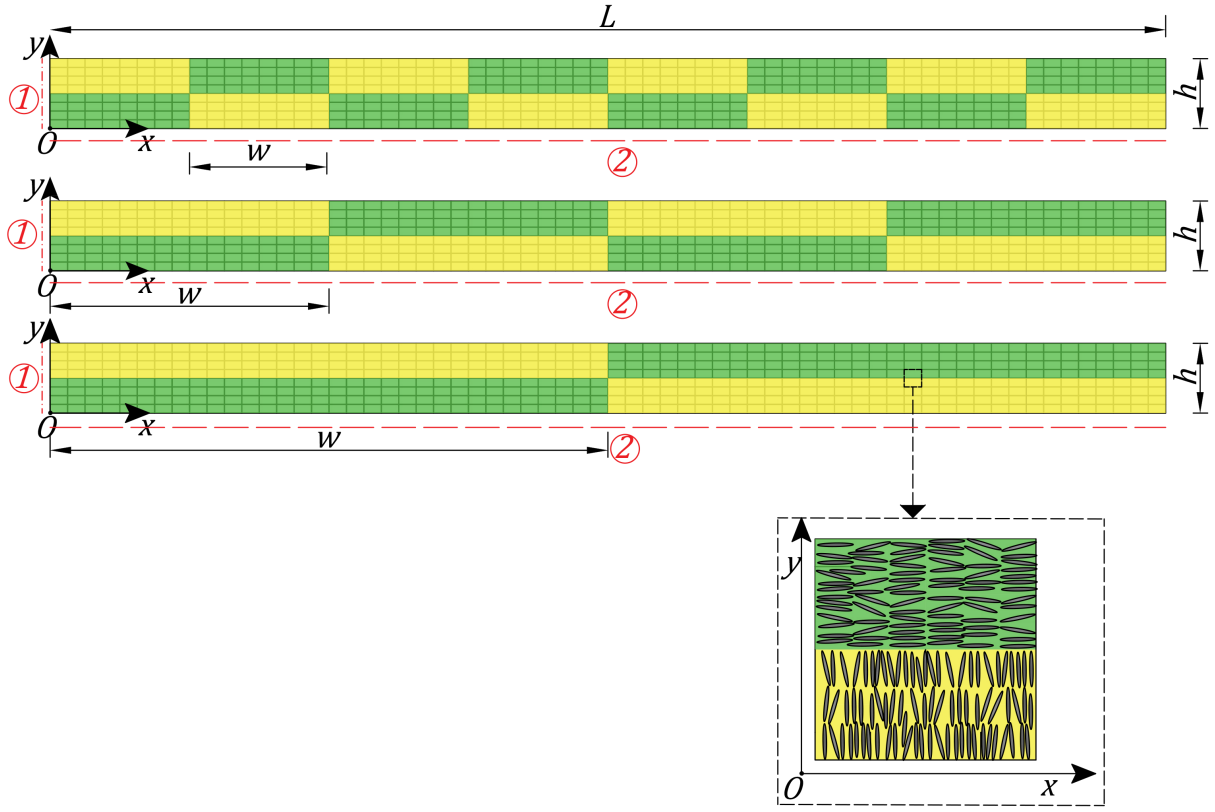

Figure 4.13: *Configuration of different patterns of LCEs blocks within the considered beam-like element (architected LCE-based elements), with three different widths of the constituent LCEs blocks corresponding to three dimensionless ratios* $w/L = 0.125; 0.25; 0.5$ *(top-to-bottom elements). Each element is heated at its bottom part; moreover, for each element, two analysis are performed by varying the boundary conditions: clamped boundary condition,*①*, and vertical support on a rigid, horizontal and frictionless plane, (unilateral support)* ②*.*

different boundary conditions, the amplitude of the deformed shapes are less pronounced for fixed values of w/L and T_B/T_{NI}. The last numerical example, aims at demonstrating the possibility to design a displacement path, reaching a specific target zone at the end of the thermo-mechanical morphing: from this perspective in specific applications it can be required the structural element to be deformed in a specific way at the end of the actuation, following a defined kinematics path. To this aim, LCE blocks are assumed to have distinct transition temperatures. Four cases are considered; the transition temperatures of the mesogens preferentially oriented along the x-axis is fixed at $T_{NI,X} = 50\,°C$ whereas for the mesogens preferentially oriented along the y-axis the following values are assumed: $T_{NI,Y} = 50; 70; 100; 130\,°C$ (cases $1, 2, 3, 4$ respectively, Fig. 4.16). This architecture induces a controlled shape-morphing; as it can be noticed from Fig. 4.16(a), the point P moves from its initial position (P_0 at $X = L, Y = 0$) by following distinct paths to achieve a certain target zone (light blue circle of Fig. 4.16(a)). Fig. 4.16(b) illustrates the deformed shapes of the middle line of the LCE element at $T_B = 70°$; the exploitation of LCE blocks having distinct transition

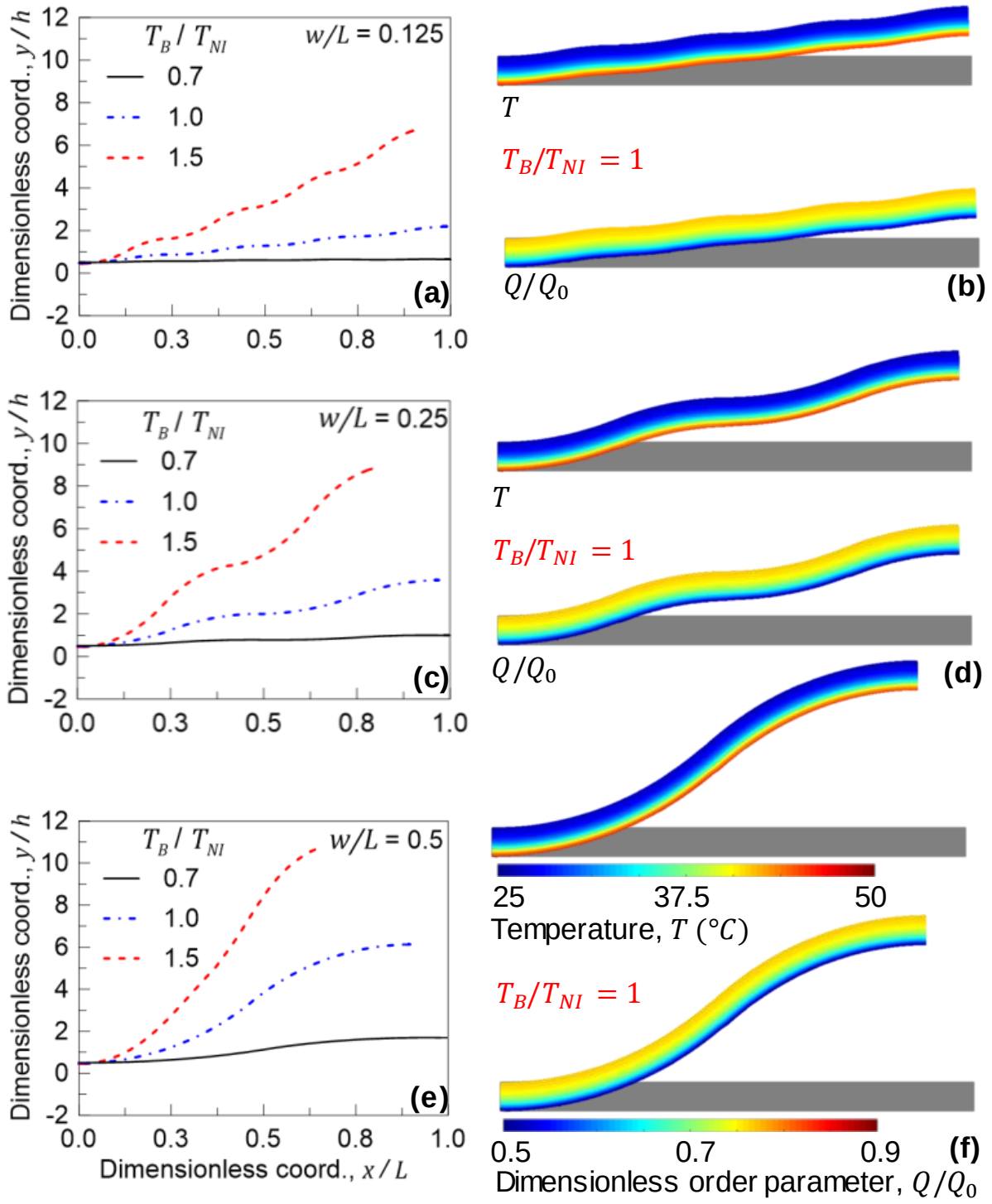

Figure 4.14: *Morphing of architected LCE cantilever elements in Fig. 4.13: (a,c,e) deformed shapes of the middle line of the element for different values of the applied boundary temperature for the three configurations of the architected LCE elements, and (b,d,f) corresponding contours of the temperature field and of the dimensionless order parameter plotted in the deformed configuration at* $T_B/T_{NI} = 1$.

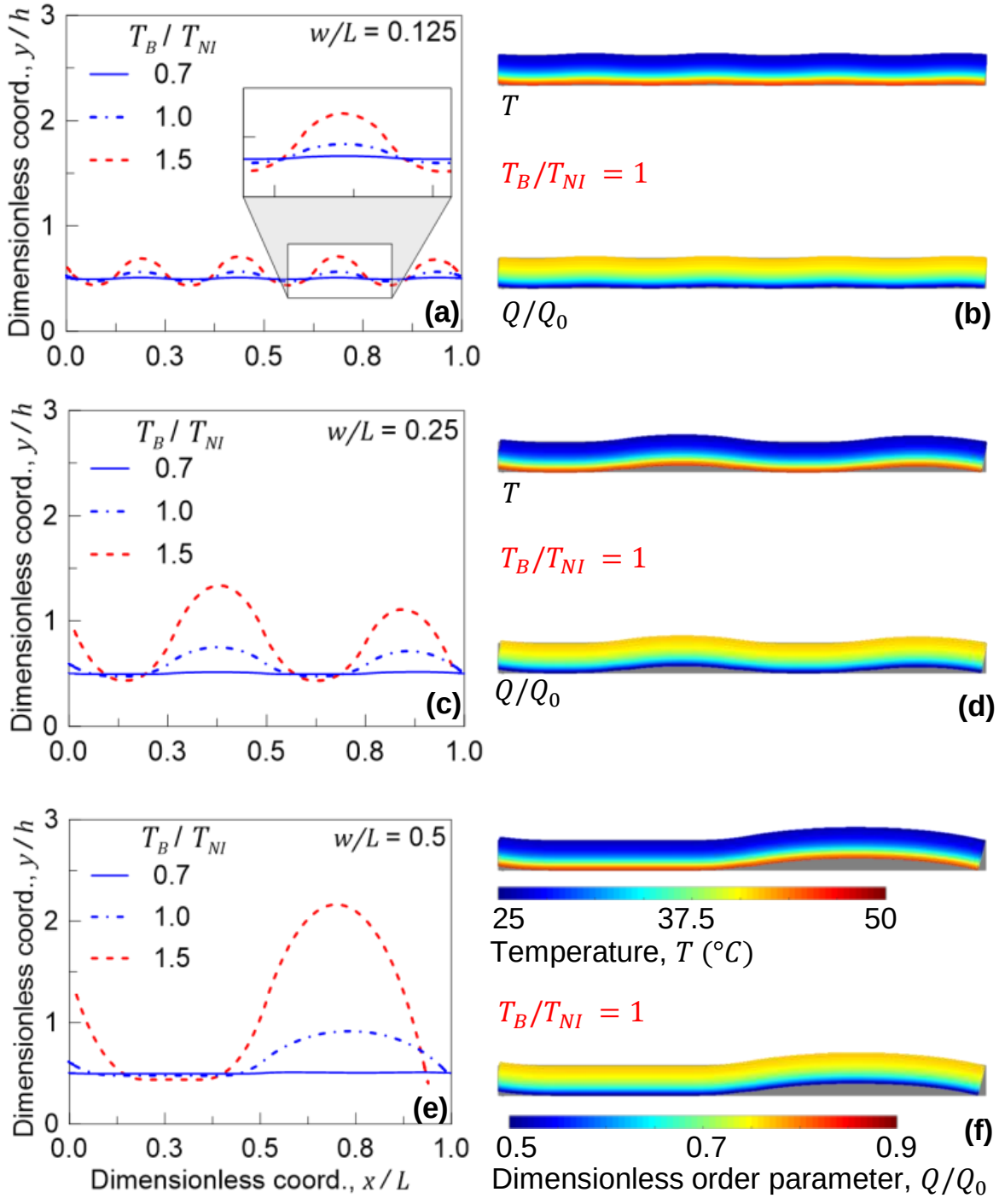

Figure 4.15: *Morphing of architected LCE elements in Fig. 4.13 restrained on a unilateral support: (a,c,e) deformed shapes of the middle line of the element for different values of the applied boundary temperature for the three architected configurations, and (b,d,f) corresponding maps of the temperature field and of the dimensionless order parameter plotted in the deformed configuration at* $T_B/T_{NI} = 1$.

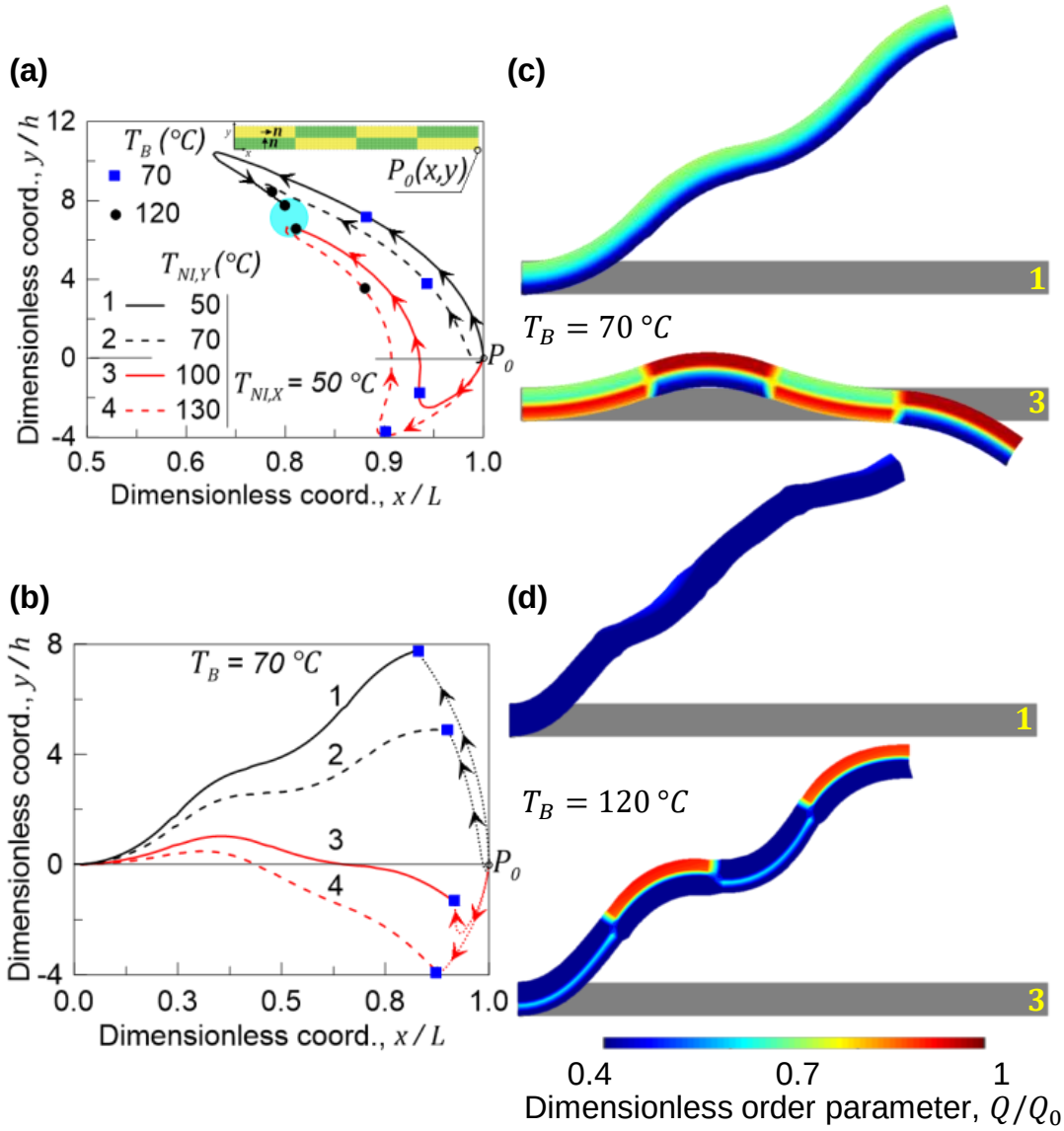

Figure 4.16: *Architected LCE cantilever element of Fig. 4.13 (second architected configuration) constituted of LCE blocks with different transition temperatures: (a) paths of the point P by rising up the temperature from $T_B = 25\,°C$ to $T_B = 120\,°C$ and (b) deformed shapes of the middle line at $T_B = 70\,°C$. (c,d) Corresponding contour of the dimensionless order parameter plotted in the deformed configuration of the element, at $T_B = 70\,°C$ and $T_B = 120\,°C$.*

temperatures $T_{NI,Y}$ enables the point P to move from P_0 to the target area moving upward to the left (black paths, $T_{NI,Y} = 50; 70\,°C$) or firstly downward and then upward to the left (red paths, $T_{NI,Y} = 100; 130\,°C$). In this way, the capability of such a point to move toward the desired region by following distinct trajectories, can be harnessed.

4.5.3 Controlled morphing through cross-link density tuning

Differently from the results shown in Sect. 4.5.2, where the morphing capability of LCE-based elements was controlled and tuned by coupling LCE blocks with distinct nematic directors, in this last subsection the controlled morphing of LCE-based elements is obtained by harnessing the effect of the cross-link-density-related-responsiveness [127]. In doing this, three main examples are presented: in the first case, LCE elements made of two superposed layers having the same thickness but different chain concentrations are investigated. In the second case, elements made of two superposed layers with different chain concentrations as well as distinct layer thickness (but without varying the overall geometrical size of the elements), are considered. Finally, in the last case, elements with a graded cross-link density across their thickness are considered.

In all the following examples, LC mesogens are oriented parallel to the x-axis for each of the considered element, without any encoded pattern; the investigated structure is the beam-like element (cantilever) considered in the previous section with $Q_0 = 0.3$, $c = 20$, $T_{NI} = 50\,^{\circ}C$. The thermal conductivity and specific heat are assumed to be $k = 0.8\,W/mK$ and $C = 1050\,J/KgK$, respectively. In order to ensure a uniform thermal diffusion in the LCE element, the bottom surface of the element was heated slowly, by applying a temperature rate of $\dot{T} = 2.083\,^{\circ}Cs^{-1}$. In all the examples, the actual cross-link density of the LCE material is assumed to be in region II of the self-deformation effectiveness diagram (see Fig. 4.5). The limit chain concentrations defining region II, $\overline{c}_a$ and c_t, expressed through the corresponding limit of the shear moduli $\overline{\mu}_a$ and μ_t, are assumed as follows: $\overline{\mu}_a = \overline{c}_a k_B T = 0.4\,MPa$ and $\mu_t = c_t k_B T = 6\,MPa$, whereas $\alpha_{II} = 2$, (see Eq. 4.13).

Let's consider now the first two examples involving LCE bi-layer elements. By assuming the two connected layers to be synthesized with distinct photopolymerization setups, each one results to be characterized by its own cross-link density, namely ${c_a}^{(1)}$ (bottom layer) and ${c_a}^{(2)}$ (top layer).

In the first example, the LCE beam-like element is made of two superposed layers with the same thickness $h/2$ and different c_a. The thermo-mechanical responsiveness has been simulated by assuming the bottom layer with cross-link density ${c_a}^{(1)}$ (shear modulus $\mu^{(1,A)} = 5\,MPa$), while the upper layer has different cross-link densities. The LCE elements are identified by the corresponding relative cross-link density, namely ${c_a}^{(1)}/{c_a}^{(2)} = 1; 1.04; 1.25; 2.5$. The deformed shapes of the middle line of the LCE elements are displayed in Fig. 4.17(a,b) for two distinct temperature levels, $T_B/T_{NI} = 0.75; 2$. As it can be appreciated, the LCE element simply contracts when ${c_a}^{(1)}/{c_a}^{(2)} = 1$ whereas a bending responsiveness gradually arises by increasing the cross-link density ratio, ${c_a}^{(1)}/{c_a}^{(2)} = 1.04; 1.25; 2.5$. The bending response occurs with a curvature towards the upper layer (the softer one) and is more pronounced by increasing the temperature. The maximum actuation has been obtained for ${c_a}^{(1)}/{c_a}^{(2)} = 2.5$ (see blue dashed lines in Fig. 4.17). The deformed shapes and the corresponding dimensionless order parameter fields for ${c_a}^{(1)}/{c_a}^{(2)} = 1.04$ and ${c_a}^{(1)}/{c_a}^{(2)} = 2.50$ are displayed in Fig. 4.18 for three different temperature levels; the dimensionless order parameter is uniform for each considered temperature, because of the slow thermal evolution; however, the LCE elements display bending upon increasing the temperature (which induces a decrease of Q) because of a different

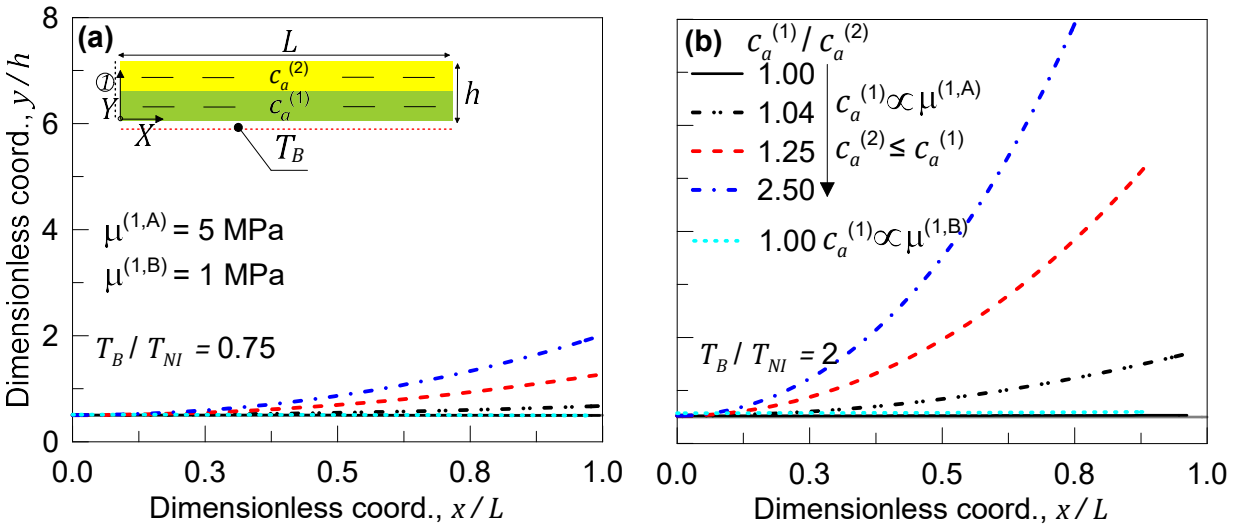

Figure 4.17: *Deformed shapes of the middle line of LCE bi-layer elements for different relative cross-link density ratios (bottom to top), namely* $c_a{}^{(1)}/c_a{}^{(2)} = 1; 1.04; 1.25; 2.50$*, at a fixed relative thickness ratio. Results are plotted at two different temperatures, (a)* $T_B/T_{NI} = 0.75$ *and (b)* $T_B/T_{NI} = 2$*.*

microscopic strain effectiveness of the two superposed layers. Considering the particular case with $c_a{}^{(1)}/c_a{}^{(2)} = 1$, but with a lower $c_a{}^{(1)}$ ($\mu^{(1,B)} = 1\,MPa$, a softer material with respect to the previous one), the LCE element contracts more compared to the previous case with $\mu^{(1,A)} = 5\,MPa$, see Fig. 4.17. In fact, the shear modulus $\mu^{(1,B)} = 1\,MPa$ is well below the assumed limit shear modulus μ_t compared to the case $\mu^{(1,A)} = 5\,MPa$.

In the second example, the controlled morphing is obtained by tuning the relative thickness of the two layers with different fixed cross-link densities. Two cases characterized by two relative cross-link density ratios (bottom to top), namely $c_a{}^{(1)}/c_a{}^{(2)} = 1.25$ and $c_a{}^{(1)}/c_a{}^{(2)} = 2.5$, are considered: the relative thickness of these layers is made to vary. The investigated bi-layer LCE element is identified by its relative thickness ratio, i.e. $h^{(1)}/h^{(2)} = 1; 4; 9$. The bending response is shown in Fig. 4.19(a,b) for two different relative cross-link density ratios at a fixed dimensionless temperature $T_B/T_{NI} = 2$. The maximum bending actuation is obtained by the bi-layer LCE element made of two identical layers ($h^{(1)}/h^{(2)} = 1$). The bending capability decreases by increasing the extension of the lower layer with respect to the upper one. In the limit case $h^{(1)} \to h$, the simple contraction displayed in Fig. 4.17 is recovered. For a fixed value of the relative thickness ratio, a higher cross-link density ratio provides a larger bending actuation.

The deformed shapes as well as the corresponding dimensionless order parameter fields for $c_a{}^{(1)}/c_a{}^{(2)} = 1.25$ and $c_a{}^{(1)}/c_a{}^{(2)} = 2.50$ for two different relative thickness ratios, namely $h^{(1)}/h^{(2)} = 4$ and $h^{(1)}/h^{(2)} = 9$, are displayed in Fig. 4.20; similarly to the previous example, the dimensionless order parameter fields is uniform for each considered temperature, however elements display bending by increasing the temperature. It can be noticed that the bending responsiveness is more pronounced for lower values of the relative thickness ratio $h^{(1)}/h^{(2)}$. The last example considers a

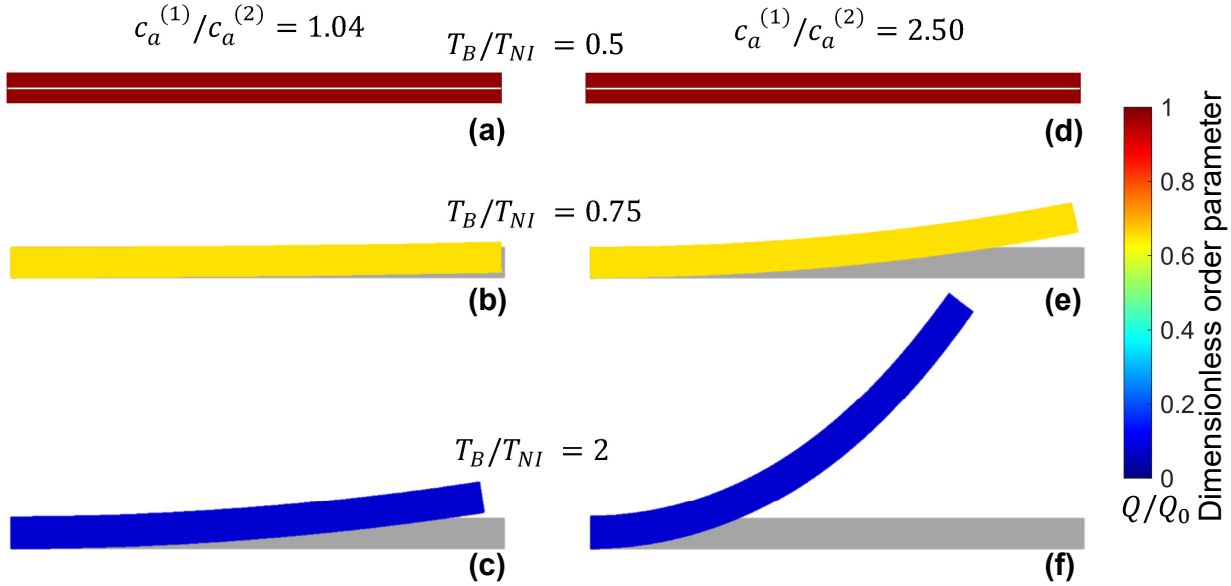

Figure 4.18: *Deformed shapes of the bi-layer LCE element and corresponding order parameter fields; the results are obtained by adopting different cross-link density ratios for the two constituting layers, i.e. (a,b,c)* $c_a^{(1)}/c_a^{(2)} = 1.04$ *and (d,e,f)* $c_a^{(1)}/c_a^{(2)} = 2.50$*, for three different temperatures* T_B/T_{NI}*, respectively.*

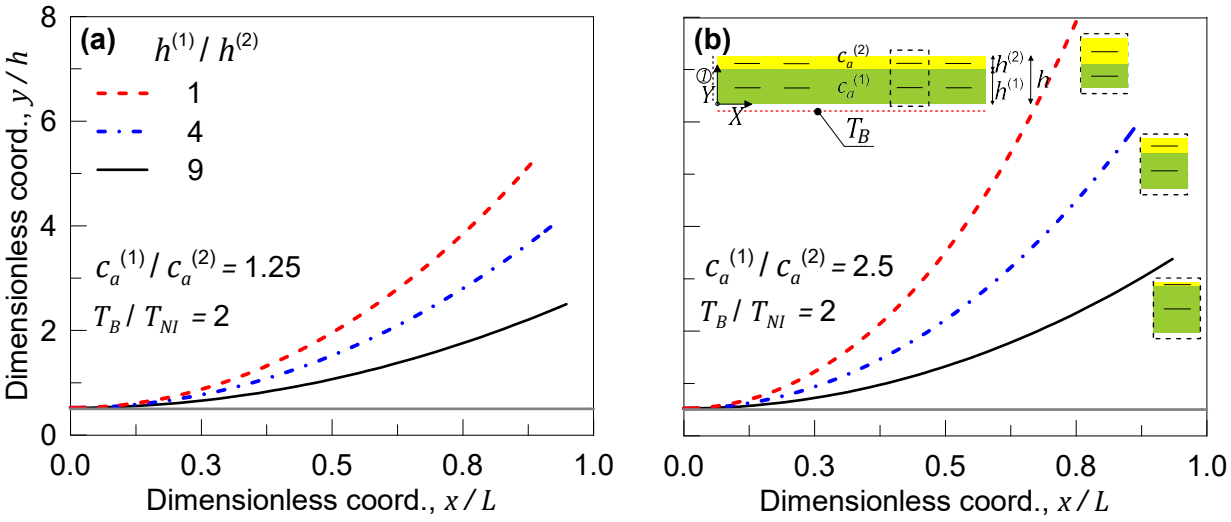

Figure 4.19: *Deformed shapes of the center line of bi-layer LCE element for different relative thickness ratios, namely* $h^{(1)} = h^{(2)} = 1;4;9$*, with (a)* $c_a^{(1)}/c_a^{(2)} = 1.25$ *and (b)* $c_a^{(1)}/c_a^{(2)} = 2.5$*. In both cases, results are plotted for the bottom surface dimensionless temperature equal to* $T_B/T_{NI} = 2$*.*

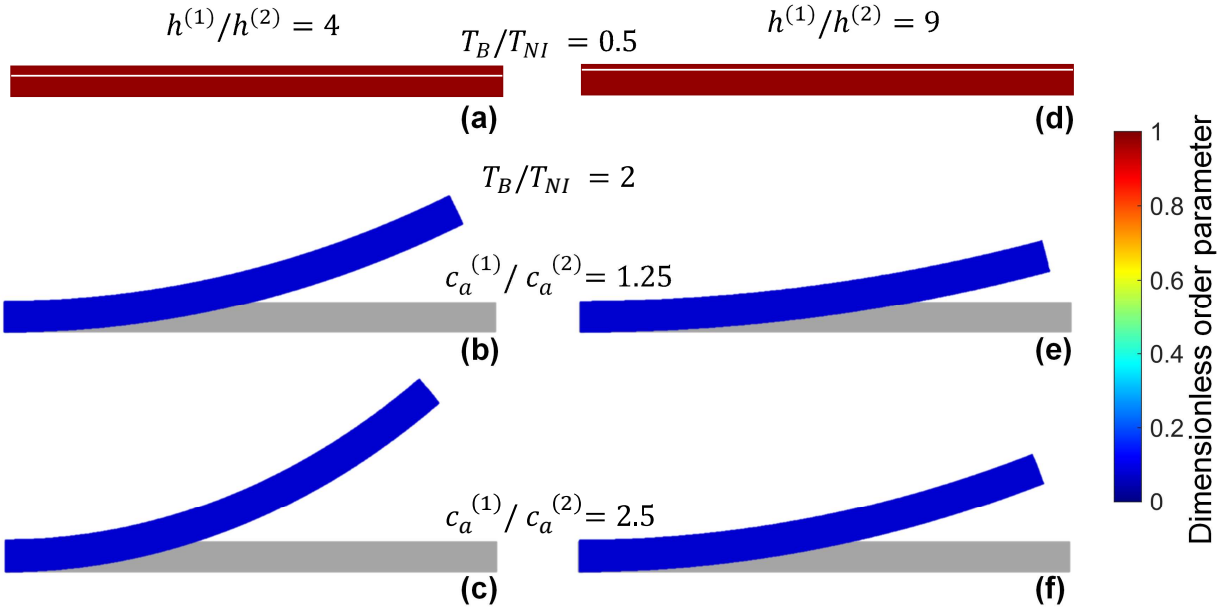

Figure 4.20: *Deformed shapes and corresponding order parameter fields of the bi-layer LCE element for different relative layer thickness ratios, (a,b,c)* $h^{(1)}/h^{(2)} = 4$ *and (d,e,f)* $h^{(1)}/h^{(2)} = 9$*, by adopting different cross-link density ratios* ${c_a}^{(1)}/{c_a}^{(2)} = 1.25; 2.5$*, respectively. Results for two temperatures* $T_B/T_{NI} = 0.5; 2$ *are shown.*

LCE beam-like element characterized by a graded distribution of the cross-link density through the thickness. From a technological viewpoint this can be obtained by synthesizing the element layer-by-layer (as typically occurs in 3D printing technology) and using a different photopolymerization setup to successively cure each layer made the element. Similarly to the previous examples, the LC mesogens are simply parallel to the x-axis.

Various LCE beam-like elements have been simulated: the cross-link density of the top region of the element is assumed to be fixed and equal to $c_a^{(T)} = \overline{c}_a$, whereas the cross-link density varies linearly through the thickness with different gradients up to the value $c_a^{(B)} = \alpha \overline{c}_a$ (where $\overline{c}_a$ represents the cross-link density corresponding to $\overline{\mu} = 0.4\ MPa$) at the bottom part of each element. The parameter α, defined as $g = (\alpha - 1)/h$, sets the cross-link density gradient through the thickness of the elements. Four cases are considered, $\alpha = 2.5; 5; 7.5; 10$. As it can be noticed from the deformed shapes of the middle line of each element, Fig. 4.21(b), a greater gradient of the cross-link density (Fig. 4.21(a)), entails a more pronounced bending responsiveness for a given thermal stimulus. The deformed shapes of different LCE graded elements are displayed in Fig. 4.21(c) for different values of α; the same figure also illustrates the dimensionless order parameter plotted in the deformed configuration, for two different temperatures. The actuation amplitude can be increased up to four times by amplifying the cross-link density gradient from $g = (\alpha - 1)/h = 1.5/h$ to $g = (\alpha - 1)/h = 9/h$. Therefore, g represents a suitable design parameter to be used for controlling the material microstructure, in order to design devices with a desired actuation capability.

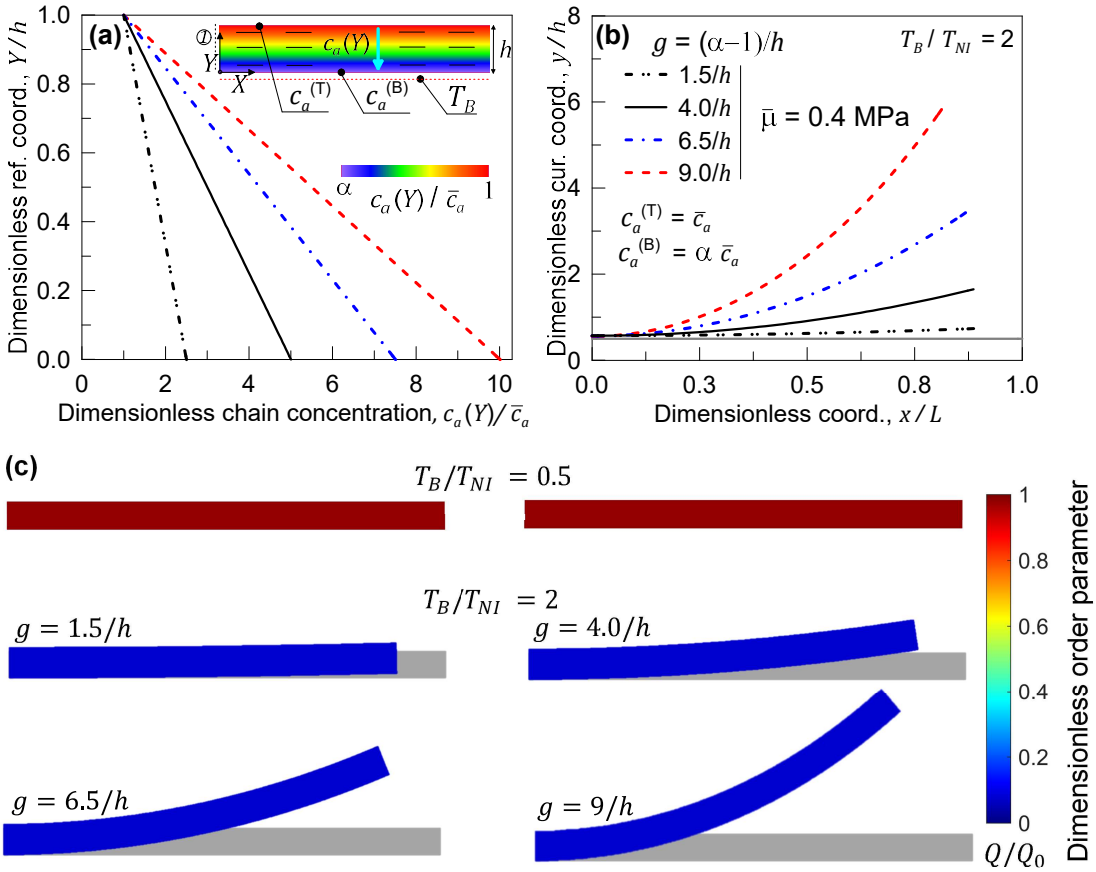

Figure 4.21: *Morphing of LCE-based elements obtained by grading the cross-link density across the element's thickness. (a) Dimensionless cross-link density vs dimensionless reference vertical coordinate. (b) Corresponding deformed shapes (center line) of the elements for different values of the parameter g, at* $T_B/T_{NI} = 2$. *(c) Deformed shapes of the elements and contour of the dimensionless order parameter, for the elements considered in (b), at two different dimensionless temperatures* $T_B/T_{NI} = 0.5; 2$.

In this chapter, a micromechanical-based model suitable for investigating the mechanical response of thermally-responsive-LCEs has been developed. The presented model takes into account the physics-based description evolution of the polymer network at the microscale, which governs the macroscopic shape-change of the material. The model has demonstrated to properly describe the various shape-morphing of LCE-based elements. The parameters involved in the model have a clear physical meaning: they represent specific characteristics of the polymer (such as the nematic orientation, the nematic-transition temperature and the cross-link density) which can be physically imprinted within the LCE matrix by means of the synthesis process (*process-microstructure-responsiveness* relationship). The model has been validated with experimental outcomes as well as with literature results. Numerical simulations aimed at controlling and programming the shape-morphing of LCE-based elements, have been performed. The adopted engineering approach and the results of

the present investigation represents a promising starting point for the design and development of innovative LCE-based -materials, -devices, -structures etc.

CHAPTER 5

PROGRAMMABLE RESPONSE OF PHOTOPOLYMERIZED MATERIALS

Photopolymerized materials can display different mechanical responses by varying the way the initial liquid resin is synthesized (photopolymerization setup).

The aim of this chapter is to develop a multi-physics model for describing the mechanical response of photopolymerized materials in relation to their synthesis process. The model is then exploited to investigate the possibility to program the mechanical response of elements made of these polymeric materials.

The chapter is organized as follows: sect. 5.1 presents an overview and an introductory discussion on photopolymerized materials. In Sect. 5.2 a multi-physics model of the photopolymerization process, coupled with a micromechanical description of polymeric materials, is proposed. In sect. 5.3 the optimal printing of a photopolymerized element is studied. Sect. 5.4 illustrates the finite element implementation of the model as well as its validation, while in Sect. 5.5 some examples illustrating the possibility of tuning and programming the mechanical response of photopolymerized elements are shown.

5.1 Overview and introductory discussion

Photopolymerization is a well-known fabrication technique which allows synthesizing solid polymeric materials by exposing an initial liquid resin (bulk material) to a light source. Recently, the basic principles of this technique have been implemented in modern AM technologies, such as the stereolithography (STL) or the digital light processing (DLP), which enable fabricating polymeric components of any shape, by harnessing a selective and controlled exposure of the bulk material either to a moving UV-laser (STL) or to a light projector (DLP), [133, 134]. As recalled in the previous chapter, this technique is also exploited in the synthesis of LCE materials to polymerize a

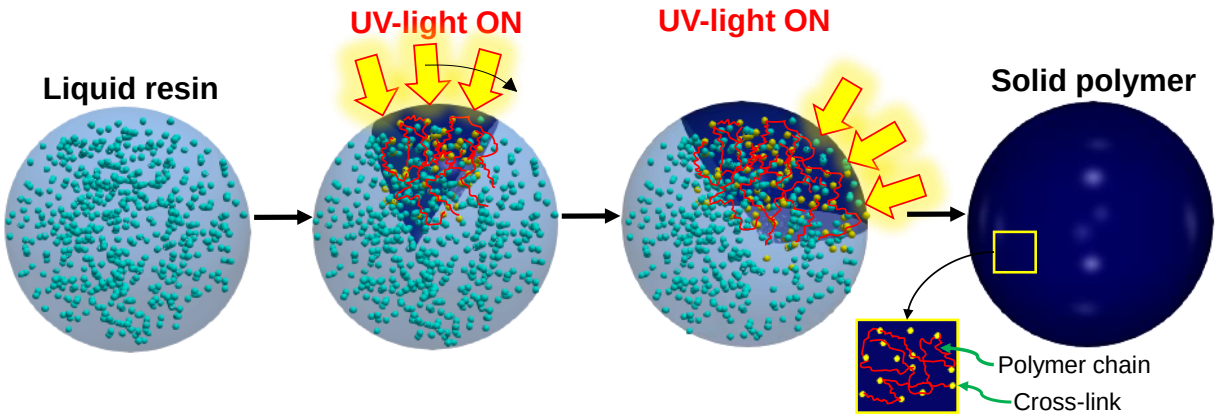

Figure 5.1: *Ideal scheme of the photopolymerization process: starting from the liquid resin (left-hand side), the final solid polymer (right-hand side) is obtained.*

photosensitive LCE ink (as occurs for instance in the DIW synthesis process).

As it is well-known in the realm of AM, the mechanical performance of the synthesized components are related to the process parameters used during synthesis [134–137]. From a functional perspective, distinct mechanical responses can arise from elements obtained through different photopolymerization setups (by tuning UV-laser light intensity, curing time, etc.).

In order to suitably describe the mechanical behavior of photopolymerized materials, a proper theoretical and computational model of the synthesis process represents a necessary starting point.

Early studies adopted energetic approaches for modeling the photopolymerization process: the material is assumed to be solidified when a threshold energy limit is provided to the system, [138, 139]. Kinetic models of photopolymerization have been also proposed [140–144]: these models do not simply consider the liquid-solid transition phenomenon; in fact, the solid phase can exist in different states (degrees of cure) displaying corresponding different mechanical properties, due to different photopolymerization setups. All the above-mentioned studies were mainly based on a pure description of the photopolymerization process, whereas its link to the mechanical behavior of photopolymerized components is still in its infancy [134–136, 145].

In this chapter, the process-microstructure-responsiveness relationship is exploited to encode different mechanical responses in structural elements by harnessing the photopolymerization process. To this end, a chemical-physics-based model for simulating the solidification (curing) of a liquid-resin material, coupled with a micromechanical-based description of a polymeric material, is proposed.

5.2 Multiphysics modeling of photopolymerized materials

In order to study the mechanical response of photopolymerized materials, the proposed approach follows two sequential routes: (1) simulation of the photopolymerization process and (2) mechanical

description of the obtained material.

Modeling the photopolymerization process requires three ingredients: (a) evaluation of the light propagation triggering the chemical species evolution, (b) assessment of the chemical species evolution through kinetics relations and (c) computing the corresponding mechanical properties evolution in the domain under photopolymerization. Finally, the mechanical behavior of the synthesized material is described by means of a micromechanical-based model.

5.2.1 Kinetics modeling of the chemical species and mechanical properties evolution

The chemical-physics problem of the light-induced polymerization, is usually described by a set of differential equations quantifying the evolution of the chemical species constituting the material [135, 136, 146]. The evolution of the chemical species can be related to the mechanism of the polymer chains formation, here assumed to occur without any deformation of the domain during synthesis ($\mathbf{F} = \mathbb{1}$). The kinetic mechanism of the chemical species allows determining the active chain concentration c_a (cross-link density), which affects the mechanical behavior of the polymer network. This quantity can be related to the so called degree of cure (DoC, degree of polymerization or degree of conversion) denoted with ϱ, which in turn is affected by the chemical species evolution.

The material to be photopolymerized is typically formed by distinct chemical species, some already present in the un-cured state (bulk material, such as the liquid monomer (M) and the photo-initiators (Ph_I)); other species appear during or at the end of the process, such as free radicals/cross-link sites (R) and growing or growth polymer chains (P or P_{end}).

When the light is spread into the material, photo-initiator molecules are converted into free radicals. The molar concentration of photo-initiators $C_I(\mathbf{X}, \tau)$, whose initial value is $C_I(\mathbf{X}, \tau = 0) = C_{I0}\ \forall \mathbf{X} \in \mathscr{B}_0$, is gradually consumed in order to enable the production of free radicals, thus providing an increase of their concentration $C_R(\mathbf{X}, \tau)$. Free radicals react with monomer molecules promoting the polymer chains formation; therefore, the evolution of the free radicals concentration is a trade-off between free radicals generated by photo-initiators and free radicals consumed by monomer molecules to form polymer chains. Thus, the monomer concentration $C_M(\mathbf{X}, \tau)$, whose initial value is $C_M(\mathbf{X}, \tau = 0) = C_{M0}\ \forall \mathbf{X} \in \mathscr{B}_0$, is gradually reduced during the process. A polymer chain P stops propagating (termination, $P \rightarrow P_{end}$), when it encounters and so it binds to, another chain or a cross-link site, see Fig. 5.2(a), [146]. The process is described by a set of chemical reactions displayed in Fig. 5.2(b), that can be modelled by differential equations. The photo-initiators decomposition (reaction 1 in Fig. 5.2(b)) is modelled by means of Eq. 5.1, while the chemical reactions referred to initiation, propagation and termination of polymer chains (reactions 2-4 in Fig. 5.2(b)) are modelled

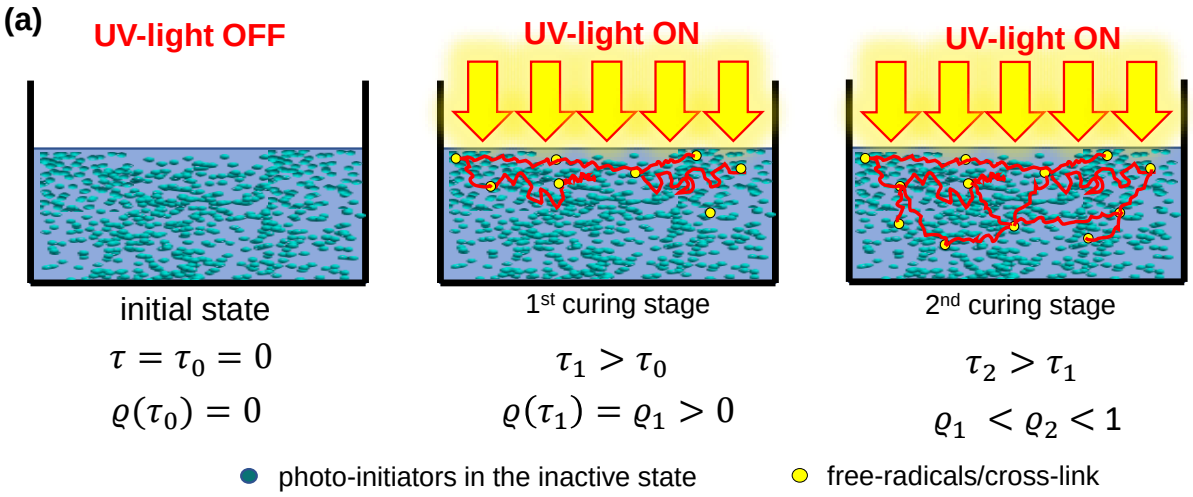

(b)

Scheme of the reactions:

(1) Photo-initiators decomposition: $Ph_I \xrightarrow{k_{pr}} 2R$

(2) Initiation of polymer chains: $R + M \xrightarrow{k_p} P$

(3) Propagation of polymer chains: $P + M \xrightarrow{k_p} P$

(4) Termination: $P + R \xrightarrow{k_t} P_{end}$

$P + P \xrightarrow{k_t} P_{end}$

Figure 5.2: *Scheme of the photopolymerization reactions: (a) evolution of the degree of cure and corresponding growth of polymer chains. (b) Scheme of the chemical reactions governing the process.*

by means of Eqs. 5.2-5.3:

$$\dot{C}_I(\mathbf{X},\tau) = -k_{pr} I(\mathbf{X},\tau) C_I(\mathbf{X},\tau) \tag{5.1}$$

$$\dot{C}_R(\mathbf{X},\tau) = \left| m\dot{C}_I(\mathbf{X},\tau) \right| - m k_t [C_R(\mathbf{X},\tau)]^2 \tag{5.2}$$

$$\dot{C}_M(\mathbf{X},\tau) = -k_p C_M(\mathbf{X},\tau) C_R(\mathbf{X},\tau) \tag{5.3}$$

where m is the number of radicals generated for each photo-initiator involved in the photo-decomposition reaction (it is herein assumed $m = 2$), while k_{pr}, k_p and k_t are the chemical rate constants regulating the involved reactions, namely: the photo-decomposition, the propagation and the termination rate constants, respectively [136, 141, 143]. It is worth mentioning that, both the propagation and the termination rate constants are related to the material properties evolution. In other words, $k_p = k_{p0} \cdot h_p(\varrho(\mathbf{X},\tau))$ and $k_t = k_{t0} \cdot h_t(\varrho(\mathbf{X},\tau))$, where k_{p0} and k_{t0} are the propagation and termination rate constants of the material in the un-cured state ($\varrho = 0$) while h_p and h_t are two functions regulating the diffusion controlled reaction [135, 146].

It is worth mentioning that no transport (mass transfer or migration) has been accounted for in writing Eqs. 5.1-5.3, [135]; from a theoretical viewpoint, since the concentration of the chemical species involved in the problem (I, R and M) varies not only in time but also in space, a migration

of the above mentioned species from regions characterized by different concentration may occur. In order to model mass transfer, a diffusivity term (proportional to the gradient of the species) should be considered in writing the differential equations 5.1-5.3, [147]. As an example, the evolution of the monomer concentration (Eq. 5.3) should be expressed as follows:

$$\dot{C}_M(\mathbf{X},\tau) = \nabla_{\mathbf{X}} \left[\frac{C_M(\mathbf{X},\tau) D_M}{k_B T} \cdot \nabla_{\mathbf{X}} \mu_M \right] - k_p C_M(\mathbf{X},\tau) C_R(\mathbf{X},\tau) \tag{5.4}$$

which, according to the hypothesis made in this dissertation, has been written in the reference configuration assuming that no deformation occurs during photopolymerization. In Eq. 5.4, D_M is the diffusion coefficient of the monomer molecules within the resin; typically it assumes very small values (e.g., $D_M = 5.3 \cdot 10^{-12}\ m^2/s$ for a PEA monomer [147]). In Eq. 5.4, μ_M is the chemical potential of the monomer molecules (related to the monomer concentration), and is conceptually identical to the chemical potential used for modeling the fluid permeation in gels [14]. However, by assuming the speed of the photopolymerization process to be made larger than the space-diffusion of the reacting molecules, the diffusivity term can be reasonably neglected. In other words, by considering Eq. 5.4, the photochemical reaction term (second term on the righ-hand side) is much greater than the space-diffusion term (first term on the righ-hand side).

The system of differential equations 5.1-5.3 can be solved by imposing the initial conditions on the chemical concentrations, which are characteristic properties of the resin being photopolymerized [146], once the light intensity within the irradiated domain has been determined (Sect. 5.2.2). The solution of the system allows computing the concentration of each chemical species as the photopolymerization proceeds, thus enabling the evaluation of the degree of cure as follows [135]:

$$\varrho(\mathbf{X},\tau) = 1 - \frac{C_M(\mathbf{X},\tau)}{C_{M0}(\mathbf{X})} \tag{5.5}$$

which physically represents the amount of monomer molecules converted into polymer chains [146], see Fig. 5.2(a).

It has been experimentally shown that as the photopolymerization proceeds, the mechanical stiffness of the material upon overcoming the gelation point increases according to an exponential law [135, 148]. The chain concentration of the polymer network is related to the shear modulus of the material through $\mu(\mathbf{X},\tau) = c_a(\mathbf{X},\tau) k_B T$ [149]. It is here assumed the chain concentration c_a to be related to the degree of cure by means of the following equation:

$$c_a(\mathbf{X},\tau) = \mathscr{H}\left[\varrho(\mathbf{X},\tau)\right] \cdot \frac{\overline{\mu}}{k_B T} exp\left\{\gamma\left[\varrho(\mathbf{X},\tau) - 1\right]\right\} \tag{5.6}$$

where the Heaviside function has been used to simulate the mechanical stiffness increase occurring beyond the gelation point, i.e. $\mathscr{H} = 0$ for $\varrho(\mathbf{X},\tau) \leq \varrho_{gel}$ or $\mathscr{H} = 1$ for $\varrho > \varrho_{gel}$, while $c_a(\mathbf{X},\tau_{gel}) = c_{a,gel} \cong 0$ is here assumed, [150]. $\overline{\mu}$ represents the shear modulus of the fully-cured polymer (i.e. the maximum achievable shear modulus of the resin being photopolymerized, which is a characteristic property of the resin) while γ is a material-parameter regulating the rate of the mechanical stiffness increase, [145].

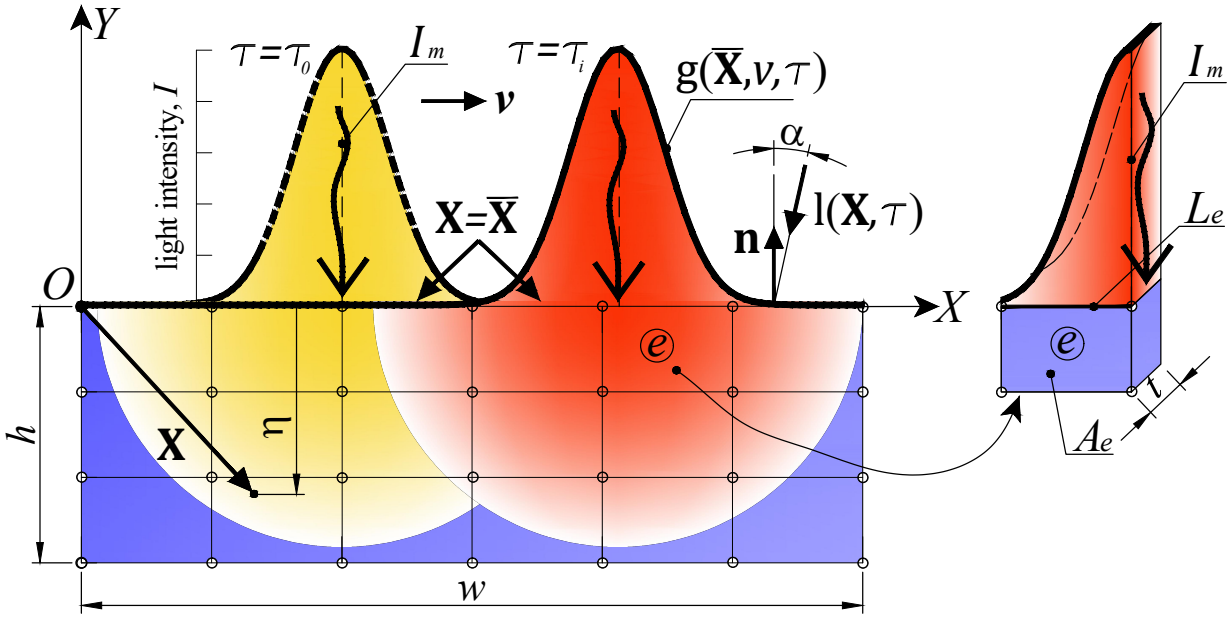

Figure 5.3: *Scheme of the light hitting a continuum body which contains the liquid resin to be photopolymerized (dimensions $w \times h \times s$), discretized into finite elements. The light source is travelling rightward at a velocity v.*

At the end of the photopolymerization process, i.e. after a curing time t_c, the chain concentration can be expressed by adopting an integral equation. In fact, by evaluating the time derivative of the chain concentration from Eq. 5.6, $\dot{c}_a(\mathbf{X},\tau) = \gamma c_a(\mathbf{X},\tau)\dot{\varrho}(\mathbf{X},\tau)$, and determining $\dot{\varrho}(\mathbf{X},\tau)$ from its definition in Eq. 5.5, it holds [145]:

$$c_a(\mathbf{X},t_c) = c_a(\mathbf{X},\tau=0) + \int_{t_{gel}}^{t_c} \dot{c}_a(\mathbf{X},\tau)\,d\tau \tag{5.7}$$

and since typically no polymer chains are present in the liquid monomer state, it can be assumed $c_a(\mathbf{X},\tau=0) \cong 0$, [145].

5.2.2 Light diffusion through a semi-transparent material

When a laser source hits the boundary of the material domain, the light penetrates and spreads within such a domain; the corresponding light intensity inside the material depends on the physics-chemical properties of the semi-transparent material being crossed. In fact, the light intensity is attenuated by the absorbance of the material which depends on the relative absorbance of each substance constituting the material itself. The instantaneous light propagation phenomenon is quantified by the well-known Beer-Lambert law [151]. Let's consider a domain occupied by the material, whose internal region and its boundary in the reference configuration are denoted with $\mathscr{B}_0$ and $\partial\mathscr{B}_0$, respectively; moreover, denoting with $\mathbf{X}$ a generic point within the domain, the following

equation with the corresponding boundary condition hold [151]:

$$\begin{aligned} \mathbf{l}(\mathbf{X},\tau)\cdot\nabla_{\mathbf{X}} I(\mathbf{X},\tau) &= -A(\mathbf{X},\tau)I(\mathbf{X},\tau) \qquad \text{for} \mathbf{X}\in\mathscr{B}_0 \\ I(\mathbf{X},\tau) &= \overline{I}(\mathbf{X},\tau) \qquad\qquad\quad \text{for} \mathbf{X}\in\partial\mathscr{B}_0 \end{aligned} \tag{5.8}$$

where $\nabla_{\mathbf{X}}$ is the gradient operator evaluated in the reference configuration, $\mathbf{l}(\mathbf{X},\tau)$ is the unit vector indicating the direction of the incoming light (here assumed perpendicular to the irradiated boundary), $I(\mathbf{X},\tau)$ is the light intensity at the position $\mathbf{X}$ and time τ, while $A(\mathbf{X},\tau)$ is a coefficient which quantifies the absorbance of the material. Eq. 5.8 represents the Beer-Lambert law written in a general 3D framework with its Dirichlet boundary condition.

The light intensity irradiated on the boundary can be expressed as:

$$\overline{I}(\overline{\mathbf{X}},\tau) = I_m \cdot g(\overline{\mathbf{X}},v,\tau) \tag{5.9}$$

where I_m indicates the maximum light intensity on the irradiated surface at $\mathbf{X}=\overline{\mathbf{X}}$, see Fig. 5.3. The function g is used for quantifying the distribution of the light intensity on the irradiated boundary, because of (a) light scattering from the source and (b) movement of the laser. The speed of the laser source has been denoted with v. A Gaussian distribution function can be reasonably assumed for g:

$$g(\overline{\mathbf{X}},v,\tau) = exp\frac{\left(\left|\overline{\mathbf{X}}\right| - v\tau\right)^2}{c} \tag{5.10}$$

where c is the standard deviation of the Gaussian function depending on the laser source characteristics.

On the other hand, the material absorbance depends on various factors. By following [135], the material absorbance at a generic point $\mathbf{X}$ of the domain can be expressed as follows:

$$A(\mathbf{X},\tau) = A_I\, C_I(\mathbf{X},\tau) + A_{pol}\, \rho(\mathbf{X},\tau) + A_{mon}\,[1-\rho(\mathbf{X},\tau)] \tag{5.11}$$

i.e. as the sum of various contributions. In Eq. 5.11, the photo-initiators with molar absorbance A_I, the monomer absorbance A_{mon} in the un-cured state and the absorbance in the fully-cured state A_{pol} have been considered.

5.2.3 Mechanical behavior of photopolymerized materials

During the photopolymerization process the material is assumed to be in the stress-free state. This implies that while the polymer chains are forming, the statistical distribution of the polymer chains evolves according to the following expression:

$$\rho_0(\mathbf{r},\tau) = \varphi_0(\mathbf{r})\cdot c_a(\tau) \qquad \text{with} \qquad 0\le\tau\le t_c \tag{5.12}$$

φ_0 and c_a being the normalized Gaussian distribution function and the current active chain concentration (cross-link density), see chapter 2. As it can be observed in Eq. 5.12, the active chains

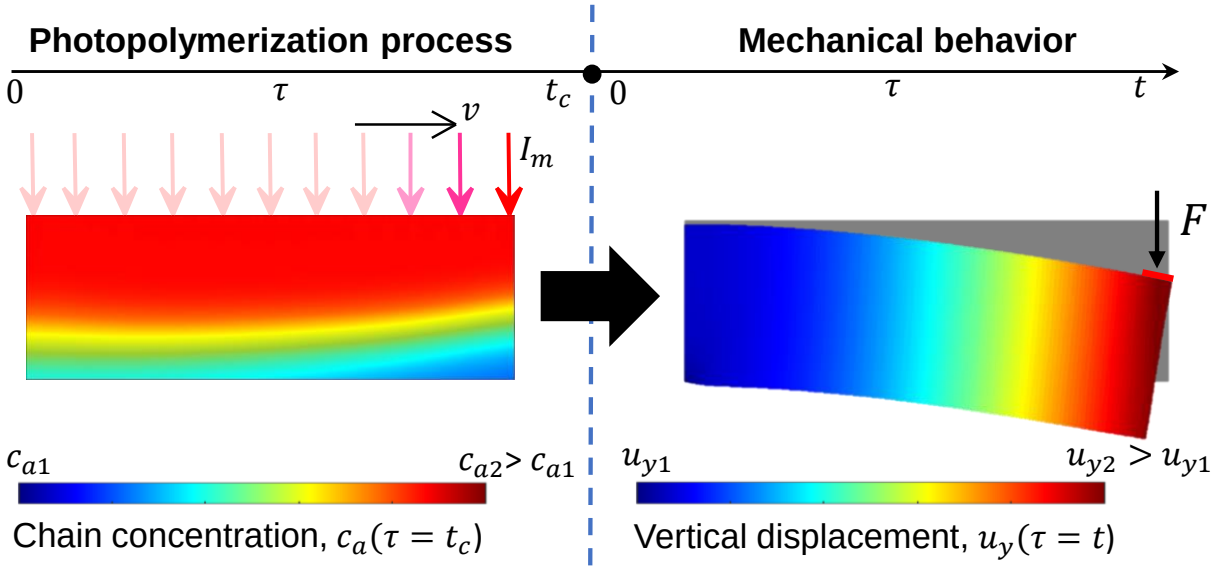

Figure 5.4: *From the photopolymerization process simulation (time history $0 \le \tau \le t_c$) to the mechanical response modeling (time history $0 \le \tau \le t$). The mechanical response of the cured component depends on the mechanical properties imprinted to the component during the photopolymerization.*

concentration is a time-dependent-variable. At the end of the photopolymerization process ($\tau = t_c$), the statistical distribution of the polymer chains in the reference configuration, is given by:

$$\rho_0(\mathbf{r}, t_c) = \varphi_0(\mathbf{r}) \cdot \left(c_a(\mathbf{X}, \tau = 0) + \int_{t_{gel}}^{t_c} \dot{c}_a(\mathbf{X}, \tau)\, d\tau \right) = \varphi_0(\mathbf{r}) \cdot c_\mu \tag{5.13}$$

where the equality $c_\mu = c_a(\mathbf{X}, \tau = 0) + \int_{t_{gel}}^{t_c} \dot{c}_a(\mathbf{X}, \tau)\, d\tau$ has been used in writing the right-hand side of Eq. 5.13. In order not to introduce further dependencies, the number of Kuhn's segments in each polymer chain is assumed to be not influenced by the curing condition, i.e. the forming chains are all chemically identical, while only their concentration c_a is varying in time. $\varphi_0(\mathbf{r})$ is expressed as usual by the Gaussian distribution with N and b characteristic parameters of the resin being printed.

The strain energy density of the material during photopolymerization changes because of chain formation, [145]. It is given by:

$$\Psi(\tau) = c_a(\tau) \langle \varphi_0(\mathbf{r}) \psi_c(\mathbf{r}) \rangle \qquad \text{with} \qquad 0 \le \tau \le t_c \tag{5.14}$$

where ψ_c is the free energy of a single chain based on the Gaussian statistics, see chapter 2. After the photopolymerization process has been completed, the material is supposed to be subjected to external mechanical actions (e.g. stretches, forces, etc.), in the time interval $0 \le \tau \le t$, see Fig. 5.4. In other words, in the proposed model the mechanical problem takes place only after the photopolymerization process was completed. The chain concentration, evaluated as shown in sect. 5.2.1, does not change in time during the mechanical problem, since damage (chains rupture) and

self-healing mechanisms are neglected [145]; it is $c_a = c_\mu \; \forall \tau \in 0 \leq \tau \leq t$. Therefore, the strain energy density of the material in the time interval $0 \leq \tau \leq t$ is given by:

$$\Psi(\tau) = c_\mu \langle \varphi(\mathbf{r},\tau)\psi_c(\mathbf{r})\rangle \qquad \text{with} \qquad 0 \leq \tau \leq t \tag{5.15}$$

where the current value of the chain distribution function $\varphi(\mathbf{r},\tau)$ is evaluated on the basis of the applied mechanical history (chapter 2, sect. 2.3). The strain energy density variation with respect to the reference state, is:

$$\Delta\Psi(\tau) = \Psi(\tau) - \Psi_0(\tau) = c_\mu \langle \big(\varphi(\mathbf{r},\tau) - \varphi_0(\mathbf{r},0)\big)\psi_c(\mathbf{r})\rangle \qquad \text{with} \qquad 0 \leq \tau \leq t \tag{5.16}$$

and the Cauchy stress tensor is computed as:

$$\boldsymbol{\sigma}(\tau) = J^{-1}\mathbf{P}\mathbf{F}^T = c_\mu \langle \big(\varphi(\mathbf{r},\tau) - \varphi_0(\mathbf{r},0)\big)\left(\frac{\partial \psi_c}{\partial \mathbf{r}} \otimes \mathbf{r}\right)\rangle + \pi \mathbb{1} \tag{5.17}$$

It is worth recalling that, if the free energy of an individual chain $\psi_c(\mathbf{r})$ is evaluated according to the Gaussian statistics (suitable for chains not too much stretched), the Cauchy stress tensor can be evaluated by means of the chain distribution tensor as:

$$\boldsymbol{\sigma}(\tau) = \frac{3c_\mu k_B T}{Nb^2}\left(\boldsymbol{\mu}(\tau) - \boldsymbol{\mu}_0\right) + \pi \mathbb{1} \tag{5.18}$$

5.3 Photopolymerization process optimization

The synthesis of a material characterized by desired physical properties by minimizing the energy consumption during its synthesis process, is an important requirement in the field of AM [145]. This challenge can be overcome by facing an optimization problem.

During photopolymerization, the total energy transmitted by the laser source to the material domain can be evaluated as:

$$\Gamma(v, I_m) = \int_0^{t_c} \dot{\Gamma}(\tau) d\tau \qquad \text{with} \qquad t_c = w/v \tag{5.19}$$

The energy rate $\dot{\Gamma}(\tau)$ irradiated by the laser source at the time τ is evaluated as:

$$\dot{\Gamma}(\tau) = I_m \int_0^w g(\overline{\mathbf{X}}, v, \tau) dS \tag{5.20}$$

where S indicates the boundary surface of the domain; a 2D problem with a rectangular irradiated top surface with length w (total length of the laser's path) and unit depth, has been assumed. This energy promotes the reactions of the chemical species in the material to be photopolymerized, [145]. The energy effectively stored in the material can be assumed to be proportional to the chain concentration obtained out of the process as follows:

$$\Gamma_p(v, I_m) \propto \frac{1}{\overline{c}_a V} \int_{\mathscr{B}_0} c_a(\mathbf{X}, v, I_m)\, dV = \frac{C_a(v, I_m)}{\overline{C}_a} \tag{5.21}$$

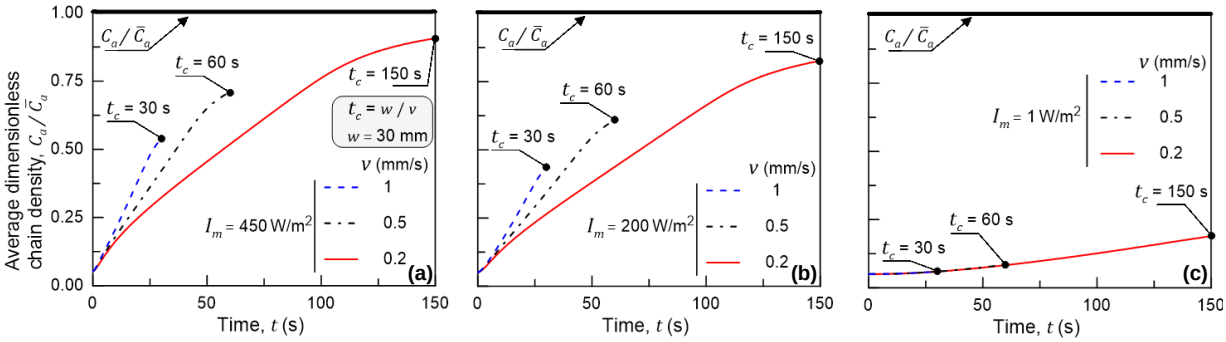

Figure 5.5: *Average dimensionless chain density evolution during the photopolymerization process, for different photopolymerization setups. Adapted from [145].*

A dimensionless form of such an energy has been adopted, where $\overline{C}_a = \bar{c}_a V$ and $C_a(v, I_m) = \int_{\mathscr{B}_0} c_a(\mathbf{X}, v, I_m)\, dV$ are the total number of polymer chains formed in the fully-cured material and in the actual photopolymerized one (in the domain $\mathscr{B}_0$), respectively. The energy in Eq. 5.21 quantifies the level of solidification achieved by the material, taking the fully cured one as the reference (see Fig. 5.5). However, it does not account for the effective total energy spent during the chain formation, $\Gamma(v, I_m)$, since in real cases a fraction of the irradiated energy is not used for solidifying the material. Therefore, the quantity $\Gamma(v, I_m)$ is used in the following for the definition of the minimization problem. In order to evaluate the optimum photopolymerization setup of an element for which a prescribed mechanical target response is sought (for given boundary conditions), the problem is mathematically expressed by the minimization of a suitable objective function. The following normalized target function is introduced for such a purpose:

$$h_{1a}(v, I_m) = \frac{\delta^*(v, I_m) - \overline{\delta}^*}{\delta^*(v, I_m)} + a \frac{\Gamma(v, I_m)}{\Gamma_{max}} \tag{5.22}$$

where $\delta^*(v, I_m)$ represents the displacement at a representative point of the element, $\overline{\delta}^*$ is the target displacement taking place at the same point, Γ_{max} is the maximum value of the energy in the considered domain (introduced here for dealing with dimensionless quantity) whereas a is a weight parameter used to quantify the relative importance of the energy consumption with respect to the mechanical response [145]. By defining $\frac{\delta^*(v, I_m) - \overline{\delta}^*}{\delta^*(v, I_m)} = \delta'(v, I_m)$ and $\frac{\Gamma(v, I_m)}{\Gamma_{max}} = \Gamma'(v, I_m)$, the above objective function can be rewritten as:

$$h_{1a}(v, I_m) = \delta'(v, I_m) + a\Gamma'(v, I_m) \tag{5.23}$$

The formulated optimal problem consists in minimizing the objective function in order to determine the most appropriate values of v and I_m to be used for the photopolymerization of the material. When the optimization problem is aimed at minimizing the compliance of an element (Sect. 5.5.2), the target displacement can be assumed to be equal to that of a fully-cured component.

It is worth mentioning that, according to the desired characteristics of the mechanical response in turn, other objective functions can be introduced. For instance, if the lowest degree of the viscous

behavior of the synthesized material must be attained, the following objective function can be used:

$$h_{2\beta}(v,I_m) = \left[1 - \frac{\tilde{\tau}_r(v,I_m)}{\overline{\tau}_r}\right] + \beta\,\Gamma'(v,I_m) = \tau'_r(v,I_m) + \beta\,\Gamma'(v,I_m) \tag{5.24}$$

In Eq. 5.24, $\frac{\tilde{\tau}_r(v,I_m)}{\overline{\tau}_r} = \frac{\int_{\mathscr{B}} c_a^{1/3}(\mathbf{X},v,I_m)dV}{V\,\overline{c}_a^{1/3}}$ is the viscosity-related term, with $\tilde{\tau}_r$ and $\overline{\tau}_r$ representing the average relaxation time of the actual photopolymerized material and of the fully-cured one, respectively, [145]. On the other hand, similarly to the parameter a introduced in $h_{1a}(v,I_m)$, β is a parameter playing the role of regulating the relative importance of the two terms involved in $h_{2\beta}(v,I_m)$.

The above described minimization problem can be solved by adopting standard algorithms suitable to solve an unconstrained gradient-based optimization problem [152]. The modified Newton's method has been adopted in the present study; starting from an arbitrary point in the design domain, in this particular case identified by the independent design variables v and I_m, the algorithm operates by searching the optimal solution identified by design variables $\overline{v}$ and $\overline{I}_m$ (corresponding to the minimum value of the adopted objective function). This can be achieved by performing a line search along the so-called Newton directions [145]. The solution is obtained by an iterative procedure which requires the computation of the Hessian of the objective function h_j:

$$\tilde{\mathbf{H}}_j(\boldsymbol{\xi}_k) = \nabla^2 h_j(\boldsymbol{\xi}_k) \tag{5.25}$$

where j is an index which simply identifies the objective function of the problem of interest, i.e. $h_j = h_{1a}$ or $h_j = h_{2\beta}$ according to the cases illustrated above. The Hessian matrix contains the second-derivatives of the objective function evaluated with respect to its independent design variables, in the design space. $\boldsymbol{\xi}_k = (v_k, I_{mk})$ is a vector which contains the design variables at the iteration $k = 1,2,...,M$, where M is the maximum number of iterations to be performed. The search direction at the iteration k is represented by a vector which can be evaluated as follows:

$$\mathbf{p}_j(\boldsymbol{\xi}_k) = -\tilde{\mathbf{H}}_j^{-1}(\boldsymbol{\xi}_k)\mathbf{d}_j(\boldsymbol{\xi}_k) \tag{5.26}$$

where $\mathbf{d}_j(\boldsymbol{\xi}_k) = \nabla h_j(\boldsymbol{\xi}_k)$ is the gradient of the objective function at the point $\boldsymbol{\xi}_k$. The vector $\boldsymbol{\xi}_k$ is iteratively updated during the procedure as follows:

$$\boldsymbol{\xi}_{k+1} = \xi_k + \tilde{\gamma}_k\,\mathbf{d}_j(\boldsymbol{\xi}_k) \tag{5.27}$$

In order to evaluate $\boldsymbol{\xi}_{k+1}$ according to Eq. 5.27, the so-called step length $\tilde{\gamma}_k$ has to be firstly computed: it represents a scalar parameter required for moving forward the solution along the direction $p_j(\boldsymbol{\xi}_k)$. It can be evaluated according to the condition $h_j(\boldsymbol{\xi}_k + \tilde{\gamma}_k\,\mathbf{p}_j(\boldsymbol{\xi}_k)) < h_j(\boldsymbol{\xi}_k)$, [145]. The iterative procedure mathematically described by Eqs. 5.25-5.27 is arrested when a proper convergence criterion on the h_j gradient is fulfilled.

5.4 Finite element implementation and validation

The above described model is coded in a computational framework made of two main blocks solved in an uncoupled way: in the first block, the light diffusion problem as well as the kinetics of photopolymerization are solved. In the second block, the mechanical problem is performed. It is worth highlighting that when the mechanical problem is performed (second block), the mechanical properties of the material are an output of the first block, so the two problem are linked (process-microstructure-responsiveness relationship).

Firstly, the implementation of the light diffusion problem is described. In order to code the Beer-Lambert law in a computational framework, the use of the weak form of the governing equations is necessary and so it has been addressed. This can be obtained by introducing a proper functional of the problem or, alternatively, by transforming the strong form Eq. 5.8 into a weak (integral) formulation by introducing a weight function $W(\mathbf{X})$, [146]. The Beer-Lambert law and the related essential boundary conditions are multiplied by the weight function and integrated over the domains of the problem:

$$\begin{aligned} \int_{\mathscr{B}_0} W(\mathbf{X})\, \mathbf{l}(\mathbf{X},\tau)\cdot\nabla_{\mathbf{X}} I(\mathbf{X},\tau)\, dV &= -\int_{\mathscr{B}_0} W(\mathbf{X})\, A(\mathbf{X},\tau) I(\mathbf{X},\tau)\, dV \qquad \text{for} \mathbf{X}\in\mathscr{B}_0 \\ \int_{\partial\mathscr{B}_0} W(\mathbf{X})\, I(\mathbf{X},\tau)\, dS &= \int_{\partial\mathscr{B}_0} W(\mathbf{X})\bar{I}(\mathbf{X},\tau)\, dS \qquad \text{for} \mathbf{X}\in\partial\mathscr{B}_0 \end{aligned} \tag{5.28}$$

The light beam vector field is assumed to be constant in space and time, i.e. $\mathbf{l}(\mathbf{X},\tau)=\bar{\mathbf{l}}$ (with $\bar{\mathbf{l}}$ the unit vector defining the vertical direction). By harnessing the equality $\int_{\mathscr{B}_0} W(\mathbf{X})\,\mathbf{l}(\mathbf{X},\tau)\cdot\nabla_{\mathbf{X}} I(\mathbf{X},\tau)\, dV = \int_{\partial\mathscr{B}_0} W(\mathbf{X})\cdot I(\mathbf{X},\tau)\,\mathbf{l}(\mathbf{X},\tau)\,\mathbf{n}\, dS - \int_{\mathscr{B}_0} I(\mathbf{X},\tau)\,\mathbf{l}(\mathbf{X},\tau)\cdot\nabla_{\mathbf{X}} W(\mathbf{X})\, dV$ provided by the divergence theorem ($\mathbf{n}$ being the outward unit vector normal at $\mathscr{B}_0$), the first term of the first line of Eq. 5.28 can be rewritten. The following weak form can be finally obtained:

$$\int_{\mathscr{B}_0} \nabla_{\mathbf{X}} W(\mathbf{X})\, I(\mathbf{X},\tau)\bar{\mathbf{l}}\, dV - \int_{\mathscr{B}_0} W(\mathbf{X}) A(\mathbf{X},\tau) I(\mathbf{X},\tau)\, dV = \int_{\partial\mathscr{B}_0} W(\mathbf{X})\bar{I}(\mathbf{X},\tau)\,\bar{\mathbf{l}}\cdot\mathbf{n}\, dS \tag{5.29}$$

By introducing a proper discretization of the domain into finite elements and by interpolating the involved field variables through the corresponding nodal values, the above weak form can be rewritten in matrix form:

$$[\mathbf{H}(\tau)+\mathbf{A}(\tau)+\mathbf{M}]\tilde{\mathbf{I}}(\tau)=\mathbf{G}(\tau) \tag{5.30}$$

where $\mathbf{H}=\mathbb{A}_{e=1}^{ne}\mathbf{H}_e$, $\mathbf{A}=\mathbb{A}_{e=1}^{ne}\mathbf{A}_e$, $\mathbf{M}=\mathbb{M}_{e=1}^{ne}\mathbf{M}_e$ are the light gradient, absorbance and stabilization global matrices, respectively, where $\mathbb{A}$ is the assembly operator and ne is the number of finite elements. In Eq. 5.30, $\mathbf{G}$ is the (known) global vector of the nodal values of the light intensity irradiating the boundary of the domain under photopolymerization. $\tilde{\mathbf{I}}$ is the global vector of the sought nodal values of the light intensity (which also contains the unknowns of the problem, i.e. the light intensity values inside the domain). The corresponding matrices, as well as the vector of the

incoming light intensity, can be determined as follows:

$$\begin{aligned}
\mathbf{H}_e(\tau) &= \int_{V_e} [B]^T \bar{\mathbf{l}} [N]\, dV \\
\mathbf{A}_e(\tau) &= -\int_{V_e} [N]^T A(\mathbf{X},\tau)[N]\, dV \\
\mathbf{M}_e(\tau) &= Q h_e \int_{V_e} [B]^T [B]\, dV \\
\mathbf{G}_e(\tau) &= \int_{S_e} [N]^T I_m \cdot g(\overline{\mathbf{X}}, v, \tau) \cdot l_n \, dS
\end{aligned} \tag{5.31}$$

[N] and [B] being the shape function and the standard compatibility matrix of each element, respectively, while $l_n = \bar{\mathbf{l}} \cdot \mathbf{n} = 1$ where $\alpha = 0$ is assumed (Fig. 5.3).

It is worth mentioning that a stabilization term needs to be added to the weak form through a stabilization matrix $\mathbf{M}$ for numerical reasons; in fact, the presence of only the transport (convective) term $\mathbf{l}(\mathbf{X},\tau) \cdot \nabla_{\mathbf{X}} I(\mathbf{X},\tau)$ in the strong form of the problem (Eq. 5.8) leads to a region, generally close to the boundary, where the solution is characterized by large gradient or oscillations, thus providing meaningless unstable numerical results [146, 153]. The stabilization matrix $\mathbf{M}$, whose addition to the strong form allows overcoming the above-mentioned numerical problem, operates as a fictitious diffusion-like term of the form $Q h_e \nabla_{\mathbf{X}} I(\mathbf{X},\tau)$, with $Q h_e$ being a small number, i.e. the product of a small coefficient Q and a characteristic geometrical size h_e related to the problem in turn [146].

Once the light distribution in $\mathscr{B}_0$ is known at the nodal values of the discretized domain, the corresponding values at the Gauss points (GP), $I_{GP}(\tau)$, can be evaluated through a standard interpolation [146]. This allows evaluating the values of the chemical species concentration by numerically solving the kinetic system illustrated in Sect. 5.2.1. First, the photo-initiator concentration is required; at the time τ and for each GP of each finite element of the discretized domain, it is estimated as:

$$C_{I,GP}(\tau) = C_{I,GP}(\tau_{-1}) + \Delta\tau \left[-k_{pr} I_{GP}(\tau) C_{I,GP}(\tau_{-1}) \right] \tag{5.32}$$

where $\Delta\tau$ is the time step adopted for the numerical integration in the time domain. After the photo-initiator concentration has been determined, the concentration of the other chemical species can be determined [146]. Finally, once all the concentration of the chemical species are known, the degree of cure for each GP can be evaluated as:

$$\varrho_{GP}(\tau) = 1 - \frac{C_{M,GP}(\tau)}{C_{M,GP}(\tau = 0)} \tag{5.33}$$

and, finally, the corresponding chain concentration (when $\varrho_{GP} \geq \varrho_{gel}$) is given by:

$$c_{a,GP}(\tau) = \frac{\overline{\mu}}{k_B T} exp\left\{ \gamma \left[\varrho_{GP}(\tau) - 1 \right] \right\} \tag{5.34}$$

Once the mechanical properties of the actual photopolymerized material have been determined, the mechanical problem can be solved similarly to as it has been illustrated in sect. 4.4, by imposing the mechanical boundary conditions in turn (constraints and mechanical actions).

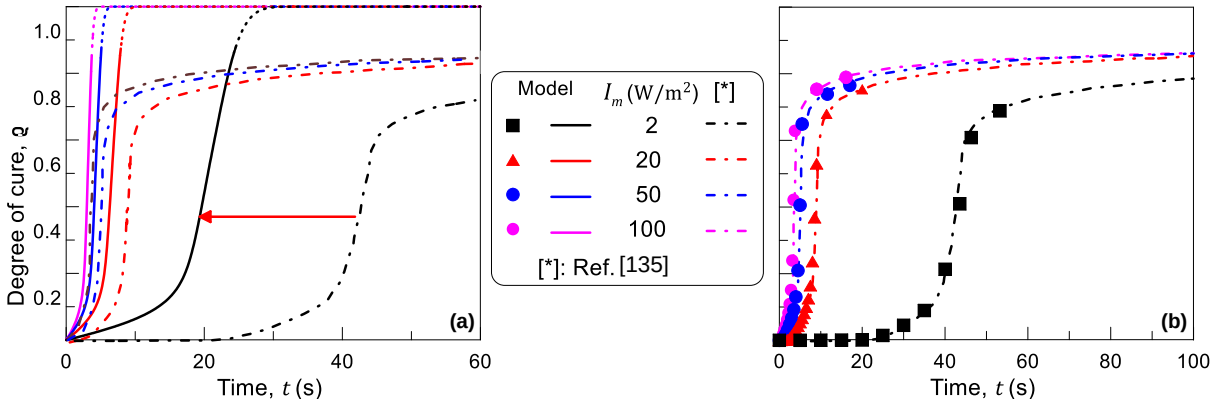

Figure 5.6: *Evolution of the degree of cure quantified by the present multi-physics model by (a) neglecting or (b) considering the role played by the oxygen inhibition. Literature results adopted from [135] are shown for comparison.*

5.4.1 A real case simulation of the photopolymerization process

The simulation of a real-case photopolymerization process reported in [135], is here considered. The monomer used is polyethylene (glycol) diacrylate (PEGDA) with a molecular weight of 250 g/mol, mixed with 0.3 % weight percent of 2,2-Dimethoxy-2-phenylacetophenone as photo-initiator (Sigma-Aldrich, St. Louis, USA) [135]. The FE simulation is performed by assuming a static laser source ($v = 0\, m/s$) applied to a single material point lying on the resin surface.

The propagation and termination rate constants are assumed to depend on the degree of cure, $k_p = k_{p0} \cdot h_p(\varrho)$ with $h_p(\varrho) = \dfrac{1}{1+\left(k_{p0}/k_{p,D0}\right)e^{d\varrho}}$ while $k_t = \dfrac{1}{1/k_{t,SD}+(e^{d\varrho})/k_{t,TD0}} + \dfrac{C_{RD}(1-\varrho)k_{p0}}{1+\left(k_{p0}/k_{p,D0}\right)e^{d\varrho}}$, [135]. In order to take into account the role played by the oxygen inhibition in hindering the photopolymerization process, the expression quantifying the free radicals evolution (Eq. 5.2) is modified as follows [135]:

$$\dot{C}_R(\mathbf{X},\tau) = \left|m\dot{C}_I(\mathbf{X},\tau)\right| - mk_t[C_R(\mathbf{X},\tau)]^2 - k_O C_R(\mathbf{X},\tau)C_O(\mathbf{X},\tau) \tag{5.35}$$

where C_O represents the oxygen concentration and k_O is the rate constant quantifying the oxygen production. This equation represents the actual evolution of free radicals if the oxygen inhibition occurs: free radicals react and so are consumed by the oxygen molecules instead of reacting with monomer molecules to form other polymer chains.

The parameters used in the present simulation, which have been experimentally determined and calibrated in [135], are: $k_{p0} = 1.86048\ m^3/mol\ s$, $k_{p,D0} = 9.994 \cdot 10^8\ m^3/mol\ s$, $k_{t,SD} = 4.39 \cdot 10^3\ m^3/mol\ s$, $k_{t,TD0} = 1.002443 \cdot 10^4\ m^3/mol\ s$, $k_{pr} = 8.999 \cdot 10^{-4}\ m^2/J$, $d = 34.149$ and $C_{RD} = 1.0146$, [135, 145]. The evolution of the degree of cure, evaluated with the present model and compared with the results obtained in [135], are plotted in Fig. 5.6(a,b) for different light intensities. In particular, Fig. 5.6(a) illustrates the model results when the role played by the oxygen is neglected, whereas the curves obtained by considering the oxygen inhibition are displayed in Fig. 5.6(b). The model

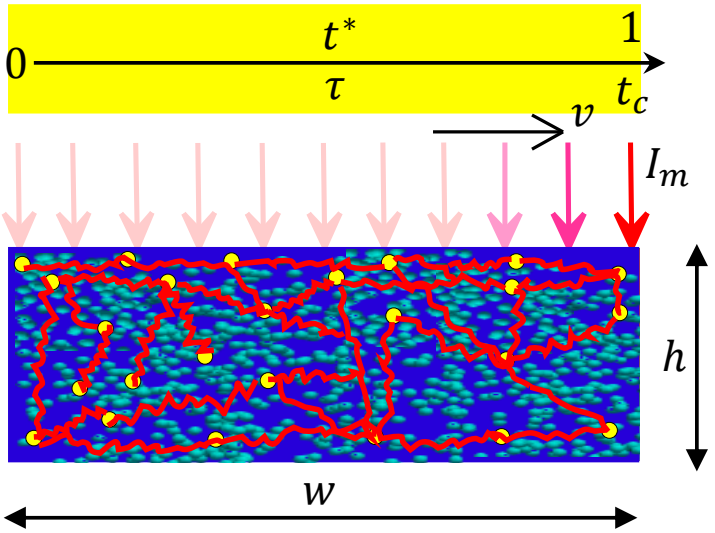

Figure 5.7: *Scheme of the photopolymerization process modeling, involved in the considered examples.*

results are in good agreement with the experimental ones when the oxygen effect is considered, Fig. 5.6(b), while the degree of cure is overestimated when such an effect is neglected, Fig. 5.6(a) [145].

It is worth mentioning that considering the role played by inhibition due to oxygen does not represent a modelling issue but is strictly related to the specific technology used for the photopolymerization synthesis; in fact, the problem related to the oxygen inhibition can be overcome by using physical-chemical methods, for instance by curing in an oxygen-free atmosphere through special barriers or by using additives in the liquid monomer being photopolymerized [146, 154]. In other words, the model assumptions must be consistent with the specific problem in turn and so with the particular conditions of the synthesis process.

5.5 Programming the response through photopolymerization: from the process to the mechanical behavior

In this section, the role played by the main photopolymerization process parameters in affecting the mechanical properties of photopolymerized-based elements is considered; in particular, the role of the laser speed (Sect. 5.5.1.1), the light intensity (Sect. 5.5.1.2) and the material's absorbance (Sect. 5.5.1.3) are investigated. The possibility of programming the mechanical response of polymer-based elements synthesized via photopolymerization, through different photopolymerization process setups, is investigated in Sect. 5.5.2. It is shown how the main process parameters can be tuned in order to obtain a desired mechanical response; finally, the optimization problem (linking photopolymerization process and mechanical problem) is considered. In the following examples, unless differently stated, the 2D domain initially filled with the monomer, is assumed to have the dimen-

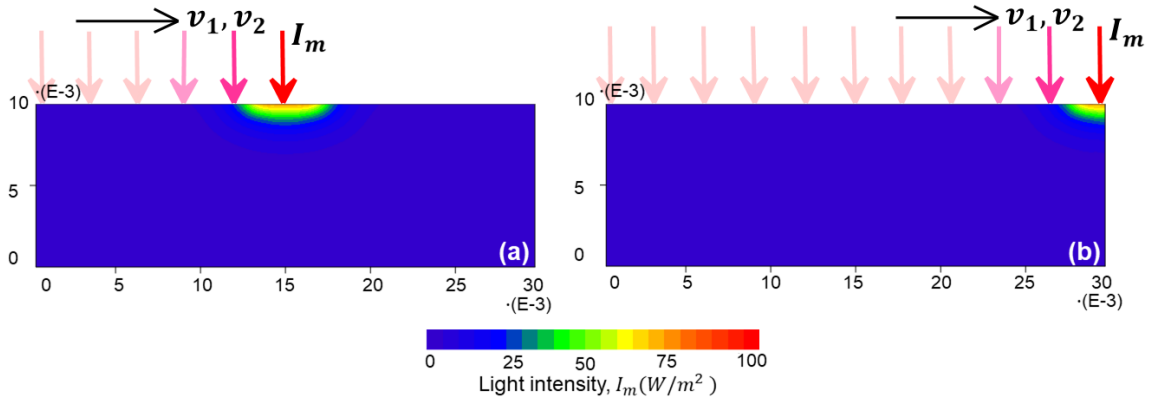

Figure 5.8: *Instantaneous light intensity distribution at (a)* $t^* = 0.5$ *and (b)* $t^* = 1$ *by adopting* $I_m = 150\ W/m^2$ *and two different laser speeds* $v_1 = 1\ mm/s$ *and* $v_2 = 0.1\ mm/s$*. The geometrical dimensions of the domain are expressed in meters.*

sions $h = 10\,mm$ (layer thickness) and $w = 30\,mm$ (width). The curing time required for covering the entire domain under photopolymerization is $t_c = w/v$, being v the laser speed characterizing the process; a dimensionless curing time will be used in the following, namely $t^* = t/t_c$, see Fig. 5.7. The parameters related to the liquid monomer resin are assumed as follows: $C_I(\mathbf{X}, t = 0) = 20\,mol/m^3$, $C_M(\mathbf{X}, t = 0) = 3000\,mol/m^3$; for sake of simplicity, the chemical rate constants are assumed to be constant in time: $k_{pr} = 8 \cdot 10^{-4}\ m^2/J$ and $k_p = k_t = 0.21\ m^3/mol \cdot s$ [135, 143, 146]. Finally, unless differently stated, the material absorbance is assumed to be constant, $A(\mathbf{X}) = 600\,m^{-1}$. Moreover, the shear modulus of the fully cured polymer is assumed to be $\overline{\mu} = 267\,MPa$ and the parameter governing the velocity of the stiffness' increase is set to $\gamma = 3$.

5.5.1 Mechanical properties of photopolymerized materials: assessment through numerical simulations

5.5.1.1 Effect of the laser speed

In this subsection, the effect of the laser speed on the photopolymerization process is investigated. Two photopolymerization setups are adopted. Specifically, two laser speeds are considered, namely $v_1 = 1\,mm/s$ and $v_2 = 0.1\,mm/s$; the maximum laser light intensity is $I_m = 150\,W/m^2$ and $c = 10^{-6}\,m$ in both cases. All the other parameters are kept fixed. The maps of the light intensity distribution, for all the adopted parameters, are displayed in Fig. 5.8(a,b) for two dimensionless curing time, $t^* = 0.5$ (i.e. when the laser has covered one half of the domain being cured) and $t^* = 1$ (i.e. when the laser has covered the entire domain), respectively; since a constant material absorbance is assumed in this example, these maps do not depend by the adopted laser speed. The dimensionless chain concentration as well as the dimensionless shear modulus fields are displayed in Fig. 5.9; in particular, for each adopted laser speed, the distributions are referred to $t^* = 0.5$, Fig. 5.9(a,b), and to $t^* = 1$ Fig. 5.9(c,d). As it can be appreciated, the slowest laser speed entails a more pronounced

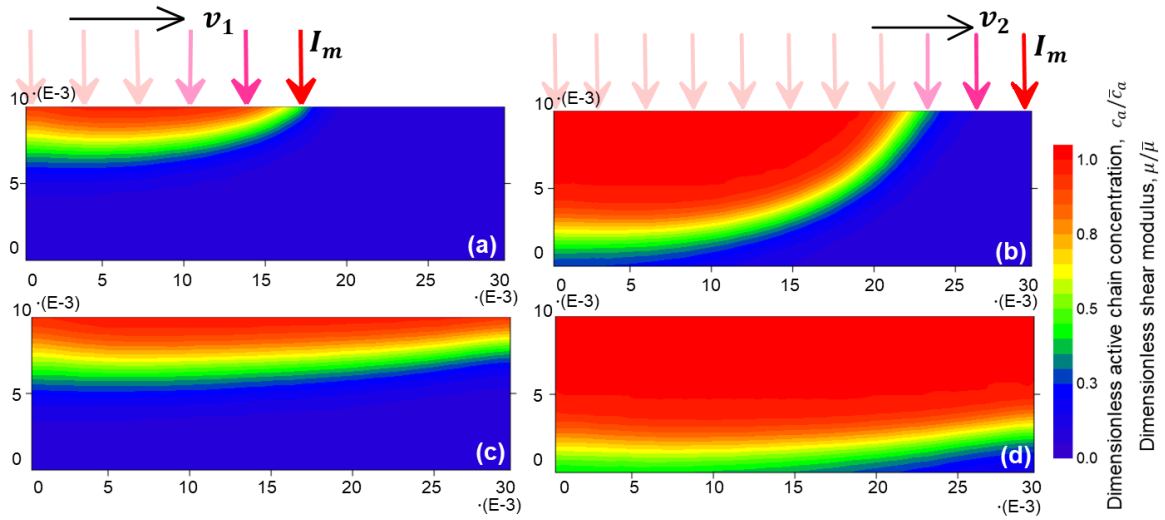

Figure 5.9: *Maps of the dimensionless shear modulus as well as of the dimensionless active chain concentrations of a liquid resin vat under photopolymerization, by assuming a constant laser light intensity* $I_m = 150\ W/m^2$ *and two different laser speed namely (a,b)* $v_1 = 1\ mm/s$ *and (c,d)* $v_2 = 0.1\ mm/s$*. The geometrical dimensions of the domain are expressed in meters.*

and homogeneous chain concentration within the domain. It can be noticed that an uncured zone ($c_a(t) \rightarrow 0$), whose extent depends on the specific laser speed used, remains at the bottom of the domain because polymer chains do not have time to propagate in that region [146].

5.5.1.2 Effect of the maximum laser light intensity

In this second parametric analysis, the effect of the maximum laser light intensity is investigated. Two photopolymerization setups are adopted for curing the domain displayed in Fig. 5.7. Two maximum laser light intensity values are considered, namely $I_{m1} = 25\ W/m^2$ and $I_{m2} = 100\ W/m^2$. The adopted laser speed is $v = 1\ mm/s$ in both cases. All the other parameters are kept fixed. The maps of the light intensity field in the domain are displayed in Fig. 5.10(A1,A2) for the two adopted values of I_m. As it can be appreciated, the use of an higher I_m enables the light to better propagate within the domain, resulting in a more evident, diffused, and deeper light-intensity within the medium, [146]. This affects the chain concentration distribution as displayed in Fig. 5.11(a) for $t^* = 0.5$. The use of a lower I_m results in a very shallow chain concentration field within the medium, see Fig. (5.11(a),A1), in comparison to the case with an higher I_m, Fig. (5.11(a),A2). This aspect can be clarified by looking at the corresponding profiles of $c_a/\bar{c}_a$ and $\mu/\bar{\mu}$ plotted vs the dimensionless vertical coordinate $\xi = (h - |Y|)/h$ (Fig. 5.11(b)), the latter graphically indicated by the vertical cross-section 1 and 2 (Fig. 5.11(a)). Similarly to the previous example, the degree of solidification (degree of conversion) achieved in the material is quantified by the dimensionless parameter $c_a/\bar{c}_a$ and $\mu/\bar{\mu}$; these fields are almost constant far away from the irradiated zone (Fig.5.11(b) at $\xi \sim > 0.5$), while a noticeable difference can be appreciated in the first top-half part of the domain being

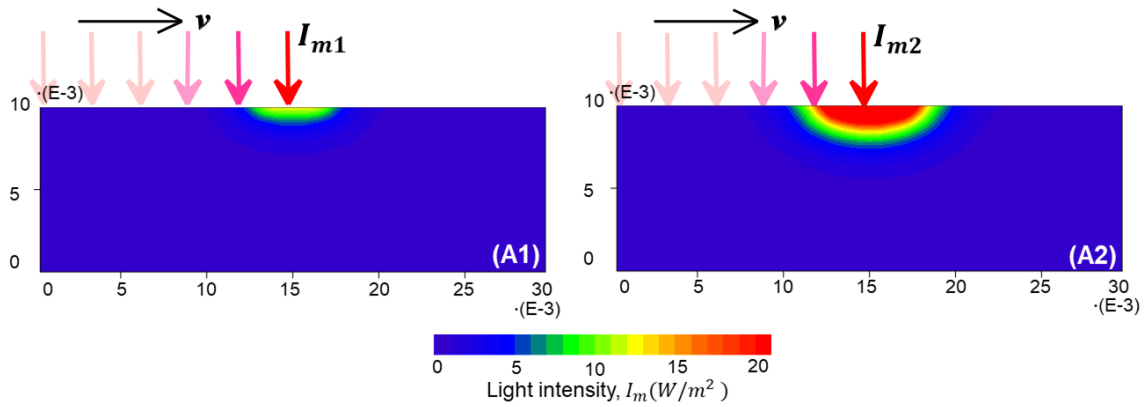

Figure 5.10: *Light intensity distribution map in a resin vat under photopolymerization for two different values of the maximum light intensity, (A1)* $I_m = 25\,W/m^2$ *and (A2)* $I_m = 100\,W/m^2$*. The geometrical dimensions of the domain are expressed in meters.*

printed. In particular, by looking at the first vertical sections, closer to the irradiated surface, the photopolymerization setup with the highest I_m provides $c_a/\overline{c}_a \to 1$ while it is much lower for the lowest I_m. On the other hand, regardless of the adopted value of I_m, $c_a/\overline{c}_a$ and $\mu/\overline{\mu}$ are always greater in section 1 rather than in section 2, because of the cross section position with respect to the speed direction.

5.5.1.3 Effect of the material's absorbance

The effect of the material's absorbance is investigated in this section. All the remaining parameters are fixed; the laser speed and the maximum laser light intensity are assumed to be $v = 1\,mm/s$ and $I_m = 150\,W/m^2$, respectively. Three cases characterized by three different values of the material's absorbance are considered: two cases with constant values $A = 600;2400\ m^{-1}$ corresponding to the liquid monomer and to the fully cured material, respectively, and the case where the material absorbance ranges between these two values according to the degree of solidification achieved, i.e. $600\,m^{-1} \le A = A(t) \le 2400\,m^{-1}$. In the latter case, the material absorbance is evaluated according to Eq. 5.11 by adopting $A_I = 30\,m^2/mol$, $A_{pol} = 2400\,m^{-1}$ and $A_{mon} = 0\,m^{-1}$.

The obtained maps of the dimensionless chain concentration, are displayed in Fig. 5.12(a). As it can be appreciated, the material with the lowest absorbance displays a more homogeneous and higher chain concentration values, Fig. 5.12(a,A1), while the material with the highest absorbance is characterized by lower values of such a quantity, Fig. 5.12(a,A3). Finally, the case characterized by a variable absorbance $600\,m^{-1} \le A = A(t) \le 2400\,m^{-1}$, displays a chain concentration's field falling in between the two previous ones, Fig. 5.12(a,A2).

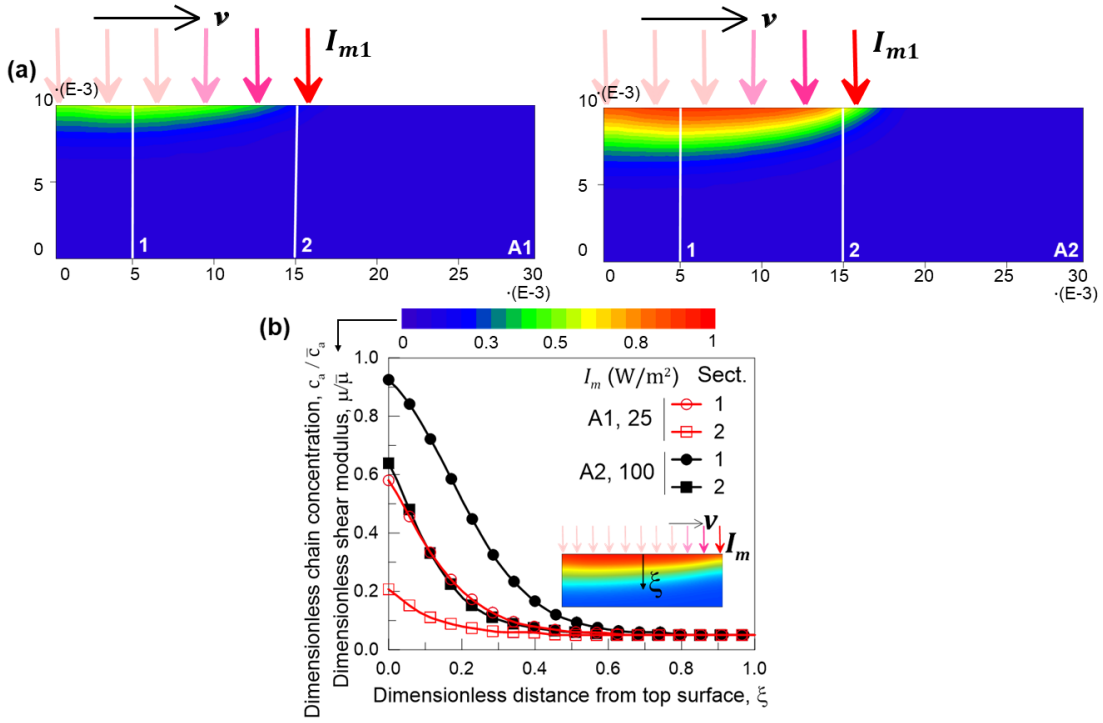

Figure 5.11: *(a) Dimensionless shear modulus as well as dimensionless chain concentration maps of a resin vat under photopolymerization, assuming a constant laser speed $v = 1\,mm/s$ and two different light intensities (A1) $I_m = 25\,W/m^2$ and (A2) $I_m = 100\,W/m^2$. The geometrical dimensions of the domain are expressed in meters. (b) Dimensionless shear modulus as well as dimensionless chain concentration vs the vertical cross-sections reported in (a), with $\xi = (h - |Y|)/h$.*

5.5.2 Programming the mechanical response of photopolymerized elements

As illustrated in sect. 5.5.1, the design of the photopolymerization setup plays a fundamental role in tuning the mechanical properties of the final synthesized material. In all the following examples, the mechanical response displayed by photopolymerized elements whose mechanical properties have been determined by the proposed model, is investigated by nonlinear FE analyses by adopting the micromechanical model proposed in sect. 5.2.3. In other words, both the two blocks of the FE code proposed in sect. 5.4 are used hereafter.

In the first example, a 2D cantilever-beam with dimensions $w\,x\,h$, under a vertical force F is considered (Fig. 5.13(a)). The element is assumed to be synthesized by exploiting the photopolymerization setup illustrated in Fig. 5.7. The concentration of the chemical specie and the rate constants listed at the beginning of sect. 5.5 have been used, with $A(\mathbf{X}, \tau) = 600\,m^{-1}$. Four photopolymerization setups characterized by the maximum laser intensity and the laser speed are considered: two setups with $I_m = 450\,W/m^2$ and by adopting (A1) $v = 0.2\,mm/s$ and (A2) $v = 1\,mm/s$, and two setups with $I_m = 100\,W/m^2$ and by assuming (A3) $v = 0.2\,mm/s$ and (A4) $v = 1\,mm/s$.

The load-displacement $(F - \delta_Y^*)$ curves of the considered structural element, represented in

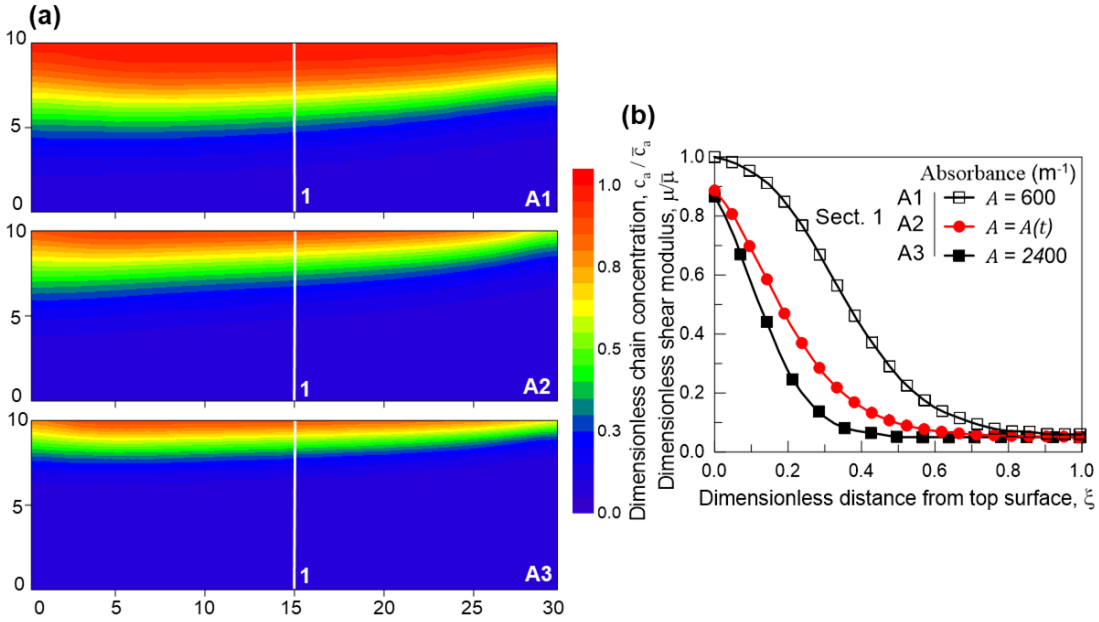

Figure 5.12: *(a) Maps of the dimensionless shear modulus as well as of the dimensionless chain concentration, by assuming a constant laser speed* $v = 1\,mm/s$ *and a constant laser light intensity* $I_m = 150\,W/m^2$*, by adopting different material's absorbances namely* $A = 600\,m^{-1}$*,* $600m^{-1} \leq A = A(t) \leq 2400\,m^{-1}$ *and* $A = 2400\,m^{-1}$*,* $A1, A2$ *and* $A3$ *respectively. Geometrical dimensions of the domain are expressed in millimeters. (b) Dimensionless shear modulus as well as dimensionless chain concentration evaluated along the vertical cross-section displayed in (a).*

Fig. 5.13 up to the load level $F = 20\,N$ (being δ_Y^* the vertical displacement of the top right point of the cantilever and $\overline{\delta}_Y^*$ the corresponding value of the fully-cured element), are illustrated by adopting the fully-cured element as the reference. It can be noticed that the mechanical response of the structural element can be tuned by controlling the photopolymerization process parameters; generally speaking, slower laser speeds (higher curing time) as well as higher maximum light intensities are responsible for a stiffer mechanical response, in comparison to higher speeds and lower light intensities. The setup with the lowest speed and the highest maximum light intensity ($A1$), provides an element whose $F - \delta_Y^*$ curve is the closest to that of the fully-cured element (A_{FC}).

By tuning the photopolymerization parameters, the vertical displacement of the reference point vs applied load can be thus programmed. For instance, the setup A_4 leads to an element whose δ_Y^* at $F = 20\,N$ is roughly 4 times $\overline{\delta}_Y^*$. The maps of the dimensionless vertical displacement, plotted in the deformed configuration for the fully-cured element and for the elements obtained with the various photopolymerization setups, are illustrated in Fig. 5.13(c) and Fig. 5.13(d).

A sensitivity study of the mechanical response of the element has been performed; different $F - \delta_Y^*$ curves arise by changing the values of the photopolymerization parameters in a controlled manner, as illustrated in Fig. 5.14, have been obtained. The $F - \delta_Y^*$ curves obtained by assuming the photopolymerization characterized by two reference laser speeds, $v = 1\,mm/s$ and $v = 0.2\,mm/s$,

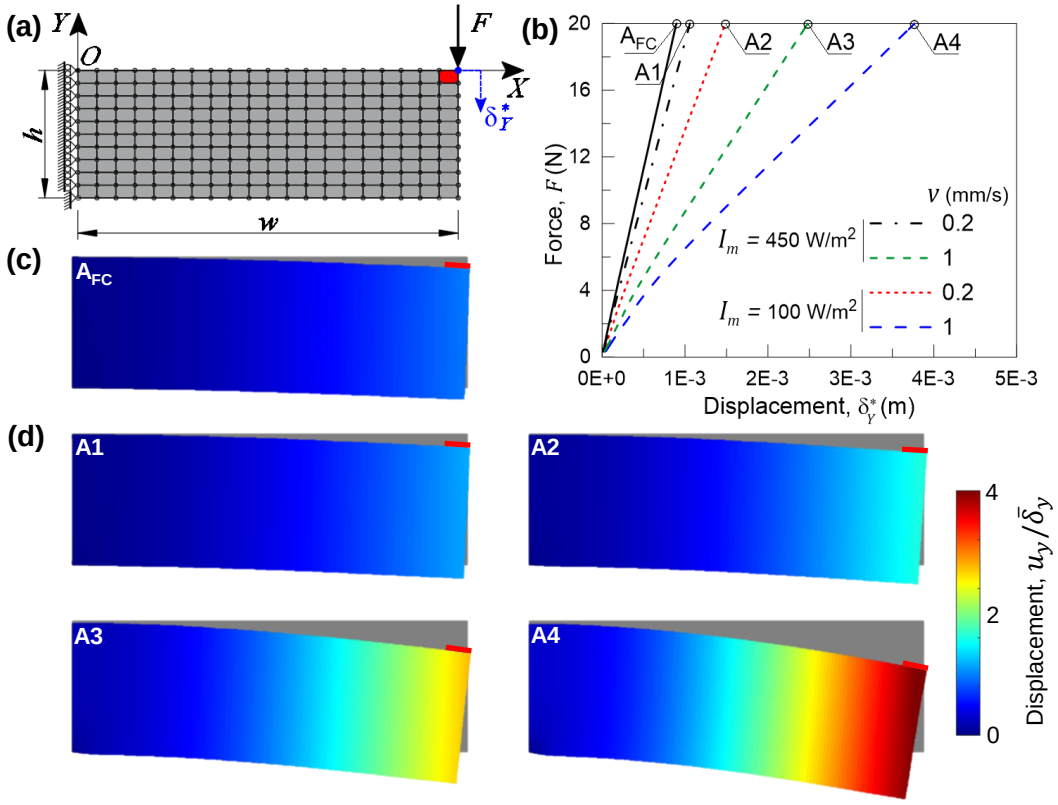

Figure 5.13: *Mechanical behavior of a photopolymerized cantilever beam, subjected to a vertical force: (a) mesh of the considered structural element, (b) load-displacement curves for the fully cured element (reference) and for elements obtained through different photopolymerization setups and corresponding maps of the vertical dimensionless displacement field (for $F = 20\,N$) for (c) the fully cured element and for (d) the different photopolymerized elements.*

respectively, and by varying the reference value of the maximum laser light intensity $I_m = 100\,W/m^2$ by ±5%, ±10% and ±50%, are shown in (Fig. 5.14(a,b)). Similarly, in Fig. 5.14(c,d), the mechanical responses obtained by assuming two reference (constant) maximum light intensities, $I_m = 100\,W/m^2$ and $I_m = 400\,W/m^2$, respectively, and by varying the reference laser speed $v = 1\,mm/s$, by ±5%, ±10% and ±50%, have been considered. Greater variations of the photopolymerization parameters (e.g. ±50%) are required to noticeably modify the mechanical response of an element. As appears from the considered example, the laser speed is more effective in providing a change of the mechanical response with respect to the maximum light intensity (see the yellow areas of Fig.5.14(a,b) and the corresponding ones of Fig.5.14(c,d)).

In the second example, the structural element assumed to be fabricated by the same photopolymerization setups ($A1 - A4$), is loaded with a tensile force F. In order to distribute the point load over the entire height of the element, a rigid bar has been introduced at its right-hand side (Fig. 5.15(a)). In this case, the horizontal displacements of the point placed at ($X = w, Y = -h/2$) of the photopolymerized elements and the corresponding one of the fully-cured element, namely δ^*_X and

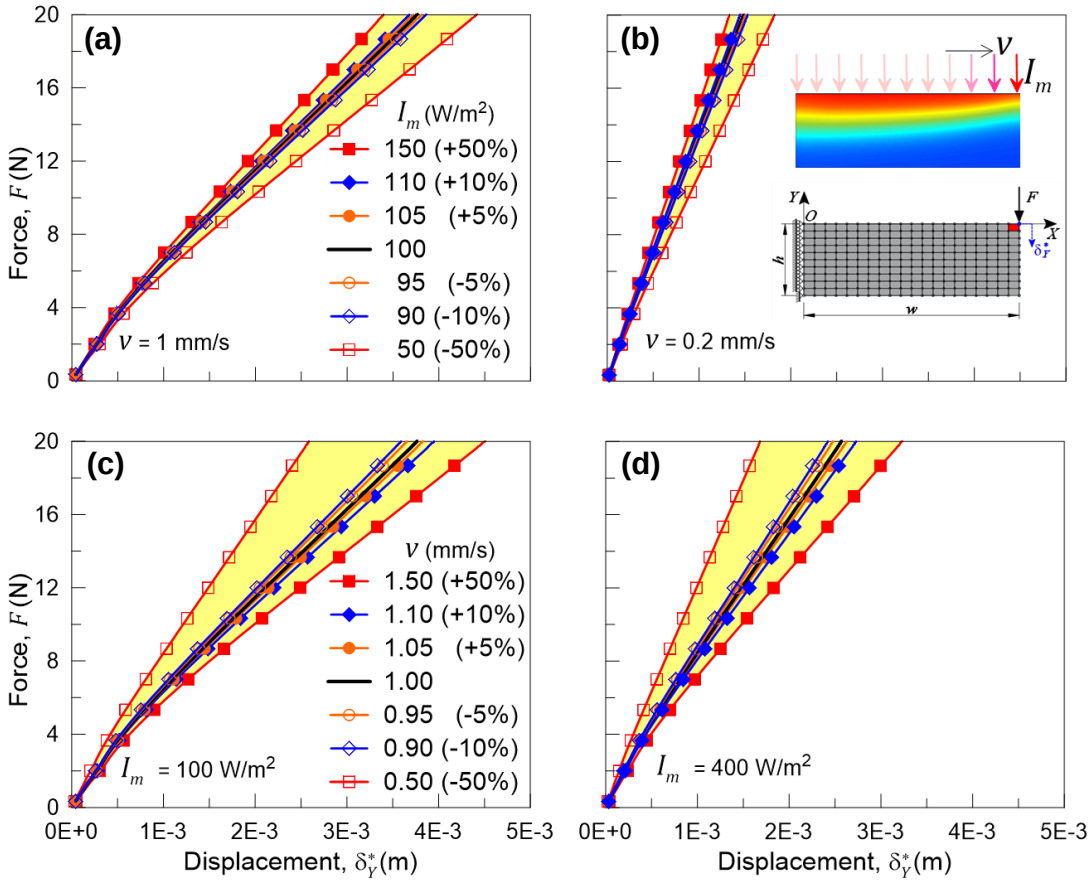

Figure 5.14: *Sensitivity analysis of the mechanical response: (a,b) $F-\delta_Y^*$ curves (up to $F=20\,N$) for an element with constant reference values of the laser speed $v=1\,mm/s$ and $v=0.2\,mm/s$, by varying the maximum light intensity. (c,d) Corresponding results obtained with fixed reference values of the maximum light intensities, $I_m=100\,W/m^2$ and $I_m=400\,W/m^2$, by controlling the laser speed.*

$\overline{\delta}_X^*$, are monitored.

The load-displacement curves ($F-\delta_X^*$) up to the load level $F=500\,N$, are shown in Fig. 5.15(b). The maps of the dimensionless horizontal displacement $u_X/\overline{\delta}_X^*$, plotted on the deformed shapes of the fully-cured element and of the actual photopolymerized one, are illustrated in Fig. 5.15(c) and Fig. 5.15(d), respectively. As it can be noticed, despite a centered tensile force is applied to the element, a bending response arises. In particular, the bending response is more pronounced by adopting the quickest laser speed and the lowest maximum light intensity, (Fig. 5.15(d), $A4$). Differently, when the lowest laser speed and the highest maximum light intensity are adopted, the mechanical properties are more homogeneously distributed over the domain and the deformed shape of the element approaches that of the fully-cured one (simple elongation with no bending). In the last example, the photopolymerization optimization problem (sect. 5.3) is considered. The goal is to find the optimum photopolymerization setup (i.e. compute $\overline{v}$ and $\overline{I}_m$) enabling the achievement of the desired mechanical response, assumed to be identified by $\delta_X^* \rightarrow \overline{\delta}_X^*$ at a given load level

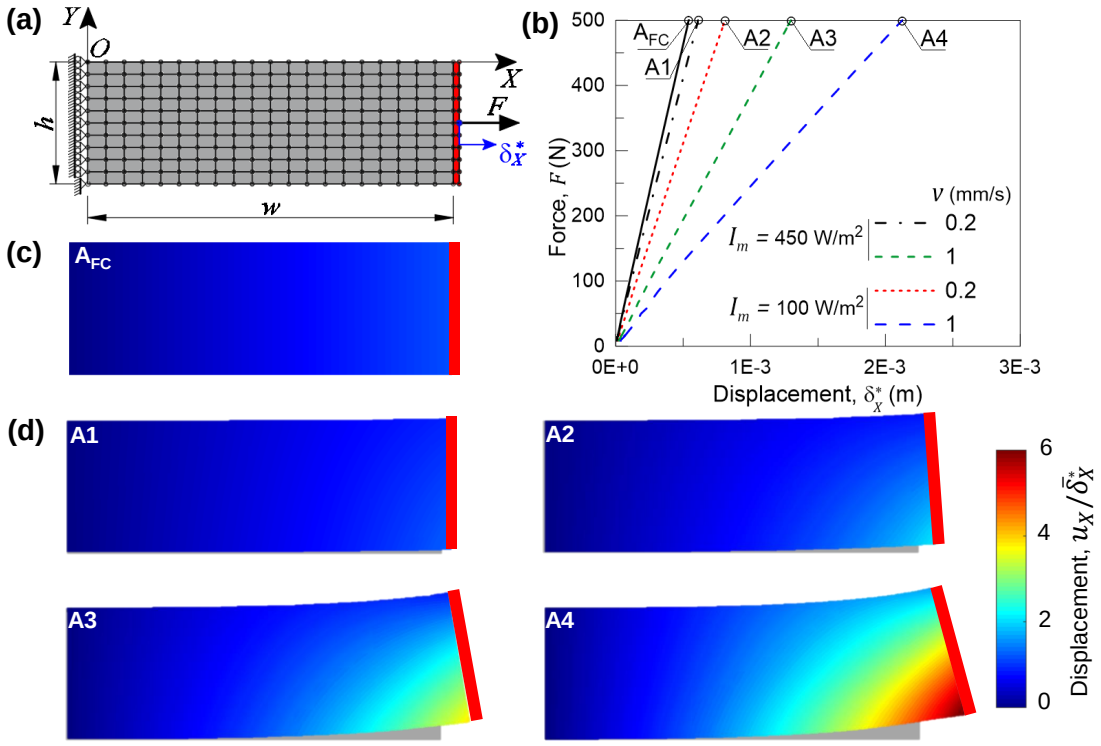

Figure 5.15: *Mechanical response of a photopolymerized element, subjected to a tensile force: (a) FE discretization, (b) load-displacement curves for the fully cured element (reference) and for elements obtained through different photopolymerization setups and corresponding maps of the horizontal dimensionless displacement field (at $F = 500\,N$) for (c) the fully cured element and for (d) different photopolymerized elements.*

$F = 500\,N$, by minimizing the energy spent in the synthesis process.

To achieve this goal, the dimensionless objective function h_{1a} (whose values range in the interval $0 \div 1$) must be minimized. The optimum values $\overline{v}$ and $\overline{I}_m$ must be searched in the design space domain, defined as follows: $v \in v_{min} \div v_{max} = 3.75 \cdot 10^{-2} \div 1\,mm/s$ and $I_m \in I_{m,min} \div I_{m,max} = 1 \div 450\,W/m^2$. For numerical reasons, the design space domain has been normalized by using dimensionless variables: $v' = \frac{v - v_{min}}{v_{max} - v_{min}}$ and $I'_m = \frac{I_m - I_{m,min}}{I_{m,max} - I_{m,min}}$, leading to $v' \in v'_{min} \div v'_{max} = 0 \div 1$ and $I'_m \in I'_{m,min} \div I'_{m,max} = 0 \div 1$.

The maps of the objective function h_{1a} for different values of the weight parameter $a = 0.2; 1; 5; 10$ are plotted in Fig. 5.16(a-d). Starting from an initial value of $h_{1a}(v', I'_m)$ (for sake of simplicity placed at the center of the design domain), the optimal solution $(\overline{v}', \overline{I}'_m)$ is obtained by adopting the iterative procedure briefly illustrated in sect. 5.3; the solution evolves following the white paths in Fig. 5.16), until the minimum of h_{1a} is achieved.

The maps of the dimensionless chain concentration for two elements obtained via photopolymerization by adopting the optimum values of $\overline{v}'$ and $\overline{I}'_m$, whose values correspond to those obtained by the minimization problem with $a = 1$ and $a = 10$, are plotted in Fig. 5.17(a,b). The resulting chain concentration field is almost homogeneous if $a = 1$ is adopted, with $c_a/\overline{c}_a \to 1$ roughly in the entire

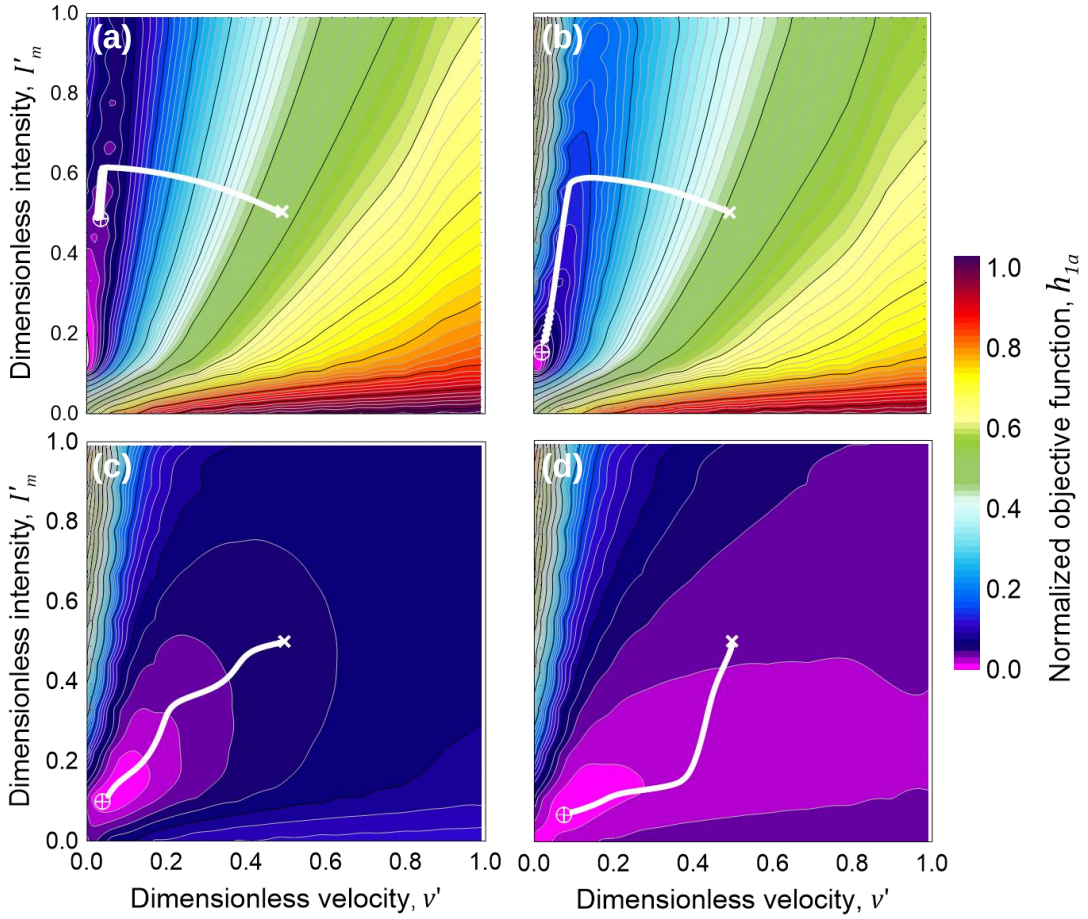

Figure 5.16: *Maps of the objective function h_{1a} for different values of the weight parameter a, namely $a = 0.2; 1; 5; 10$ (a,b,c,d). The line search path of the iterative solution (Newton directions) is displayed by the white line; the solution evolves from the center of the design space until the desired optimum condition is attained.*

domain, while a non-symmetric distribution with different values of $c_a/\overline{c}_a$ arises by adopting $a = 10$. The corresponding mechanical responses are plotted in Fig. 5.17(c,d). As it can be noticed, the lowest value of the weight parameter a makes the compliance of the element to reach a minimum, resulting in a mechanical behavior close to that of the fully-cured element (simple elongation); on the other hand, the highest a results in a photopolymerization setup which provides an element whose mechanical behavior for the same load level displays a non-symmetric deformed shape.

In conclusion, a multi-physics model suitable for describing the mechanical response of materials obtained through photopolymerization has been formulated and its numerical implementation in a FE framework has been illustrated. In particular, the model describes mathematically the light diffusion phenomenon, the polymer chains formation as well as the mechanics of the final synthesized material (*process-microstructure-responsiveness* relationship). The model has been

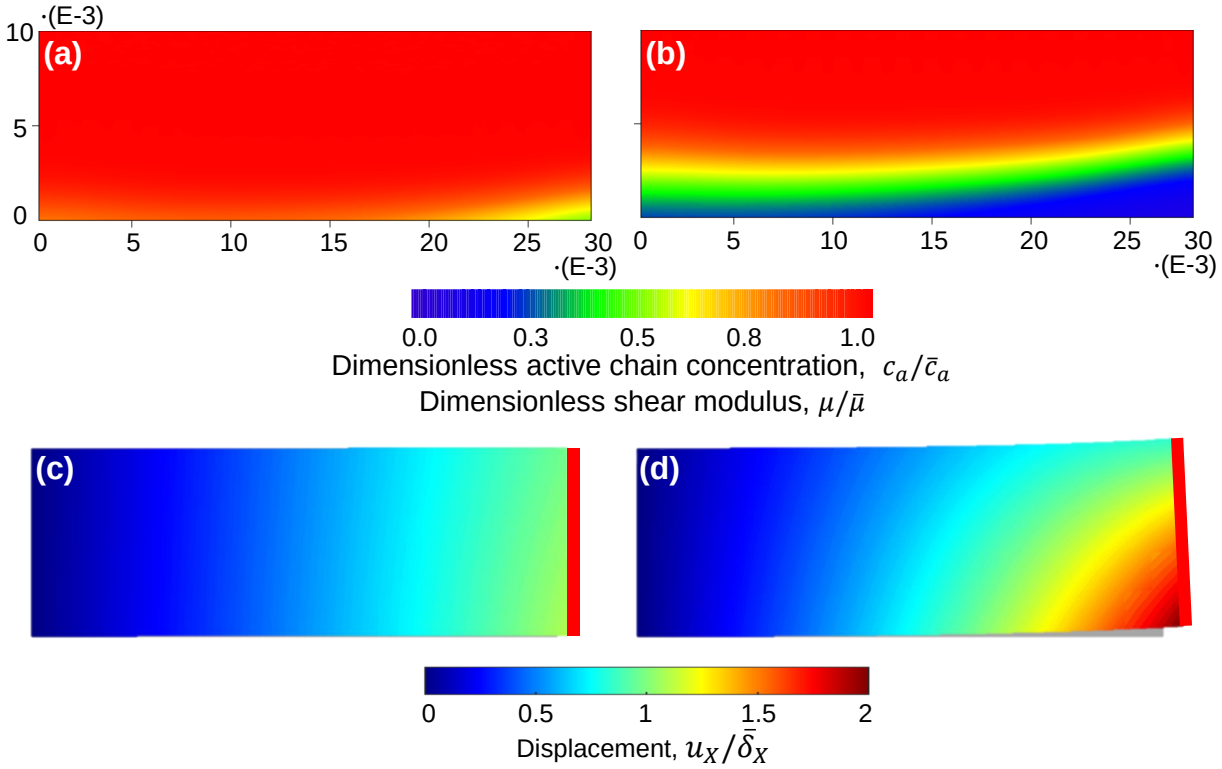

Figure 5.17: *Maps of the dimensionless chain concentration obtained by the photopolymerization of the domain vat with the optimum values* $\overline{v}$ *and* $\overline{I}_m$*, evaluated by solving the minimization problem with (a)*$a = 1$ *and (b)* $a = 10$*. Dimensions in* $[m]$*. (c,d) Corresponding mechanical response of the two optimum photopolymerized elements; the dimensionless horizontal displacement field (evaluated at* $F = 500\,N$*) is plotted in the deformed shape.*

validated by the simulation of a real photopolymerization case. It has been shown how the main photopolymerization process parameters (such as the laser speed and the maximum laser light intensity) affect the mechanical properties of photopolymerized structural elements. It has been illustrated how synthesizing an element by using different photopolymerization setups entails quite different mechanical responses, enabling the possibility of programming the mechanical response of polymer-based elements. The optimization problem, suitable for defining the optimum photopolymerization setup required to synthesize a polymer-based element having a prescribed mechanical response, has been also addressed. The outcome of the present work represents an insight that may open new scenarios in the design and development of innovative functional materials obtained by controlling the material's microstructure via photopolymerization.

CHAPTER 6

CONCLUSIONS AND FUTURE PERSPECTIVES

In the present work, the mechanical response of innovative functional materials has been considered by following the *process-microstructure-responsiveness* concept. From a general viewpoint, it can be concluded that controlling the synthesis process allows inferring a desired microstructure to the material, enabling the final goal of obtaining a responsive material with a programmed functionality. This is a well-known feature of natural structures (naturally-programmed) and it can nowadays be exploited in the context of synthetic functional materials, thanks to innovative synthesis processes (such as 3D printing).

The development of physics-based models capable to relate the microstructure of a functional material to its responsiveness, useful for programming and controlling the mechanical response of innovative materials in the perspective of a functional design, has been considered. This is an important route to pursue in order to support the development of functional materials required by specific applications [155], or, to some extent, for supporting the synthesis of materials-like-machines as visionarily discussed in [80, 156]; this class of materials is characterized by a microstructure whose properties allow obtaining functionalities similar to those shown by everyday machines, but without any need of engine, hydraulic systems, sensors, etc., for their tasks to be done. Furthermore, the development of functional materials that can adapt their responsiveness during their life-cycle (reconfiguration), represents a challenge to be addressed in future research; the physics-based models presented in this work, as well as the general methodology adopted and the acquired mindset, represent an important starting point to be used in perspective studies in this field.

Within the context outlined above, a physics-based model aimed at mathematically describing the shape-morphing capability of thermally-responsive LCE materials and a multi-physics model for describing the mechanical behaviour of polymers obtained *via* photopolymerization, have been proposed.

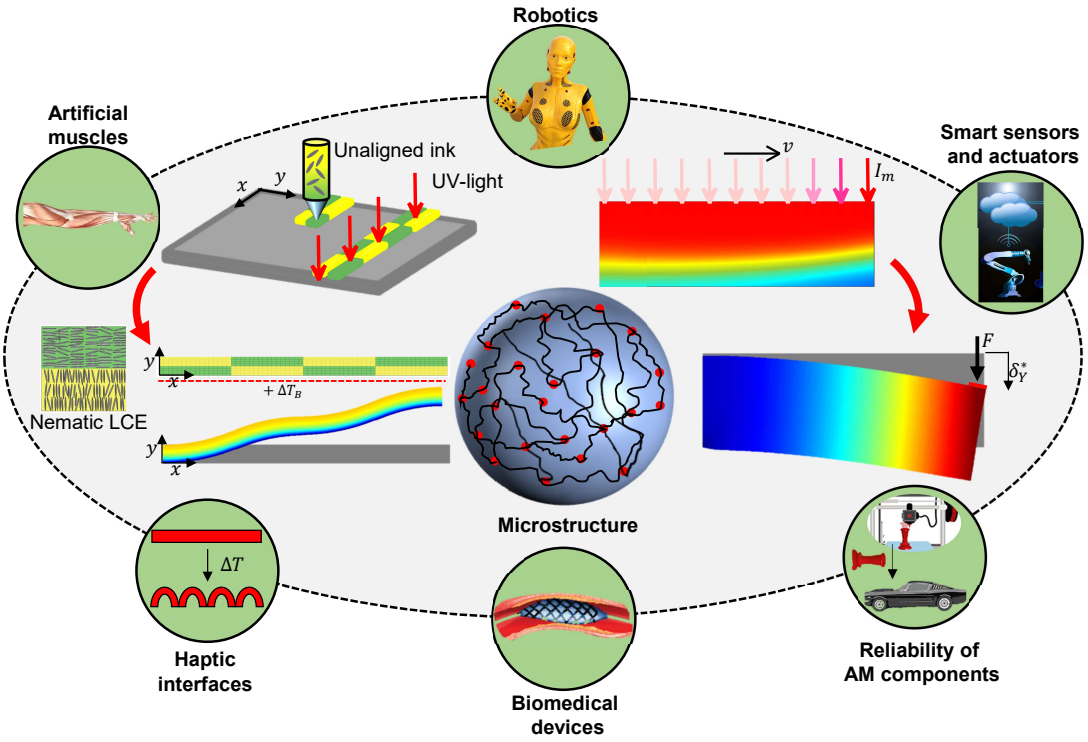

Figure 6.1: *Summary of the process-microstructure-responsiveness relationship with particular reference to the topics treated in the present work (grey region) and some applications (green regions).*

The present study, dealing with the mechanics of thermally-responsive LCEs based on a theoretical micromechanical based framework, represents a novelty in the current literature [25]. It is worth highlighting also the introduction of a theoretical description of the cross-link density-controlled actuation of LCEs; so far, this latter aspect has been investigated mainly through experiments in the current literature and the introduction of a proper modeling tool [127] represents an important contribution.

It has been demonstrated how micromechanical features of a LCE material can be tuned to control and program its mechanical response in order to get the desired shape-morphing response. Different shape-morphing responses, ranging from simple contractions/elongations to intricate bending responses, have been encoded in the material as shown by several examples.

According to the model presented in chapter 4, the features offered by the microstructure of LCE materials (although related to their synthesis process) do not directly stem from the synthesis process used, and have been assumed *a priori*. The design of the LCE synthesis, based on proper modeling approaches, has to be addressed in future studies, for instance by modeling the filament-by-filament deposition of LCE ink (involved for example in the DIW technique) and its successive photopolymerization. This approach will enable to understand and encode new intriguing features and morphing capabilities in LCE-based devices. This aspect has emerged from recent experimental

studies [157] where process parameters have been shown to be related to the morphing capabilities of LCEs. Experimental studies have also shown the possibility to fabricate LCE elements with an arbitrary three-dimensional nematic director distribution non necessarily related to a prefixed printing path, to get exotic 3D shape-morphing [158]. The implementation of the presented model in a 3D FE framework may represent a further extension to face new scenarios. The present model is a prominent candidate to be used in future studies as a tool for building a large input/output simulation data set to be used, for instance, for training a neural network (Machine Learning), aimed at automatically providing the material's microstructure architecture according to the response required (inverse problem).

In the present study, the *process-microstructure-responsiveness* inspiration concept has been also exploited to program the mechanical response of photopolymerized materials (chapter 5). The proposed approach, based on a chemical-physics description of the photopolymerization process coupled with a micromechanical model of the final photopolymerized material, represents a further contribution to the existing literature [145, 146, 150].

It has been demonstrated the possibility of obtaining different load-displacement responses and deformed shapes of a structural element, by tuning its photopolymerization process setup.

In the presented examples, elements have been assumed to be photopolymerized in one single layer; in future studies, the photopolymerization of an element made of many superposed layers, though conceptually no differences exist with respect to the case of a single layer, will be considered. This aspect may allow us to assess the effect of the layer thickness on the mechanical response of a photopolymerized element, thus enabling to enlarge the degrees of freedom of the design space and open new scenarios in the perspective of their functional design.

The optimization problem addressed in this work has allowed to obtain target mechanical responses under assigned mechanical actions, by minimizing the energy spent for the photopolymerization process. Future studies may consider the possibility of exploiting the photopolymerization for synthesizing elements displaying a load-displacement target curve (with a pre-defined arbitrary path), as shown for instance in [69] for composite metastructures. In such a context, approaches based on Machine Learning could be the right tool to obtain unprecedented functional materials.

APPENDIX

A.1 Energy of a nematic elastomer

The main difference between nematic elastomers and regular elastomers is related to the molecular anistropy induced by the nematic mesogens. Therefore, from an energetic viewpoint, the mechanical description of a nematic elastomers is basically an extension of the classical molecular rubber elasticity. In particular, according to [109], the free energy per unit volume of the material can be obtained by adding up the free energy of all the chains contained in a reference volume, embedded in the chain configuration space, i.e.:

$$\Psi = -c_a k_B T \left\langle ln\varphi_n \right\rangle = \frac{3c_a k_B T}{2Nb} tr\left(\ell^{-1} \left\langle \boldsymbol{r} \otimes \boldsymbol{r} \right\rangle\right) + C \tag{A.1.1}$$

where the non-isotropic distribution function φ_n given by Eq. 4.1 has been used, while C is a constant that can be neglected when change of nematic directors is considered. By using the affine deformation hypothesis, the current end-to-end vector can be simply expressed as $\boldsymbol{r} = \boldsymbol{F}\boldsymbol{r}_0$ and the free energy (Eq. A.1.1) becomes [111]:

$$\Psi = \frac{1}{2} c_a k_B T \, \mathrm{tr}(\mathbf{F}\boldsymbol{\ell}_0\mathbf{F}^T\boldsymbol{\ell}^{-1}) \tag{A.1.2}$$

which has been written by assuming the nematic state exists in the initial (reference) state and exploiting the result $\left\langle \mathbf{r}_{0i}\mathbf{r}_{0j} \right\rangle = \frac{Nb}{3}\boldsymbol{\ell}_{0ij}$. On the other hand, the variation of the energy density with respect to the nematic stress-free state, for which $\Psi_0 = 3\mu/2$, can now be expressed as:

$$\Delta\Psi(t) = \Psi(t) - \Psi_0 = \frac{\mu}{2}\left[\mathrm{tr}\left(\mathbf{F}\boldsymbol{\ell}_0\mathbf{F}^T\boldsymbol{\ell}^{-1}\right) - 3\right] \tag{A.1.3}$$

where $\mu = c_a k_B T$ is the shear modulus of the material.

On the other hand, the free energy can be rewritten by means of the chain distribution tensor but taking into account the nematic character of the polymer network. The initial nematic stress-free state can be rewritten by considering that $\mathrm{tr}\,\boldsymbol{\mu}_{0n} = \frac{Nb}{3}\mathrm{tr}\boldsymbol{\ell}_0 = 3\frac{Nb^2}{3}$. Therefore, the following expression can be obtained:

$$\begin{aligned} \Delta\Psi(t) = \Psi(t) - \Psi_0 &= \frac{3\mu}{2Nb^2}\mathrm{tr}\left(\boldsymbol{\mu}_n(t) - \boldsymbol{\mu}_{0n}\right) \\ &= \frac{\mu}{2}\left(\mathrm{tr}\frac{3\boldsymbol{\mu}_n(t)}{Nb^2} - 3\right) \end{aligned} \tag{A.1.4}$$

where $\boldsymbol{\mu}_{on} = \boldsymbol{\mu}_n(t=0)$, which represents the extension of the free energy typically defined in the classical rubber elasticity theory, [25]. From the above equation, the relationship between the chain distribution tensor in the current configuration and the initial step length tensor, can be obtained:

$$\boldsymbol{\mu}_n = \frac{Nb}{3}\boldsymbol{F}\boldsymbol{\ell}_0\boldsymbol{F}^T \tag{A.1.5}$$

A.2 Mechanics of elastomers with multiple networks

The extension of the distribution tensor concept to elastomers with multiple networks is briefly presented. It is worth recalling that the concept of multiple networks has been used in chapter 4 only for assessing the chain distribution tensor evolution, by taking into account the actual deformation effectiveness on the controlled morphing of LCEs related to the cross-link density influence (see Sect. 4.3.2).

Let's assume that a polymeric material is made of $I = 1,...,M$ non-interacting entangled networks, each one characterized by its own cross-link density c_I and by other physical properties such as the average number of Kuhn's segment per chain (N_I), the length of each Kuhn's segments belonging to such a I-th network (b_I) etc. Under these conditions, in the stress-free state the network is described by M distribution functions φ_{0I} each one providing the statistical distribution of a single network. The initial distribution tensor of the I-th network, can be defined as:

$$\boldsymbol{\mu}_I(\mathbf{r}, t=0) = \boldsymbol{\mu}_{0I}(\mathbf{r}) = \langle \varphi_{0I}(\mathbf{r})\mathbf{r}\otimes\mathbf{r}\rangle \tag{A.2.1}$$

whose evolution due to mechanical deformation is expressed as:

$$\dot{\boldsymbol{\mu}}_{\mathbf{F}I}(t) = \mathbf{L}\boldsymbol{\mu}_{\mathbf{F}I}(t) + \left(\mathbf{L}\boldsymbol{\mu}_{\mathbf{F}I}(t)\right)^T \tag{A.2.2}$$

By representing the total cross-link density of the entire network through the sum of the cross-link density of each sub-network, i.e. $c_a = \sum_{I=1}^{M} c_{aI}$, the overall distribution tensor of the multiple network can be evaluated by means of the following equation:

$$\boldsymbol{\mu}(t) = \sum_{I=1}^{M} \frac{c_{aI}}{c_a}\boldsymbol{\mu}_I(t) \tag{A.2.3}$$

On the other hand, by assuming that the mass density of the polymer does not depend on the chain's cross-link density, it holds $v_{fI} = v_I/v = c_{aI}/c_a$ [127]. Moreover, by assuming that all the networks constituting the polymer are chemically identical and assuming that they do not interact each other, the elastic energy density stored in the material can be additively decomposed as:

$$\begin{aligned}\Delta\Psi &= \frac{3k_BT}{2Nb^2}\sum_{I=1}^{M} c_{aI}\,tr(\boldsymbol{\mu}_I - \boldsymbol{\mu}_{0I}) + \pi[det\boldsymbol{F} - 1] = \\ &= \frac{3c_ak_BT}{2Nb^2}\sum_{I=1}^{M} v_{fI}\,tr(\boldsymbol{\mu}_I - \boldsymbol{\mu}_{0I}) + \pi[det\boldsymbol{F} - 1]\end{aligned} \tag{A.2.4}$$

which is formally equivalent to Eq. A.1.4.

BIBLIOGRAPHY

[1] M. Nagalakshmaiah, S. Afrin, R. P. Malladi, S. Elkoun, M. Robert, M. A. Ansari, A. Svedberg, and Z. Karim, "Chapter 9 - Biocomposites: Present trends and challenges for the future," in *Green Composites for Automotive Applications*, ser. Woodhead Publishing Series in Composites Science and Engineering, G. Koronis and A. Silva, Eds. Woodhead Publishing, 2019, pp. 197–215. [Online]. Available: https://www.sciencedirect.com/science/article/pii/B9780081021774000094

[2] M. Doi, *Soft matter physics*. Oxford University Press, 2013.

[3] P. J. Flory, *Principles of polymer chemistry*. Cornell University Press, 1953.

[4] C. A. R. A. J. Peacock, "Polymer chemistry : properties and applications," 2006, archive: /z-wcorg/ ISBN: 9781613443002 1613443005 9783446433434 3446433430 Library Catalog: http://worldcat.org Place: Munich; Cincinnati, Ohio Publisher: Hanser Gardner Publications. [Online]. Available: http://search.ebscohost.com/login.aspx?direct=true&scope=site&db=nlebk&db=nlabk&AN=1628275

[5] J. R. Fried, "Polymer science and technology," 2014, archive: /z-wcorg/ ISBN: 9780137039975 0137039972 9780137039555 0137039557 Library Catalog: http://worldcat.org Place: Upper Saddle River, NJ Publisher: Prentice Hall.

[6] L. Treloar, *The physics of rubber elasticity*. Oxford University Press, USA, 1975.

[7] G. Puglisi and G. Saccomandi, "Multi-scale modelling of rubber-like materials and soft tissues: *an appraisal*," *Proceedings of the Royal Society A: Mathematical, Physical and Engineering Sciences*, vol. 472, no. 2187, p. 20160060, 2016, _eprint: https://royalsocietypublishing.org/doi/pdf/10.1098/rspa.2016.0060. [Online]. Available: https://royalsocietypublishing.org/doi/abs/10.1098/rspa.2016.0060

[8] G. Holzapfel, *Nonlinear Solid Mechanics: A Continuum Approach for Engineering*. West Sussex, England: John Wiley & Sons, Ltd, 2000.

[9] O. Yeoh, "Some forms of the strain energy function for rubber," *Rubber Chemistry and technology*, vol. 66, no. 5, pp. 754–771, 1993.

[10] L. R. G. Treloar, "The elasticity of a network of long-chain molecules.—III," *Trans. Faraday Soc.*, vol. 42, no. 0, pp. 83–94, 1946, publisher: The Royal Society of Chemistry. [Online]. Available: http://dx.doi.org/10.1039/TF9464200083

[11] M. Boyce and E. Arruda, "Constitutive models of rubber elasticity: a review," *Rubber chemistry and technology*, vol. 73, no. 3, pp. 504–523, 2000.

[12] P. J. Flory, M. Gordon, P. J. Flory, and N. . G. McCrum, "Statistical thermodynamics of random networks," *Proceedings of the Royal Society of London. A. Mathematical and Physical Sciences*, vol. 351, no. 1666, pp. 351–380, Nov. 1976, publisher: Royal Society. [Online]. Available: https://doi.org/10.1098/rspa.1976.0146

[13] P. Wu and E. Van Der Giessen, "On improved network models for rubber elasticity and their applications to orientation hardening in glassy polymers," *Journal of the Mechanics and Physics of Solids*, vol. 41, no. 3, pp. 427–456, 1993, publisher: Elsevier.

[14] R. Brighenti and M. P. Cosma, "Swelling mechanism in smart polymers responsive to mechano-chemical stimuli," *Journal of the Mechanics and Physics of Solids*, vol. 143, p. 104011, Oct. 2020, publisher: Elsevier Ltd.

[15] Y. Mao, B. Talamini, and L. Anand, "Rupture of polymers by chain scission," *Extreme Mechanics Letters*, vol. 13, pp. 17–24, 2017, publisher: Elsevier.

[16] M. Wang and E. Guth, "Statistical theory of networks of non-Gaussian flexible chains," *The Journal of Chemical Physics*, vol. 20, no. 7, pp. 1144–1157, 1952, publisher: AIP.

[17] P. J. Flory and J. Rehner, "Statistical Mechanics of Cross-Linked Polymer Networks I. Rubberlike Elasticity," *The Journal of Chemical Physics*, vol. 11, no. 11, pp. 512–520, Nov. 1943, publisher: American Institute of Physics. [Online]. Available: https://doi.org/10.1063/1.1723791

[18] E. M. Arruda and M. C. Boyce, "A three-dimensional constitutive model for the large stretch behavior of rubber elastic materials," *Journal of the Mechanics and Physics of Solids*, vol. 41, no. 2, pp. 389–412, Feb. 1993.

[19] F. J. Vernerey, R. Long, and R. Brighenti, "A statistically-based continuum theory for polymers with transient networks," *Journal of the Mechanics and Physics of Solids*, vol. 107, pp. 1 – 20, 2017. [Online]. Available: http://www.sciencedirect.com/science/article/pii/S0022509617301874

[20] M. Beatty, "An average-stretch full-network model for rubber elasticity," *Journal of Elasticity*, vol. 70, no. 1-3, pp. 65–86, 2003, publisher: Springer.

[21] H. James and E. Guth, "Theory of the elastic properties of rubber," *The Journal of Chemical Physics*, vol. 11, no. 10, pp. 455–481, 1943, publisher: AIP.

[22] R. Brighenti, F. Artoni, and M. P. Cosma, "Viscous and Failure Mechanisms in Polymer Networks: A Theoretical Micromechanical Approach," *Materials*, vol. 12, no. 10, p. 1576, 2019.

[23] A. Spagnoli, R. Brighenti, M. P. Cosma, and M. Terzano, "Fracture in soft elastic materials: Continuum description, molecular aspects and applications," ser. Advances in Applied Mechanics. Elsevier, 2021, iSSN: 0065-2156. [Online]. Available: https://www.sciencedirect.com/science/article/pii/S0065215621000028

[24] R. Brighenti, Y. Li, and F. J. Vernerey, "Smart polymers for advanced applications: a mechanical perspective review," *Frontiers in Materials*, vol. 7, p. 196, 2020. [Online]. Available: https://www.frontiersin.org/article/10.3389/fmats.2020.00196

[25] R. Brighenti, C. G. McMahan, M. P. Cosma, A. Kotikian, J. A. Lewis, and C. Daraio, "A micromechanical-based model of stimulus responsive liquid crystal elastomers," *International Journal of Solids and Structures*, vol. 219-220, pp. 92–105, 2021. [Online]. Available: https://www.sciencedirect.com/science/article/pii/S0020768321000779

[26] F. Vernerey, R. Brighenti, R. Long, and T. Shen, "Statistical Damage Mechanics of Polymer Networks," *Macromolecules*, vol. 51, no. 17, pp. 6609–6622, 2018, publisher: ACS Publications.

[27] L. K. Rivera-Tarazona, V. D. Bhat, H. Kim, Z. T. Campbell, and T. H. Ware, "Shape-morphing living composites," *Science Advances*, vol. 6, no. 3, 2020, publisher: American Association for the Advancement of Science _eprint: https://advances.sciencemag.org/content/6/3/eaax8582.full.pdf. [Online]. Available: https://advances.sciencemag.org/content/6/3/eaax8582

[28] P. C. Foster, N. J. Mlot, A. Lin, and D. L. Hu, "Fire ants actively control spacing and orientation within self-assemblages," *Journal of Experimental Biology*, vol. 217, no. 12, pp. 2089–2100, Jun. 2014. [Online]. Available: https://doi.org/10.1242/jeb.093021

[29] A. Barbosa, J. J. Allen, L. M. Mäthger, and R. T. Hanlon, "Cuttlefish use visual cues to determine arm postures for camouflage," *Proceedings. Biological sciences*, vol. 279, no. 1726, pp. 84–90, Jan. 2012, edition: 2011/05/11 Publisher: The Royal Society. [Online]. Available: https://pubmed.ncbi.nlm.nih.gov/21561967

[30] S. Poppinga, C. Zollfrank, O. Prucker, J. Rühe, A. Menges, T. Cheng, and T. Speck, "Toward a New Generation of Smart Biomimetic Actuators for Architecture," *Advanced Materials*, vol. 30, no. 19, p. 1703653, 2018, _eprint:

https://onlinelibrary.wiley.com/doi/pdf/10.1002/adma.201703653. [Online]. Available: https://onlinelibrary.wiley.com/doi/abs/10.1002/adma.201703653

[31] F. Vollrath, "Strength and structure of spiders' silks," *Reviews in Molecular Biotechnology*, vol. 74, no. 2, pp. 67–83, 2000. [Online]. Available: https://www.sciencedirect.com/science/article/pii/S1389035200000064

[32] M. Serpelloni, M. Arricca, C. Bonanno, and A. Salvadori, "Modeling cells spreading, motility, and receptors dynamics: a general framework," *Acta Mechanica Sinica*, vol. 37, no. 6, pp. 1013–1030, Jun. 2021. [Online]. Available: https://doi.org/10.1007/s10409-021-01088-w

[33] V. Damioli, A. Salvadori, G. P. Beretta, C. Ravelli, and S. Mitola, "Multi-physics interactions drive VEGFR2 relocation on endothelial cells," *Scientific Reports*, vol. 7, no. 1, p. 16700, Dec. 2017. [Online]. Available: https://doi.org/10.1038/s41598-017-16786-4

[34] P. Christen, K. Ito, R. Ellouz, S. Boutroy, E. Sornay-Rendu, R. D. Chapurlat, and B. van Rietbergen, "Bone remodelling in humans is load-driven but not lazy," *Nature Communications*, vol. 5, no. 1, p. 4855, Sep. 2014. [Online]. Available: https://doi.org/10.1038/ncomms5855

[35] Z. Wang, J. Wang, J. Ayarza, T. Steeves, Z. Hu, S. Manna, and A. P. Esser-Kahn, "Bio-inspired mechanically adaptive materials through vibration-induced crosslinking," *Nature Materials*, vol. 20, no. 6, pp. 869–874, Jun. 2021. [Online]. Available: https://doi.org/10.1038/s41563-021-00932-5

[36] I. Linsmeier, S. Banerjee, P. W. Oakes, W. Jung, T. Kim, and M. P. Murrell, "Disordered actomyosin networks are sufficient to produce cooperative and telescopic contractility," *Nature Communications*, vol. 7, no. 1, p. 12615, Aug. 2016. [Online]. Available: https://doi.org/10.1038/ncomms12615

[37] M. Schuppler, F. C. Keber, M. Kröger, and A. R. Bausch, "Boundaries steer the contraction of active gels," *Nature Communications*, vol. 7, no. 1, p. 13120, Oct. 2016. [Online]. Available: https://doi.org/10.1038/ncomms13120

[38] T. D. Ross, H. J. Lee, Z. Qu, R. A. Banks, R. Phillips, and M. Thomson, "Controlling organization and forces in active matter through optically defined boundaries," *Nature*, vol. 572, no. 7768, pp. 224–229, Aug. 2019. [Online]. Available: https://doi.org/10.1038/s41586-019-1447-1

[39] T. Nitta, Y. Wang, Z. Du, K. Morishima, and Y. Hiratsuka, "A printable active network actuator built from an engineered biomolecular motor," *Nature Materials*, Apr. 2021. [Online]. Available: https://doi.org/10.1038/s41563-021-00969-6

[40] E. Méhes and T. Vicsek, "Collective motion of cells: from experiments to models." *Integrative biology : quantitative biosciences from nano to macro*, vol. 6, no. 9, pp. 831–854, Sep. 2014, place: England.

[41] O. Peleg, J. M. Peters, M. K. Salcedo, and L. Mahadevan, "Collective mechanical adaptation of honeybee swarms," *Nature Physics*, vol. 14, no. 12, pp. 1193–1198, Dec. 2018. [Online]. Available: https://doi.org/10.1038/s41567-018-0262-1

[42] F. J. Vernerey, E. Benet, L. Blue, A. K. Fajrial, S. L. Sridhar, J. S. Lum, G. Shakya, K. H. Song, A. N. Thomas, and M. A. Borden, "Biological active matter aggregates: Inspiration for smart colloidal materials," *Advances in Colloid and Interface Science*, vol. 263, pp. 38 – 51, 2019. [Online]. Available: http://www.sciencedirect.com/science/article/pii/S0001868618302549

[43] D. Hu, S. Phonekeo, E. Altshuler, and F. Brochard-Wyart, "Entangled active matter: From cells to ants," *The European Physical Journal Special Topics*, vol. 225, no. 4, pp. 629–649, Jul. 2016. [Online]. Available: https://doi.org/10.1140/epjst/e2015-50264-4

[44] E. D. Brodie, "Salamander Antipredator Postures," *Copeia*, vol. 1977, no. 3, pp. 523–535, 1977, publisher: [American Society of Ichthyologists and Herpetologists (ASIH), Allen Press]. [Online]. Available: http://www.jstor.org/stable/1443271

[45] H. Shahsavan, S. M. Salili, A. Jákli, and B. Zhao, "Thermally Active Liquid Crystal Network Gripper Mimicking the Self-Peeling of Gecko Toe Pads," *Advanced Materials*, vol. 29, no. 3, p. 1604021, 2017, _eprint: https://onlinelibrary.wiley.com/doi/pdf/10.1002/adma.201604021. [Online]. Available: https://onlinelibrary.wiley.com/doi/abs/10.1002/adma.201604021

[46] S. Sponberg, "The emergent physics of animal locomotion," *Physics Today*, vol. 70, no. 9, pp. 34–40, Sep. 2017, publisher: American Institute of Physics. [Online]. Available: https://doi.org/10.1063/PT.3.3691

[47] S. A. Combes and R. Dudley, "Turbulence-driven instabilities limit insect flight performance," *Proceedings of the National Academy of Sciences*, vol. 106, no. 22, pp. 9105–9108, 2009, publisher: National Academy of Sciences _eprint: https://www.pnas.org/content/106/22/9105.full.pdf. [Online]. Available: https://www.pnas.org/content/106/22/9105

[48] T. Engels, D. Kolomenskiy, K. Schneider, M. Farge, F.-O. Lehmann, and J. Sesterhenn, "Impact of turbulence on flying insects in tethered and free flight: High-resolution numerical experiments," *Phys. Rev. Fluids*, vol. 4, no. 1, p. 013103, Jan. 2019, publisher: American Physical Society. [Online]. Available: https://link.aps.org/doi/10.1103/PhysRevFluids.4.013103

[49] F.-O. Lehmann, S. Gorb, N. Nasir, and P. Schützner, "Elastic deformation and energy loss of flapping fly wings," *Journal of Experimental Biology*, vol. 214, no. 17, pp. 2949–2961, Sep. 2011. [Online]. Available: https://doi.org/10.1242/jeb.045351

[50] R. Dudley, *The biomechanics of insect flight: form, function, evolution*. Princeton University Press, 2002.

[51] A. Bernadou and V. Fourcassié, "Does substrate coarseness matter for foraging ants? An experiment with Lasius niger (Hymenoptera; Formicidae)." *Journal of insect physiology*, vol. 54, no. 3, pp. 534–542, Mar. 2008, place: England.

[52] H. C. Astley and B. C. Jayne, "Effects of perch diameter and incline on the kinematics, performance and modes of arboreal locomotion of corn snakes (Elaphe guttata)." *The Journal of experimental biology*, vol. 210, no. Pt 21, pp. 3862–3872, Nov. 2007, place: England.

[53] T. Kohlsdorf and C. A. Navas, "Evolution of jumping capacity in Tropidurinae lizards: does habitat complexity influence obstacle-crossing ability?" *Biological Journal of the Linnean Society*, vol. 91, no. 3, pp. 393–402, Jul. 2007. [Online]. Available: https://doi.org/10.1111/j.1095-8312.2007.00804.x

[54] B. Vanhooydonck, A. Andronescue, A. Herrel, and D. J. Irschick, "Effects of substrate structure on speed and acceleration capacity in climbing geckos," *Biological Journal of the Linnean Society*, vol. 85, no. 3, pp. 385–393, 2005, _eprint: https://onlinelibrary.wiley.com/doi/pdf/10.1111/j.1095-8312.2005.00495.x. [Online]. Available: https://onlinelibrary.wiley.com/doi/abs/10.1111/j.1095-8312.2005.00495.x

[55] C. Huang, J.-a. Lv, X. Tian, Y. Wang, Y. Yu, and J. Liu, "Miniaturized Swimming Soft Robot with Complex Movement Actuated and Controlled by Remote Light Signals," *Scientific Reports*, vol. 5, no. 1, p. 17414, Dec. 2015. [Online]. Available: https://doi.org/10.1038/srep17414

[56] Y. Yu, M. Nakano, and T. Ikeda, "Directed bending of a polymer film by light," *Nature*, vol. 425, no. 6954, pp. 145–145, Sep. 2003. [Online]. Available: https://doi.org/10.1038/425145a

[57] H. Finkelmann, E. Nishikawa, G. G. Pereira, and M. Warner, "A New Opto-Mechanical Effect in Solids," *Phys. Rev. Lett.*, vol. 87, no. 1, p. 015501, Jun. 2001, publisher: American Physical Society. [Online]. Available: https://link.aps.org/doi/10.1103/PhysRevLett.87.015501

[58] Z. Xu, Y. Zhou, B. Zhang, C. Zhang, J. Wang, and Z. Wang, "Recent Progress on Plant-Inspired Soft Robotics with Hydrogel Building Blocks: Fabrication, Actuation

and Application," *Micromachines*, vol. 12, no. 6, May 2021. [Online]. Available: https://europepmc.org/articles/PMC8225014

[59] J. Z. Kiss, "Up, down, and all around: how plants sense and respond to environmental stimuli," *Proceedings of the National Academy of Sciences of the United States of America*, vol. 103, no. 4, pp. 829–830, Jan. 2006, edition: 2006/01/17 Publisher: National Academy of Sciences. [Online]. Available: https://pubmed.ncbi.nlm.nih.gov/16418288

[60] J. Huang, S. Xia, Z. Li, X. Wu, and J. Ren, "Applications of four-dimensional printing in emerging directions: Review and prospects," *Journal of Materials Science & Technology*, vol. 91, pp. 105–120, 2021. [Online]. Available: https://www.sciencedirect.com/science/article/pii/S1005030221003273

[61] S. A. Gladman, E. A. Matsumoto, R. G. Nuzzo, L. Mahadevan, and J. A. Lewis, "Biomimetic 4D printing," *Nature Materials*, vol. 15, no. 4, pp. 413–418, 2016.

[62] S. Mintchev and D. Floreano, "Adaptive Morphology: A Design Principle for Multimodal and Multifunctional Robots," *IEEE Robotics Automation Magazine*, vol. 23, no. 3, pp. 42–54, Sep. 2016.

[63] J. Shim, C. Perdigou, E. R. Chen, K. Bertoldi, and P. M. Reis, "Buckling-induced encapsulation of structured elastic shells under pressure," *Proceedings of the National Academy of Sciences of the United States of America*, vol. 109, no. 16, pp. 5978–5983, Apr. 2012. [Online]. Available: https://europepmc.org/articles/PMC3341048

[64] T. Lefèvre and M. Auger, "Spider silk inspired materials and sustainability: perspective," *Materials Technology*, vol. 31, no. 7, pp. 384–399, 2016, publisher: Taylor & Francis _eprint: https://doi.org/10.1179/1753555715Y.0000000065. [Online]. Available: https://doi.org/10.1179/1753555715Y.0000000065

[65] O. Tokareva, M. Jacobsen, M. Buehler, J. Wong, and D. L. Kaplan, "Structure–function–property–design interplay in biopolymers: Spider silk," *Acta Biomaterialia*, vol. 10, no. 4, pp. 1612–1626, 2014. [Online]. Available: https://www.sciencedirect.com/science/article/pii/S1742706113004121

[66] T. B. H. Schroeder, J. Houghtaling, B. D. Wilts, and M. Mayer, "It's Not a Bug, It's a Feature: Functional Materials in Insects," *Advanced Materials*, vol. 30, no. 19, p. 1705322, 2018, _eprint: https://onlinelibrary.wiley.com/doi/pdf/10.1002/adma.201705322. [Online]. Available: https://onlinelibrary.wiley.com/doi/abs/10.1002/adma.201705322

[67] Hepburn, H. R. and Kurstjens, S. P., "The combs of honeybees as composite materials," *Apidologie*, vol. 19, no. 1, pp. 25–36, 1988. [Online]. Available: https://doi.org/10.1051/apido:19880102

[68] K. Zhang, H. Duan, B. L. Karihaloo, and J. Wang, "Hierarchical, multilayered cell walls reinforced by recycled silk cocoons enhance the structural integrity of honeybee combs," *Proceedings of the National Academy of Sciences*, vol. 107, no. 21, pp. 9502–9506, 2010, publisher: National Academy of Sciences _eprint: https://www.pnas.org/content/107/21/9502.full.pdf. [Online]. Available: https://www.pnas.org/content/107/21/9502

[69] W. Li, F. Wang, O. Sigmund, and X. S. Zhang, "Design of composite structures with programmable elastic responses under finite deformations," *Journal of the Mechanics and Physics of Solids*, vol. 151, p. 104356, 2021. [Online]. Available: https://www.sciencedirect.com/science/article/pii/S0022509621000533

[70] F. Wang, "Systematic design of 3D auxetic lattice materials with programmable Poisson's ratio for finite strains," *Journal of the Mechanics and Physics of Solids*, vol. 114, pp. 303–318, 2018. [Online]. Available: https://www.sciencedirect.com/science/article/pii/S0022509617308438

[71] F. Wang, O. Sigmund, and J. S. Jensen, "Design of materials with prescribed nonlinear properties," *Journal of the Mechanics and Physics of Solids*, vol. 69, pp. 156–174, 2014. [Online]. Available: https://www.sciencedirect.com/science/article/pii/S0022509614000866

[72] S. Shan, S. H. Kang, J. R. Raney, P. Wang, L. Fang, F. Candido, J. A. Lewis, and K. Bertoldi, "Multistable Architected Materials for Trapping Elastic Strain Energy," *Advanced Materials*, vol. 27, no. 29, pp. 4296–4301, 2015.

[73] O. Sigmund, "Tailoring materials with prescribed elastic properties," *Mechanics of Materials*, vol. 20, no. 4, pp. 351–368, 1995. [Online]. Available: https://www.sciencedirect.com/science/article/pii/0167663694000697

[74] L. H. Dudte, E. Vouga, T. Tachi, and L. Mahadevan, "Programming curvature using origami tessellations." *Nature materials*, vol. 15, no. 5, pp. 583–588, May 2016, place: England.

[75] T. J. White and D. J. Broer, "Programmable and adaptive mechanics with liquid crystal polymer networks and elastomers," *Nature Materials*, vol. 14, no. 11, pp. 1087–1098, Nov. 2015. [Online]. Available: https://doi.org/10.1038/nmat4433

[76] A. Kotikian, C. McMahan, E. C. Davidson, J. M. Muhammad, R. D. Weeks, C. Daraio, and J. A. Lewis, "Untethered soft robotic matter with passive control of shape morphing and propulsion," *Science Robotics*, vol. 4, no. 33, 2019, publisher: Science Robotics _eprint: https://robotics.sciencemag.org/content/4/33/eaax7044.full.pdf. [Online]. Available: https://robotics.sciencemag.org/content/4/33/eaax7044

[77] Y.-Y. Xiao, Z.-C. Jiang, J.-B. Hou, and Y. Zhao, "Desynchronized liquid crystalline network actuators with deformation reversal capability," *Nature Communications*, vol. 12, no. 1, p. 624, Jan. 2021. [Online]. Available: https://doi.org/10.1038/s41467-021-20938-6

[78] Y. Sun, J. S. Evans, T. Lee, B. Senyuk, P. Keller, S. He, and I. I. Smalyukh, "Optical manipulation of shape-morphing elastomeric liquid crystal microparticles doped with gold nanocrystals," *Applied Physics Letters*, vol. 100, no. 24, p. 241901, Jun. 2012. [Online]. Available: https://doi.org/10.1063/1.4729143

[79] H. K. Bisoyi, A. M. Urbas, and Q. Li, "Soft Materials Driven by Photothermal Effect and Their Applications," *Advanced Optical Materials*, vol. 6, no. 15, p. 1800458, Aug. 2018. [Online]. Available: https://doi.org/10.1002/adom.201800458

[80] J. M. McCracken, B. R. Donovan, and T. J. White, "Materials as Machines," *Advanced Materials*, vol. 32, no. 20, p. 1906564, 2020, _eprint: https://onlinelibrary.wiley.com/doi/pdf/10.1002/adma.201906564. [Online]. Available: https://onlinelibrary.wiley.com/doi/abs/10.1002/adma.201906564

[81] Y. Bar-Cohen, "Electroactive Polymers as Artificial Muscles: A Review," *Journal of Spacecraft and Rockets*, vol. 39, no. 6, pp. 822–827, 2002, _eprint: https://doi.org/10.2514/2.3902. [Online]. Available: https://doi.org/10.2514/2.3902

[82] G.-Y. Gu, J. Zhu, L.-M. Zhu, and X. Zhu, "A survey on dielectric elastomer actuators for soft robots." *Bioinspiration & biomimetics*, vol. 12, no. 1, p. 011003, Jan. 2017, place: England.

[83] Y. Bar-Cohen, "Electroactive polymers as an enabling materials technology," *Proceedings of the Institution of Mechanical Engineers, Part G: Journal of Aerospace Engineering*, vol. 221, no. 4, pp. 553–564, 2007, _eprint: https://doi.org/10.1243/09544100JAERO141. [Online]. Available: https://doi.org/10.1243/09544100JAERO141

[84] R. Brighenti, F. Artoni, and M. P. Cosma, "Mechanics of innovative responsive polymers," *Mechanics Research Communications*, vol. 100, p. 103403, 2019. [Online]. Available: https://www.sciencedirect.com/science/article/pii/S0093641319301661

[85] ——, "Mechanics of Active Mechano-Chemical Responsive Polymers," in *IOP Conference Series: Materials Science and Engineering*, vol. 416. IOP Publishing, 2018, p. 012080, issue: 1.

[86] R. Brighenti, F. Artoni, F. Vernerey, M. Torelli, A. Pedrini, I. Domenichelli, and E. Dalcanale, "Mechanics of responsive polymers via conformationally switchable molecules," *Journal of the Mechanics and Physics of Solids*, vol. 113, pp. 65–81, 2018, publisher: Elsevier.

[87] R. Brighenti, F. Artoni, and M. P. Cosma, "Mechanics of Chemo-Mechanical Stimuli Responsive Soft Polymers," in *Proceedings of XXIV AIMETA Conference 2019*, A. Carcaterra, A. Paolone, and G. Graziani, Eds. Cham: Springer International Publishing, 2020, pp. 627–637.

[88] R. Klajn, "Spiropyran-based dynamic materials," *Chem. Soc. Rev.*, vol. 43, no. 1, pp. 148–184, 2014, publisher: The Royal Society of Chemistry. [Online]. Available: http://dx.doi.org/10.1039/C3CS60181A

[89] A. D. Das, G. Mannoni, A. E. Früh, D. Orsi, R. Pinalli, and E. Dalcanale, "Damage-Reporting Carbon Fiber Epoxy Composites," *ACS Applied Polymer Materials*, vol. 1, no. 11, pp. 2990–2997, Nov. 2019, publisher: American Chemical Society. [Online]. Available: https://doi.org/10.1021/acsapm.9b00694

[90] M. A. Ghanem, A. Basu, R. Behrou, N. Boechler, A. J. Boydston, S. L. Craig, Y. Lin, B. E. Lynde, A. Nelson, H. Shen, and D. W. Storti, "The role of polymer mechanochemistry in responsive materials and additive manufacturing," *Nature Reviews Materials*, vol. 6, no. 1, pp. 84–98, Jan. 2021. [Online]. Available: https://doi.org/10.1038/s41578-020-00249-w

[91] D. Schütze, K. Holz, J. Müller, M. K. Beyer, U. Lüning, and B. Hartke, "Pinpointing Mechanochemical Bond Rupture by Embedding the Mechanophore into a Macrocycle," *Angewandte Chemie International Edition*, vol. 54, no. 8, pp. 2556–2559, 2015, _eprint: https://onlinelibrary.wiley.com/doi/pdf/10.1002/anie.201409691. [Online]. Available: https://onlinelibrary.wiley.com/doi/abs/10.1002/anie.201409691

[92] M. Kadic, G. W. Milton, M. van Hecke, and M. Wegener, "3D metamaterials," *Nature Reviews Physics*, vol. 1, no. 3, pp. 198–210, Mar. 2019. [Online]. Available: https://doi.org/10.1038/s42254-018-0018-y

[93] J. U. Surjadi, L. Gao, H. Du, X. Li, X. Xiong, N. X. Fang, and Y. Lu, "Mechanical Metamaterials and Their Engineering Applications," *Advanced Engineering Materials*, vol. 21, no. 3, p. 1800864, 2019, _eprint: https://onlinelibrary.wiley.com/doi/pdf/10.1002/adem.201800864. [Online]. Available: https://onlinelibrary.wiley.com/doi/abs/10.1002/adem.201800864

[94] K. Bertoldi, V. Vitelli, J. Christensen, and M. van Hecke, "Flexible mechanical metamaterials," *Nature Reviews Materials*, vol. 2, no. 11, p. 17066, Oct. 2017. [Online]. Available: https://doi.org/10.1038/natrevmats.2017.66

[95] S. Waitukaitis, R. Menaut, B. G.-g. Chen, and M. van Hecke, "Origami Multistability: From Single Vertices to Metasheets," *Phys. Rev. Lett.*, vol. 114, no. 5, p. 055503, Feb. 2015, publisher: American Physical Society. [Online]. Available: https://link.aps.org/doi/10.1103/PhysRevLett.114.055503

[96] Y. Miyamoto, W. Kaysser, B. Rabin, A. Kawasaki, and R. G. Ford, *Functionally graded materials: design, processing and applications*. Springer Science & Business Media, 2013, vol. 5.

[97] A. A. Bauhofer, S. Krödel, J. Rys, O. R. Bilal, A. Constantinescu, and C. Daraio, "Harnessing Photochemical Shrinkage in Direct Laser Writing for Shape Morphing of Polymer Sheets," *Advanced Materials*, vol. 29, no. 42, p. 1703024, 2017, _eprint: https://onlinelibrary.wiley.com/doi/pdf/10.1002/adma.201703024. [Online]. Available: https://onlinelibrary.wiley.com/doi/abs/10.1002/adma.201703024

[98] F. Brömmel, D. Kramer, and H. Finkelmann, "Preparation of Liquid Crystalline Elastomers," in *Liquid Crystal Elastomers: Materials and Applications*, W. H. de Jeu, Ed. Berlin, Heidelberg: Springer Berlin Heidelberg, 2012, pp. 1–48. [Online]. Available: https://doi.org/10.1007/12_2012_168

[99] M. Warner and E. Terentjev, *Liquid Crystal Elastomers*. Oxford Science Publications, 2003.

[100] R. Yang and Y. Zhao, "Multitemperature Memory Actuation of a Liquid Crystal Polymer Network over a Broad Nematic–Isotropic Phase Transition Induced by Large Strain," *ACS Macro Letters*, vol. 7, no. 3, pp. 353–357, Mar. 2018, publisher: American Chemical Society. [Online]. Available: https://doi.org/10.1021/acsmacrolett.8b00089

[101] A. Kotikian, R. L. Truby, J. W. Boley, T. J. White, and J. A. Lewis, "3D Printing of Liquid Crystal Elastomeric Actuators with Spatially Programed Nematic Order," *Advanced Materials*, vol. 30, no. 10, p. 1706164, 2018, _eprint: https://onlinelibrary.wiley.com/doi/pdf/10.1002/adma.201706164. [Online]. Available: https://onlinelibrary.wiley.com/doi/abs/10.1002/adma.201706164

[102] L. Ren, B. Li, Y. He, Z. Song, X. Zhou, Q. Liu, and L. Ren, "Programming Shape-Morphing Behavior of Liquid Crystal Elastomers via Parameter-Encoded 4D Printing," *ACS Applied Materials & Interfaces*, vol. 12, no. 13, pp. 15 562–15 572, Apr. 2020, publisher: American Chemical Society. [Online]. Available: https://doi.org/10.1021/acsami.0c00027

[103] M. O. Saed, C. P. Ambulo, H. Kim, R. De, V. Raval, K. Searles, D. A. Siddiqui, J. M. O. Cue, M. C. Stefan, M. R. Shankar, and T. H. Ware, "Molecularly-Engineered, 4D-Printed Liquid Crystal Elastomer Actuators," *Advanced Functional Materials*, vol. 29, no. 3, p. 1806412, Jan. 2019, publisher: John Wiley & Sons, Ltd. [Online]. Available: https://doi.org/10.1002/adfm.201806412

[104] R. Yang and Y. Zhao, "Non-Uniform Optical Inscription of Actuation Domains in a Liquid Crystal Polymer of Uniaxial Orientation: An Approach to Complex and Programmable

Shape Changes," *Angewandte Chemie International Edition*, vol. 56, no. 45, pp. 14 202–14 206, 2017, _eprint: https://onlinelibrary.wiley.com/doi/pdf/10.1002/anie.201709528. [Online]. Available: https://onlinelibrary.wiley.com/doi/abs/10.1002/anie.201709528

[105] C. W. Oseen, "The theory of liquid crystals," *Trans. Faraday Soc.*, vol. 29, no. 140, pp. 883–899, 1933, publisher: The Royal Society of Chemistry. [Online]. Available: http://dx.doi.org/10.1039/TF9332900883

[106] F. C. Frank, "I. Liquid crystals. On the theory of liquid crystals," *Discuss. Faraday Soc.*, vol. 25, no. 0, pp. 19–28, 1958, publisher: The Royal Society of Chemistry. [Online]. Available: http://dx.doi.org/10.1039/DF9582500019

[107] J. L. Ericksen, "Conservation Laws for Liquid Crystals," *Transactions of the Society of Rheology*, vol. 5, no. 1, pp. 23–34, Mar. 1961, publisher: The Society of Rheology. [Online]. Available: https://doi.org/10.1122/1.548883

[108] F. M. Leslie, "Some constitutive equations for liquid crystals," *Archive for Rational Mechanics and Analysis*, vol. 28, no. 4, pp. 265–283, Jan. 1968. [Online]. Available: https://doi.org/10.1007/BF00251810

[109] M. Warner and E. Terentjev, *Liquid crystal elastomers*. Oxford University Press, 2007, vol. 120.

[110] P. Bladon, E. M. Terentjev, and M. Warner, "Transitions and instabilities in liquid crystal elastomers," *Phys. Rev. E*, vol. 47, no. 6, pp. R3838–R3840, Jun. 1993, publisher: American Physical Society. [Online]. Available: https://link.aps.org/doi/10.1103/PhysRevE.47.R3838

[111] P. Bladon, E. Terentjev, and M. Warner, "Deformation–induced orientational transitions in liquid crystals elastomer," *Journal de Physique II*, vol. 4, no. 1, pp. 75–91, 1994, publisher: EDP Sciences.

[112] J. S. Biggins, M. Warner, and K. Bhattacharya, "Supersoft Elasticity in Polydomain Nematic Elastomers," *Phys. Rev. Lett.*, vol. 103, no. 3, p. 037802, Jul. 2009, publisher: American Physical Society. [Online]. Available: https://link.aps.org/doi/10.1103/PhysRevLett.103.037802

[113] ——, "Elasticity of polydomain liquid crystal elastomers," *Journal of the Mechanics and Physics of Solids*, vol. 60, no. 4, pp. 573–590, 2012. [Online]. Available: https://www.sciencedirect.com/science/article/pii/S0022509612000166

[114] V. Agostiniani and A. DeSimone, "Rigorous derivation of active plate models for thin sheets of nematic elastomers," *Mathematics and Mechanics of Solids*, vol. 25, no. 10, pp. 1804–1830, Oct. 2020, publisher: SAGE Publications Ltd STM. [Online]. Available: https://doi.org/10.1177/1081286517699991

[115] L. A. Mihai and A. Goriely, "A plate theory for nematic liquid crystalline solids," *Journal of the Mechanics and Physics of Solids*, vol. 144, p. 104101, 2020. [Online]. Available: https://www.sciencedirect.com/science/article/pii/S0022509620303355

[116] A. DeSimone, "Nematic elastomers: modelling, analysis, and numerical simulations," in *Poly-, Quasi- and Rank-One Convexity in Applied Mechanics*, J. Schröder and P. Neff, Eds. Vienna: Springer Vienna, 2010, pp. 241–264. [Online]. Available: https://doi.org/10.1007/978-3-7091-0174-2_7

[117] M. Warner, K. P. Gelling, and T. A. Vilgis, "Theory of nematic networks," *The Journal of Chemical Physics*, vol. 88, no. 6, pp. 4008–4013, 1988, _eprint: https://doi.org/10.1063/1.453852. [Online]. Available: https://doi.org/10.1063/1.453852

[118] M. Doi, *Introduction to polymer physics*. Oxford University Press, 1996.

[119] Y. Zhang, C. Xuan, Y. Jiang, and Y. Huo, "Continuum mechanical modeling of liquid crystal elastomers as dissipative ordered solids," *Journal of the Mechanics and Physics of Solids*, vol. 126, pp. 285–303, 2019. [Online]. Available: https://www.sciencedirect.com/science/article/pii/S0022509618308226

[120] R. Brighenti, F. Artoni, and M. P. Cosma, "Mechanics of materials with embedded unstable molecules," *International Journal of Solids and Structures*, 2018, publisher: Elsevier.

[121] T. Ohzono, K. Katoh, and E. M. Terentjev, "Microscopy of Diffuse Nematic–Isotropic Transition in Main-Chain Nematic Liquid-Crystal Elastomers," *Macromolecules*, vol. 54, no. 8, pp. 3678–3688, Apr. 2021, publisher: American Chemical Society. [Online]. Available: https://doi.org/10.1021/acs.macromol.1c00356

[122] P.-G. De Gennes and J. Prost, *The physics of liquid crystals*. Oxford university press, 1993, vol. 83.

[123] Z.-C. Jiang, Y.-Y. Xiao, X. Tong, and Y. Zhao, "Selective Decrosslinking in Liquid Crystal Polymer Actuators for Optical Reconfiguration of Origami and Light-Fueled Locomotion," *Angewandte Chemie International Edition*, vol. 58, no. 16, pp. 5332–5337, 2019, _eprint: https://onlinelibrary.wiley.com/doi/pdf/10.1002/anie.201900470. [Online]. Available: https://onlinelibrary.wiley.com/doi/abs/10.1002/anie.201900470

[124] K. A. Burke, I. A. Rousseau, and P. T. Mather, "Reversible actuation in main-chain liquid crystalline elastomers with varying crosslink densities," *Polymer*, vol. 55, no. 23, pp. 5897–5907, 2014. [Online]. Available: https://www.sciencedirect.com/science/article/pii/S0032386114005825

[125] C. M. Spillmann, J. Naciri, M.-S. Chen, A. Srinivasan, and B. R. Ratna, "Tuning the physical properties of a nematic liquid crystal elastomer actuator," *Liquid Crystals*, vol. 33, no. 4, pp. 373–380, 2006, publisher: Taylor & Francis _eprint: https://doi.org/10.1080/02678290500494921. [Online]. Available: https://doi.org/10.1080/02678290500494921

[126] J. Küpfer, E. Nishikawa, and H. Finkelmann, "Densely crosslinked liquid single-crystal elastomers," *Polymers for Advanced Technologies*, vol. 5, no. 2, pp. 110–115, 1994, _eprint: https://onlinelibrary.wiley.com/doi/pdf/10.1002/pat.1994.220050205. [Online]. Available: https://onlinelibrary.wiley.com/doi/abs/10.1002/pat.1994.220050205

[127] R. Brighenti and M. P. Cosma, "Smart actuation of liquid crystal elastomer elements: cross-link density-controlled response," *Smart Materials and Structures*, vol. 31, no. 1, p. 015012, Nov. 2021, publisher: IOP Publishing.

[128] S. M. Clarke, A. Hotta, A. R. Tajbakhsh, and E. M. Terentjev, "Effect of crosslinker geometry on equilibrium thermal and mechanical properties of nematic elastomers." *Physical review. E, Statistical, nonlinear, and soft matter physics*, vol. 64, no. 6 Pt 1, p. 061702, Dec. 2001, place: United States.

[129] D. R. Anderson, "Thermal Conductivity of Polymers," *Chemical Reviews*, vol. 66, no. 6, pp. 677–690, Oct. 1966, publisher: American Chemical Society. [Online]. Available: https://doi.org/10.1021/cr60244a004

[130] C. L. Choy, "Thermal conductivity of polymers," *Polymer*, vol. 18, no. 10, pp. 984–1004, 1977. [Online]. Available: https://www.sciencedirect.com/science/article/pii/0032386177900027

[131] J. E. Mark and others, *Physical properties of polymers handbook*. Springer, 2007, vol. 1076.

[132] M. P. Cosma and R. Brighenti, "Controlled morphing of architected liquid crystal elastomer elements: modeling and simulations," *Mechanics Research Communications*, vol. 121, p. 103858, 2022. [Online]. Available: https://www.sciencedirect.com/science/article/pii/S0093641322000180

[133] H. Bikas, P. Stavropoulos, and G. Chryssolouris, "Additive manufacturing methods and modelling approaches: a critical review," *The International Journal of Advanced Manufacturing Technology*, vol. 83, no. 1, pp. 389–405, Mar. 2016. [Online]. Available: https://doi.org/10.1007/s00170-015-7576-2

[134] R. Brighenti, M. P. Cosma, L. Marsavina, A. Spagnoli, and M. Terzano, "Laser-based additively manufactured polymers: a review on processes and mechanical models," *Journal of Materials Science*, 2020.

[135] J. Wu, Z. Zhao, C. M. Hamel, X. Mu, X. Kuang, Z. Guo, and H. J. Qi, "Evolution of material properties during free radical photopolymerization," *Journal of the Mechanics and Physics of Solids*, vol. 112, pp. 25–49, Mar. 2018, publisher: Elsevier Ltd.

[136] R. Anastasio, W. Peerbooms, R. Cardinaels, and L. C. Van Breemen, "Characterization of Ultraviolet-Cured Methacrylate Networks: From Photopolymerization to Ultimate Mechanical Properties," *Macromolecules*, vol. 52, no. 23, pp. 9220–9231, 2019.

[137] Y. Yang, L. Li, and J. Zhao, "Mechanical property modeling of photosensitive liquid resin in stereolithography additive manufacturing: Bridging degree of cure with tensile strength and hardness," *Materials & Design*, vol. 162, pp. 418–428, Jan. 2019.

[138] T. Nakamoto, K. Yamaguchi, P. A. Abraha, and K. Mishima, "Manufacturing of three-dimensional micro-parts by UV laser induced polymerization," *Journal of Micromechanics and Microengineering*, vol. 6, no. 2, pp. 240–253, 1996.

[139] K. Yamaguchi and T. Nakamoto, "Micro fabrication by UV laser photopolymerization," *Memoirs of the School of Engineering, Nagoya University*, vol. 50, no. 1-2, pp. 33–82, 1998.

[140] J. H. Lee, R. K. Prud'homme, and I. A. Aksay, "Cure depth in photopolymerization: Experiments and theory," *Journal of Materials Research*, vol. 16, no. 12, pp. 3536–3544, 2001.

[141] C. N. Bowman and C. J. Kloxin, "Toward an enhanced understanding and implementation of photopolymerization reactions," *AIChE Journal*, vol. 54, no. 11, pp. 2775–2795, 2008, iSBN: 9513862380.

[142] Y. Tang, C. Henderson, J. Muzzy, and D. W. Rosen, "Stereolithography cure modelling and simulation," *International Journal of Materials and Product Technology*, vol. 21, no. 4, p. 255, 2004.

[143] M. F. Perry and G. W. Young, "A Mathematical Model for Photopolymerization From a Stationary Laser Light Source," *Macromolecular Theory and Simulations*, vol. 14, no. 1, pp. 26–39, Jan. 2005.

[144] P. J. d. S. Bartolo, "Photo-curing modelling: direct irradiation," *The International Journal of Advanced Manufacturing Technology*, vol. 32, no. 5-6, pp. 480–491, 2007, iSBN: 0017000503745.

[145] R. Brighenti and M. P. Cosma, "Mechanical behavior of photopolymerized materials," *Journal of the Mechanics and Physics of Solids*, vol. 153, p. 104456, 2021.

[146] R. Brighenti, M. P. Cosma, L. Marsavina, A. Spagnoli, and M. Terzano, "Multiphysics modelling of the mechanical properties in polymers obtained via photo-induced

polymerization," *The International Journal of Advanced Manufacturing Technology*, Jul. 2021. [Online]. Available: https://doi.org/10.1007/s00170-021-07273-2

[147] D. Wu, Y. Huang, Q. Zhang, P. Wang, Y. Pei, Z. Zhao, and D. Fang, "Initiation of surface wrinkling during photopolymerization," *Journal of the Mechanics and Physics of Solids*, vol. 162, p. 104838, 2022. [Online]. Available: https://www.sciencedirect.com/science/article/pii/S0022509622000539

[148] M. Zarrelli, A. Skordos, and I. Partridge, "Toward a constitutive model for cure-dependent modulus of a high temperature epoxy during the cure," *European Polymer Journal*, vol. 46, no. 8, pp. 1705–1712, Aug. 2010, publisher: Elsevier Ltd.

[149] P. G. de Gennes and L. Leger, "Dynamics of Entangled Polymer Chains," *Annual Review of Physical Chemistry*, vol. 33, no. 1, pp. 49–61, 1982, _eprint: https://doi.org/10.1146/annurev.pc.33.100182.000405. [Online]. Available: https://doi.org/10.1146/annurev.pc.33.100182.000405

[150] M. P. Cosma and R. Brighenti, "Photopolymerized additive manufacturing materials: Modeling of the printing process, mechanical behavior, and sensitivity analysis," *Material Design & Processing Communications*, vol. n/a, no. n/a, p. e225, 2021, _eprint: https://onlinelibrary.wiley.com/doi/pdf/10.1002/mdp2.225. [Online]. Available: https://onlinelibrary.wiley.com/doi/abs/10.1002/mdp2.225

[151] A. B. Davis and A. Marshak, "Photon propagation in heterogeneous optical media with spatial correlations: enhanced mean-free-paths and wider-than-exponential free-path distributions," *Journal of Quantitative Spectroscopy and Radiative Transfer*, vol. 84, no. 1, pp. 3 – 34, 2004. [Online]. Available: http://www.sciencedirect.com/science/article/pii/S0022407303001146

[152] J. Nocedal and S. Wright, *Numerical optimization*. Springer Science & Business Media, 2006.

[153] A. Quarteroni, "Diffusion-transport-reaction equations," in *Numerical Models for Differential Problems*. Cham: Springer International Publishing, 2017, pp. 315–365. [Online]. Available: https://doi.org/10.1007/978-3-319-49316-9_13

[154] S. C. Ligon, B. Husár, H. Wutzel, R. Holman, and R. Liska, "Strategies to reduce oxygen inhibition in photoinduced polymerization," *Chemical Reviews*, vol. 114, no. 1, pp. 557–589, Jan. 2014, publisher: American Chemical Society. [Online]. Available: https://doi.org/10.1021/cr3005197

[155] Y. Gao, M. Wei, X. Li, W. Xu, A. Ahiabu, J. Perdiz, Z. Liu, and M. J. Serpe, "Stimuli-responsive polymers: Fundamental considerations and applications," *Macromolecular*

Research, vol. 25, no. 6, pp. 513–527, Jun. 2017. [Online]. Available: https://doi.org/10.1007/s13233-017-5088-7

[156] K. Bhattacharya and R. D. James, "The Material Is the Machine," *Science*, vol. 307, no. 5706, pp. 53–54, 2005, _eprint: https://www.science.org/doi/pdf/10.1126/science.1100892. [Online]. Available: https://www.science.org/doi/abs/10.1126/science.1100892

[157] C. Zhang, X. Lu, G. Fei, Z. Wang, H. Xia, and Y. Zhao, "4D Printing of a Liquid Crystal Elastomer with a Controllable Orientation Gradient," *ACS Applied Materials & Interfaces*, vol. 11, no. 47, pp. 44 774–44 782, Nov. 2019, publisher: American Chemical Society. [Online]. Available: https://doi.org/10.1021/acsami.9b18037

[158] Y. Guo, J. Zhang, W. Hu, M. T. A. Khan, and M. Sitti, "Shape-programmable liquid crystal elastomer structures with arbitrary three-dimensional director fields and geometries," *Nature Communications*, vol. 12, no. 1, p. 5936, Oct. 2021. [Online]. Available: https://doi.org/10.1038/s41467-021-26136-8